

Molecular Dynamics Simulations of Gold Nanomaterials

by

Yanting Wang

Submitted in Partial Fulfillment

of the

Requirements for the Degree

Doctor of Philosophy

Supervised by

Professor Stephen L. Teitel

Department of Physics and Astronomy

The College

Arts and Sciences

University of Rochester

Rochester, New York

2004

CURRICULUM VITAE

The author was born on April 23, 1973 in Jiangxi Province, People's Republic of China. He received his B.E. in nuclear electronics from the University of Science and Technology of China in 1994. He continued his graduate study in the same university from 1994 to 1999 and obtained his Ph.D. in nuclear physics, specialized in signal processing. In the fall of 1999, he entered the graduate school of the University of Rochester. He was a research assistant of Professor Steven L. Manly in the first year. Then he joined Professor Christoph Dellago's research group in the Chemistry Department of UR from summer 2000 to summer 2002. In 2001 he received his M.A. in physics from the University of Rochester. He was partly supported by a Teaching Assistantship from the Chemistry Department of UR in the spring semester of 2002. In the fall of 2002 he became a research assistant of Professor Stephen L. Teitel and continued his research work in the area of theoretical condensed matter.

ACKNOWLEDGMENTS

I would like to express my sincere gratitude to my advisor Professor Stephen L. Teitel for his great instruction and encouragement of creative ideas. I thank my previous advisor Professor Christoph Dellago for leading me into the door of theoretical statistical mechanics. Both professors showed me the art of theoretical physics.

I would like to thank faculty and staff both in the Physics and Astronomy Department and in the Chemistry Department for supporting my research work in many ways. My special thanks go to our graduate student administrative assistant Barbara Warren, who was always ready to help me with various kinds of problems.

ABSTRACT

We have carried out Molecular Dynamics simulations to study the thermal stability and melting behavior of gold nanoclusters and gold nanorods. The surface is found to play a very important role in both gold nanomaterials. Upon cooling from the liquid, we find that gold nanoclusters with 600–3000 atoms crystallize into a Mackay icosahedron. Upon heating, the $\{111\}$ facets on the surface of the Mackay icosahedral gold nanoclusters soften but do not premelt below the bulk melting temperature. We attribute this surface softening to the increasing mobility of vertex and edge atoms with temperature, which leads to inter-layer and intra-layer diffusion, and a shrinkage of the average facet size. Upon heating, our simulated gold nanorods undergo a shape transformation preceding the melting transition. The shape transformation is induced by a minimization of the surface free energy, and is accompanied by a complete reconstruction of the internal structure driven by the surface change. During the transformation, the atoms on the end caps of the rod move to the sides of the rods, leading the rods to be shorter and wider. After the transformation, the surface of the stable intermediate state rod is mostly covered by the more stable $\{111\}$ facets, other than the less stable $\{110\}$ and $\{100\}$ facets covering the sides of the initial constructed rod.

CONTENTS

1. Introduction	1
2. Overview of Research on Gold Nanomaterials	7
2.1 Bulk Gold	7
2.2 Structures of Nanoclusters	11
2.3 Gold Nanoclusters	15
2.4 Gold Nanorods	21
3. Methods	28
3.1 Glue Potential Model	28
3.2 Molecular Dynamics Methods	30
3.3 Quantifying Structure by Bond Orientational Order Parameters	34
3.4 Radius of Gyration to Monitor the Shape Change	39
3.5 Geometrical Analysis of the Surface	40
3.5.1 Cone Algorithm	40
3.5.2 Curvature	41
3.5.3 Average Shape	45
3.6 Atom Diffusion Analysis	48
4. Melting of Mackay Icosahedral Gold Nanoclusters	50
4.1 Mackay Icosahedra with a Missing Central Atom	51
4.2 Melting and the Bond Orientational Order Parameters	54
4.3 Average Shape and Surface Curvature	60

4.4	Diffusion of Atoms	66
4.5	Discussion and Conclusions	78
5.	Continuous Heating of Gold Nanorods	81
5.1	Initial Structure and Heating Rate	81
5.2	Shape Transformation and Melting Transition	83
5.3	Intermediate State	93
5.4	Local Structure Analysis	94
5.5	Discussion and Conclusions	99
6.	Quasi-Equilibrium Heating of Gold Nanorods	102
6.1	Quasi-equilibrium Heating	103
6.2	Intermediate State and Random Stacking	108
6.3	Average Cross-Sectional Shape and Surface Curvature	113
6.4	Structural Change of Different Layers	115
6.5	Evolution of the Interior	118
6.6	Diffusion of Atoms	120
6.7	Discussion and Conclusions	122
7.	Summary	125
	Bibliography	132

LIST OF TABLES

3.1	Bond order parameters for 3D face-centered-cubic (fcc), hexagonal-close-packed (hcp), simple-cubic (sc), body-centered-cubic (bcc), liquid, and Mackay icosahedral (Ih) bulk structures, as well as 2D Ih surface, gold {110} surface, gold {100} surface, and gold {111} surface structures.	38
4.1	Average numbers of atoms in the surface layer, the sub layers and the bulk of an $N = 2624$ atom gold cluster at different temperatures. . . .	57
5.1	Aspect ratios of the intermediate states.	94

LIST OF FIGURES

1.1	TEM image of gold nanorods after exposure to nanosecond laser pulses. Nanoparticles having the ϕ -shape are highlighted by circles. Courtesy of Link <i>et al.</i> from Ref. [29].	4
1.2	HRTEM images of gold nanorods after exposure to femtosecond laser pulses. The arrowheads in (a) indicate the nanorods with point defects and twins. Those individual particles are further enlarged in (b) two nanorods with point defects, and (c) twinned particles. Courtesy of Link <i>et al.</i> from Ref. [30].	6
2.1	Three low-index planes of the fcc structure: (a) $\{100\}$, (b) $\{110\}$, and (c) $\{111\}$. The involved particles are in black.	8
2.2	Pictures of three low-index gold surfaces: (a) gold $\{110\}$, (b) gold $\{100\}$, and (c) gold $\{111\}$	9
2.3	A tetrahedron is built up layer by layer by hexagonal planes. Courtesy of Martin from Ref. [15].	12
2.4	An ideal Ih structure with the magic number of 2869 atoms. Atoms are shaded to indicate their local structure: fcc is white, hcp is gray, and “other” is black.	13
2.5	(a) Five tetrahedra sharing an edge form a decahedron with a gap. (b) A decahedron built up by adding umbrella-shaped partial layers with a common vertex at the bottom. Courtesy of Martin from Ref. [15].	14

2.6	A 309-atom truncated decahedron with square $\{100\}$ facets. Courtesy of Martin from Ref. [15].	14
2.7	A 586-atom truncated octahedron with square and hexagonal facets. Courtesy of Martin from Ref. [15].	15
2.8	A 147-atom cuboctahedron. Courtesy of Martin from Ref. [15].	16
2.9	A hexagonal prism gold nanocluster with 30 atoms. Courtesy of Wilson and Johnston from Ref. [46].	18
2.10	Experimental values of the bulk melting temperature T_m of gold particles. The horizontal axis is the diameter of the particle in Å. The solid line is a theoretical fit to the experimental data. Courtesy of Buffat and Borel from Ref. [54].	19
2.11	Elongated cyclic penta-tetrahedral twin model of gold nanorods.	22
2.12	The structure model of the long Au nanorods observed in Ref. [57]. Courtesy of Wang <i>et al.</i> from Ref. [57].	22
2.13	(a) HRTEM image of an Au nanorod. The inset is the electron diffraction pattern recorded from the rod, which proves the single crystalline structure of the rod. (b) A structural model of the Au nanorod shown in (a). Courtesy of Wang <i>et al.</i> from Ref. [57].	23
2.14	Atomic models of (a) an ideal $\{110\}$ surface and (b) the reconstructed $\{110\}$ surface with missing rows. Courtesy of Wang <i>et al.</i> from Ref. [71].	25
2.15	A schematic process suggested in Ref. [30] for the structural transformation from nanorod to nanosphere. Courtesy of Link <i>et al.</i> from Ref. [30].	27
3.1	Three functions $\phi(r)$, $U(n)$, and $\rho(r)$ of the glue potential model optimized for gold.	31
3.2	Pair correlation functions of the gold nanoclusters with $N = 2624$ atoms at $T = 100$ K with the Ih structure, and at $T = 1500$ K in the liquid state.	35

3.3	The values of (a) the bulk and (b) the surface bond orientational order parameters vs. the cluster size N of several Ih structures. Only magic numbers N that give ideal Ih structures are used.	37
3.4	Schematic of the cone algorithm.	40
3.5	Cross sections of a gold cluster with 2624 atoms at (a) $T = 200$ K in an Ih structure and (b) $T = 1200$ K in the liquid, with the 5 topmost layers, as determined by the cone algorithm, marked by different gray scales.	41
3.6	Schematic for the calculation of the bond curvature.	43
3.7	Schematic for the calculation of the local surface curvatures.	44
3.8	Histograms of bond curvature c_b and maximal local curvature κ_M of (i) top row: an ideal Ih cluster with $N = 2869$ atoms, and (ii) bottom row: the average shape of a liquid cluster with $N = 2624$ atoms.	46
3.9	A liquid gold cluster with 2624 atoms at $T = 1200$ K. (a) and (b) are two instantaneous configurations. (c) is the shape averaged over 1000 such instantaneous configurations.	47
4.1	Ih structure of an $N = 2624$ atom gold cluster at $T = 200$ K. (a) Surface of an instantaneous configuration with atoms shaded according to the maximal local curvature; the larger the curvature, the darker the gray scale. (b) The same configuration with the three outer most layers peeled away. Atoms are shaded according to their local crystal structure: fcc is white, hcp is gray, and “other” is black.	52
4.2	Ih structure of gold clusters with (a) $N = 603$ and (b) $N = 1409$ atoms at $T = 200$ K. The atoms on the surfaces of these instantaneous configurations are shaded according to the maximal local curvature; the larger the curvature, the darker the gray scale.	54

4.3	Caloric curve of Ih gold clusters with $N = 603, 1409,$ and 2624 atoms, as well as with magic numbers of $N = 922$ and 5082 atoms with a missing central atom.	55
4.4	Bond orientational order parameters of the $N = 2624$ atom cluster for (a) the interior atoms, and (b) the surface atoms. Sample error bars, representing configuration to configuration fluctuations, are shown.	59
4.5	Q_6^* for different layers of the $N = 2624$ atom cluster. In order to see the tendency of softening in each layer clearly, the values of Q_6 have been normalized by their values at low temperature $T = 400$ K, $Q_6^* = Q_6(T)/Q_6(400 \text{ K})$	60
4.6	Bond orientational order parameters of the $N = 603$ atom cluster for (a) the interior atoms, and (b) the surface atoms.	61
4.7	Bond orientational order parameters of the magic number $N = 922$ atom cluster for (a) the interior atoms, and (b) the surface atoms.	61
4.8	Bond orientational order parameters of the $N = 1409$ atom cluster for (a) the interior atoms, and (b) the surface atoms.	62
4.9	Bond orientational order parameters of the magic number $N = 5082$ atom cluster for (a) the interior atoms, and (b) the surface atoms.	62
4.10	Average shapes of an $N = 2624$ atom cluster at $400, 600, 900, 1060$ and 1100 K. The top row shows each of the discretized solid angles of the surface shaded according to the value of the maximal local curvature; the darker the gray scale, the larger the curvature. The viewpoint of these pictures is set to infinity, to show a full hemisphere of solid angle. The bottom row is the corresponding smooth contour plot, with a finite viewpoint so as to highlight the straight edges and 5-fold rotation symmetry about the vertices.	64

4.11	Histograms of bond curvature c_b for the average cluster shape (solid lines) and the instantaneous cluster configurations (dashed lines) at (a) $T = 600\text{K}$, (b) $T = 900\text{ K}$, (c) $T = 1060\text{ K}$, and (d) $T = 1100\text{ K}$. The cluster size is $N = 2624$ atoms.	67
4.12	Histograms of maximal surface curvature κ_M of the average cluster shape (solid lines) and the instantaneous cluster configurations (dashed lines) at (a) $T = 600\text{K}$, (b) $T = 900\text{ K}$, (c) $T = 1060\text{ K}$, and (d) $T = 1100\text{ K}$. The cluster size is $N = 2624$ atoms.	68
4.13	Average cluster shapes for an $N = 1409$ atom cluster at temperatures 800 K and 900 K , where $T_m \simeq 925\text{ K}$. Points are shaded according to the value of the maximal curvature; the darker the gray scale, the larger the curvature.	69
4.14	Average cluster shapes for an $N = 5082$ atom cluster at temperatures 1000 K and 1140 K , where $T_m \simeq 1150\text{ K}$. Points are shaded according to the value of the maximal curvature; the darker the gray scale, the larger the curvature.	69
4.15	Interlayer mixing parameter $\langle n \rangle$ vs. T , for atoms initially on the surface, in the first sub layer, . . . , and in the interior. The cluster size is $N = 2624$ atoms.	70
4.16	Mean squared displacements for the $N = 2624$ atom cluster averaged over the atoms in the surface layer, first through fourth sub layers, and interior for (a) 600 K , (b) 900 K , (c) 1060 K , and (d) 1100 K . . .	71
4.17	Diffusion coefficients D vs. T for different layers of the $N = 2624$ atom cluster. The inset shows an expanded range for D in a temperature range below melting, $700 - 1050\text{ K}$	72
4.18	Number of moved atoms for the cluster with $N = 2624$ atoms in the surface layer, first through fourth sub layers, and the interior with the cutoffs of (a) 3.8 \AA , (b) 6.1 \AA , and (c) 8.0 \AA	75

4.19	Number of moved atoms for the cluster with $N = 1409$ atoms in the surface layer, first through fourth sub layers, and the interior with the cutoff of 8.0 \AA	76
4.20	Number of moved atoms for the cluster with $N = 5082$ atoms in the surface layer, first through fourth sub layers, and the interior with the cutoff of 8.0 \AA	76
4.21	Ellipsoids of displacement at 400, 600, 900, 1060 and 1100 K for the cluster of $N = 2624$ atoms. Each ellipsoid is centered at the average position of the given atom, and shows the directional distribution of root mean squared displacements. The top row gives results obtained for a simulated time of 1.075 ns, while the bottom row is for 4.3 ns. .	80
5.1	Instantaneous temperature vs. time during continuous heating of the gold nanorod with $N = 2624$ atoms.	83
5.2	Snapshots from a continuous heating run of a gold nanorod with 2624 atoms at temperatures of 5, 515, 1064, and 1468 K.	85
5.3	Temperature dependence of (a) total and potential energy and (b) the radius of gyration for the $N = 2624$ atom rod during continuous heating with a heating rate of $7 \times 10^{12} \text{ K/s}$. The letter A indicates the onset of the shape transformation and the letter B indicates the onset of the melting transition.	86
5.4	Temperature dependence of bond order parameters averaged over the internal atoms for the gold nanorod with 2624 atoms during continuous heating with a heating rate of $7 \times 10^{12} \text{ K/s}$	87
5.5	Temperature dependence of (a) the radius of gyration and (b) the average bond order parameters for internal atoms, for the $N = 2624$ atom rod during continuous heating with a rate of $2.1 \times 10^{13} \text{ K/s}$. . .	89

5.6	Temperature dependence of (a) the radius of gyration and (b) the average bond order parameters for internal atoms, for the $N = 2624$ atom rod during continuous heating with a rate of 2.3×10^{12} K/s. . .	90
5.7	Temperature dependence of (a) the radius of gyration and (b) the average bond order parameters for internal atoms, for the $N = 7552$ atom rod during continuous heating with a rate of 7×10^{12} K/s. . . .	91
5.8	Temperature dependence of (a) the radius of gyration and (b) the average bond order parameters for internal atoms, for the $N = 11\,076$ atom rod during continuous heating with a rate of 7×10^{12} K/s. . . .	92
5.9	The temperatures of the onsets of the shape transformation (T_s) and melting transition (T_m) for gold nanorods of various sizes. These temperatures were determined by visual inspection of the R_g vs. T curves as indicated by the arrows A and B in Fig. 5.3b.	93
5.10	Order parameters Q_4 and \hat{W}_4 for internal atoms in a set of structures of the 2624-atom gold nanorod at $T = 691$ K. The atoms with $Q_4 < 0.13$ and $\hat{W}_4 > 0.07$ are considered atoms with local hcp structure. Those with $Q_4 > 0.17$ and $\hat{W}_4 < -0.10$ are atoms with local fcc structure. .	95
5.11	Fractions of surface atoms and internal atoms with fcc, hcp, and “other” local structures vs. temperature for the gold nanorod with 2624 atoms.	96
5.12	Cross sections of the $N = 2624$ atom gold nanorod at different temperatures with atoms colored according to their local structure: fcc is yellow, hcp is green, and “other” is gray.	98
5.13	Motion of atoms during the shape transformation. The initial configuration is at 511 K and the final configuration is at 794 K.	99

6.1	Radius of gyration for the quasi-equilibrium heating (lower curve). Dotted vertical lines represent constant temperature bins. The values in each bin are the time evolution of radius of gyration through a constant temperature MD at a fixed temperature given by the leftmost (smallest) temperature of the bin. For comparison, the upper curve is the radius of gyration for the continuous heating of the same rod (the same curve in Fig. 5.3b).	104
6.2	Bond orientational order parameters for the internal atoms. Dotted vertical lines represent constant temperature bins. The values in each bin are the time evolution of radius of gyration through a constant temperature MD at a fixed temperature given by the leftmost (smallest) temperature of the bin.	106
6.3	Caloric curves for quasi-equilibrium heating (closed circles) and continuous heating (dotted line) of the gold nanorod with $N = 2624$ atoms, and for the equilibrium simulations of the Ih gold cluster with $N = 2624$ atoms (open circles).	107
6.4	(a) The surface of the constructed gold nanorod. (b) The second sublayer of a configuration in the intermediate state at $T = 900$ K. The atoms are colored by their 2D local surface structure: $\{111\}$ is yellow, $\{100\}$ is green, $\{110\}$ is red, and “other” is gray.	110
6.5	Cross sections of (a) the initial constructed rod and (b) the intermediate state at $T = 900$ K. The atoms are colored by their 3D local structure: fcc is yellow, hcp is green, and “other” is gray.	111
6.6	Two possible piling positions of a hexagonal plane represented by solid circles and crosses, respectively.	111
6.7	(a) The constructed rod cut along the $[\overline{111}]$ direction. (b) The cross section of the cut surface. Green atoms lie on the surface of the rod, and yellow atoms lie in the interior.	112

6.8	Average cross-sectional shape of the gold nanorod at different temperatures. At each temperature the averaging is over the side atoms of the 1000 configurations sampled in the simulated time of 43 ns. . . .	114
6.9	Histograms of bond curvature c_b for the instantaneous configurations of the rod at different temperatures.	116
6.10	Bond orientational order parameters of the (a) surface, (b) first sub layer, (c) second sub layer, (d) third sub layer, (e) fourth sub layer, and (f) interior of the rod vs. temperature.	117
6.11	Snapshots of the surface (left column) and the second sub layer (right column) of the rod at different temperatures. The atoms are colored according to their local 2D surface structure: $\{111\}$ is yellow, $\{100\}$ is green, $\{110\}$ is red, and “other” is gray.	119
6.12	Cross sections of a gold nanorod with $N = 2624$ atoms at different temperatures along the $x = 0$ plane (left) and along the $y = 0$ plane (right). The atoms are colored according to their local structure: fcc is yellow, hcp is green, and “other” is gray.	121
6.13	Inter-layer mixing parameter $\langle n \rangle$ vs. T , for atoms initially in the different layers and the interior of the gold nanorod with $N = 2624$ atoms.	122
6.14	Diffusion coefficients D vs. T for different layers and the interior of the $N = 2624$ atom rod.	123

1. INTRODUCTION

Due to their large surface-to-volume ratio, nanocrystals generally have drastically different fundamental physical properties from their corresponding bulk materials. This allows nanocrystals to be applied in various new kinds of applications. Among noble metals, gold (Au) nanomaterials are especially useful, mainly due to their high thermal stability, exceptional optical properties, and good electronic conduction. Because the plasmon absorption bands of gold nanoparticles depend on their shape and size, particle aggregation of such nanoparticles result in a red-shift of their spectra. This property has been widely used to detect materials that can induce the aggregation of gold nanoparticles, such as DNA [1], proteins [2], and metal ions [3]. By binding to DNA scaffolds, gold nanoparticles can form the building blocks of nanoscale electronic devices [4]. Colloidal gold nanoparticles have been used as a nano-oxidation mask in nanolithography, since the gold nanoparticles can form strong chemical bonds with the silicon substrates to prevent the covered area from being indented by the atomic force microscopy tip scanning [5]. Titania-supported gold nanoparticles in the range of 2–3 nm are very active for the oxidation of CO to CO₂, which makes them important for the catalysis industry [6]. In addition to spherical-like nanoclusters, rod shaped gold nanoparticles (denoted as gold “nanorods”) have advantages in electronic devices applications, because the chemical reactivity of nanomaterials are found to depend not only on their sizes, but also on their shapes [7].

To support such wide applications, knowledge of the structure and stability of gold nanoparticles is of great importance. While bulk gold has a face-centered-cubic (fcc) crystal structure, because of the competition between bulk and surface energies, nanometer sized gold crystallites can have several different competing structures,

such as decahedron, Mackay icosahedron, cuboctahedron, and truncated octahedron [8, 9, 10]. A detailed description of these structures will be given in Section 2.2.

One such structure which has been observed both in simulations [11, 12] and in experiments [8, 13] is the “Mackay icosahedron” [14, 15], which we will also denote as the “Ih structure”. It is made up of 20 fcc tetrahedra, each of which is built up layer by layer by hexagonal planes. The tetrahedra are combined to form an icosahedral shaped structure. The internal surfaces of the tetrahedra meet at twin planes with a local hexagonal-close-packed (hcp) structure, and the twin planes meet at edges, whose particles form an axis with 5-fold rotation symmetry. The external surfaces of the tetrahedra are $\{111\}$ surface facets. A picture of such an Ih structure is shown in Fig. 2.4. This structure will be the subject of our investigations in Chapter 4.

Theoretical models have predicted different limits for the stability of the Ih structure. The well known Wulff construction [16] can obtain the equilibrium shape of a single crystal by applying the constraint of constant volume and minimizing the surface free energy. However, this method is based on continuum concepts and is therefore appropriate only for very large clusters. Ino predicted that the Ih structure is stable up to cluster sizes of 40 000 atoms [17]. Marks gave similar limits by using a modified Wulff construction [13, 18]. Energetic atomistic calculations at $T = 0$ show that Ih structures are preferred only for gold clusters with tens of atoms [19, 20, 21]. However, these calculations lack entropic effects which might become important at finite temperatures. Chushak and Bartell [11] found Ih gold clusters of up to 4000 atoms in molecular dynamics (MD) simulations of the cooling of liquid drops. Furthermore, Cleveland *et al.* [22] found, in MD simulations, that upon heating gold clusters consisting of hundreds of atoms, a diffusionless solid-to-solid transition occurred from the low temperature optimal structures (truncated decahedra and truncated octahedra) to the Ih structure, as the precursor of bulk melting.

It remains unclear whether the formation of Ih structures is an equilibrium or rather a kinetic process. Nevertheless, it is natural to suppose that the formation of this structure is related to the very high stability of the $\{111\}$ surface facets. Simulations [23] and experiments [24] on bulk slab-like geometries of gold with exposed $\{111\}$ surfaces have shown that, unlike the $\{100\}$ and $\{110\}$ surfaces which melt below the bulk melting temperature T_m , the $\{111\}$ surface does not melt up to the bulk melting temperature T_m , and can in fact lead to superheating of the solid [25]. In light of this observation it is interesting to consider how the high stability of the $\{111\}$ facets effects the melting and equilibrium shape of such icosahedral clusters. Investigating the melting of such Ih gold clusters by MD simulations will be one of the main subjects of this thesis.

While the effects of size on the physical properties of gold nanoparticles are relatively well documented, less is known about the effects of shape and surface structure. Recently, however, several groups have been investigating the dependence of optical and electronic properties on such cluster geometry [26, 27]. In particular, Chang *et al.* [28] and Link *et al.* [29, 30] have explored the stability and structure of gold nanorods with various aspect ratios.

In these experiments, laser pulses are used to selectively heat gold nanorods, essentially without affecting their environment. Because the energy delivered to the particles by the laser is selected to be under the threshold for complete melting, intermediate products with various shapes can be observed. In particular, bent, twisted, shorter and wider, and ϕ -shaped intermediates were found in these experiments [28, 29]. A transmission electron microscopy (TEM) image showing the intermediate shapes is shown in Fig. 1.1. Furthermore, TEM studies also observed that point and planar internal defects appear inside gold nanorods as they undergo such shape transformations [30]. The corresponding high-resolution TEM (HRTEM) images are shown in Fig. 1.2. Computer simulations to clarify the mechanisms involved in these processes will be the second subject of this thesis.

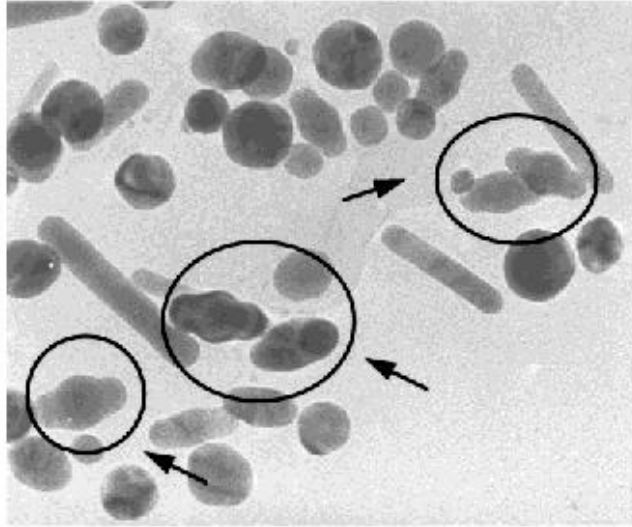


Fig. 1.1: TEM image of gold nanorods after exposure to nanosecond laser pulses. Nanoparticles having the ϕ -shape are highlighted by circles. Courtesy of Link et al. from Ref. [29].

The remainder of this thesis is organized as follows. In Chapter 2 we will overview the previous research on gold clusters and gold nanorods. In Chapter 3 we will describe the simulation and data analysis methods that we use. In Chapter 4, we will show by MD simulations that liquid gold clusters with about 600–3000 atoms crystallize to a Mackay icosahedral structure upon cooling from the liquid. We then heat the clusters up until above their melting temperatures T_m to observe their thermal stability and melting behavior. We find no surface premelting or roughening for the $\{111\}$ facets of our Ih clusters. Nevertheless, we find that there is a considerable softening of the cluster surface roughly ~ 200 K below T_m due to the motion of atoms along the vertices and edges of the cluster. In this temperature range we find both intra-layer and inter-layer diffusion of atoms, which increases as T_m is approached. The average shape evolves from fully faceted, to faceted with rounded edges, to nearly spherical just below T_m . Throughout this region, the interior atoms of the cluster remain essentially perfectly ordered, until T_m is reached.

In Chapter 5, we report on MD simulations of the morphological and structural behavior of gold nanorods during *continuous heating* from 5 K to complete melting, and compare our findings with experimental results. Our results indicate that gold nanorods melt in two stages: a shape transformation at lower temperature in which the rods shrink to a shorter and wider intermediate shape, followed by the melting transition to liquid nanospheres. Both surface and internal atoms undergo structural change during the whole process. Surface disordering and reordering was also observed. During the continuous heating, our simulated gold nanorods go through bent, twisted, shorter and wider shapes, and exhibit planar defects, which might correspond to the experimentally observed states.

In Chapter 6, we will show results for the same gold nanorod with $N = 2624$ atoms from a “quasi-equilibrium heating” procedure, which heats the rod up temperature by temperature by *constant temperature* MD. This procedure gives qualitatively the same conclusions as the continuous heating one, but with more detailed results. From those results, we conclude that the stable intermediate shorter and wider rod at higher temperatures has a pure fcc body and four elongated hexagonal gold $\{111\}$ facets on the sides. Initiated by the surface change, the initial bulk of the crystal restructures itself so that the crystal orientation of the intermediate state rod is consistent with the $\{111\}$ facets on its surface. This reconstruction is via a random stacking of the interior. A detailed mechanism of the morphological and structural changes of the gold nanorods will then be suggested to explain the experimental observations.

In Chapter 7, we will discuss and summarize our findings for gold Ih clusters and gold nanorods. Suggestions for possible future work will also be given.

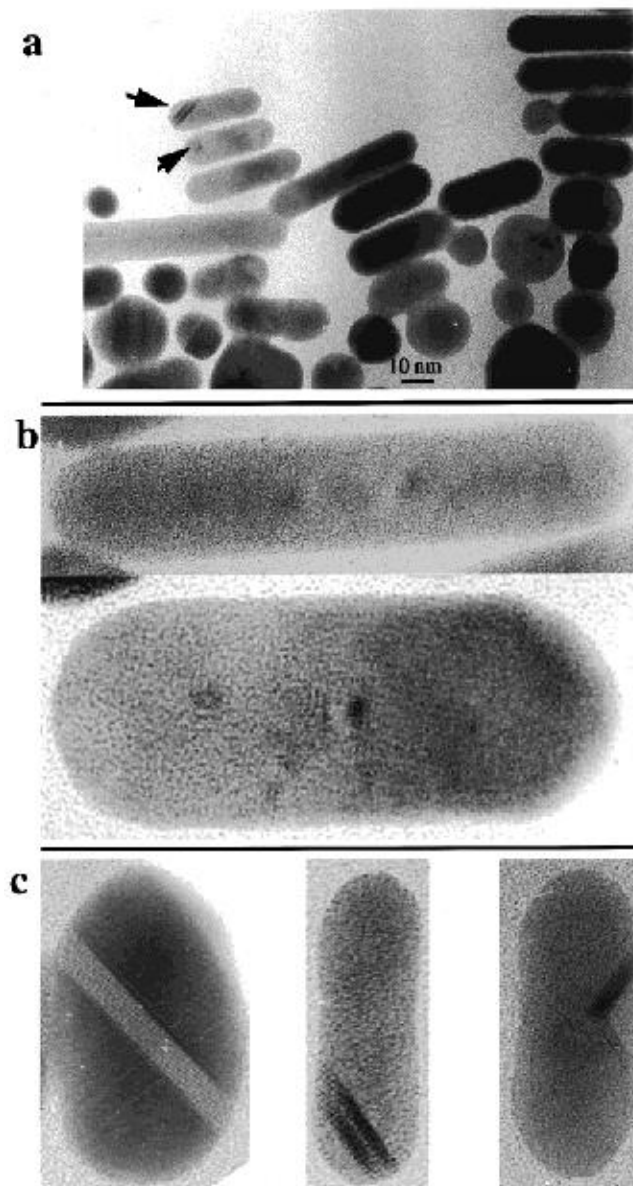


Fig. 1.2: HRTEM images of gold nanorods after exposure to femtosecond laser pulses. The arrowheads in (a) indicate the nanorods with point defects and twins. Those individual particles are further enlarged in (b) two nanorods with point defects, and (c) twinned particles. Courtesy of Link et al. from Ref. [30].

2. OVERVIEW OF RESEARCH ON GOLD NANOMATERIALS

In this chapter we review some basic facts about bulk gold and macroscopic slab-like gold surfaces, and previous work on gold nanomaterials, that will form the background for our investigations. A brief description of several nanocrystal structures will also be given.

2.1 Bulk Gold

In this section we use the word “bulk” to refer to a macroscopic large sample with a number of atoms of the order $\sim 10^{23}$. Later on we will also use “bulk” to refer to the interior of the nanocrystals. The meaning of this word should be unambiguous everywhere according to the context.

It is well known that the bulk melting temperature of gold is 1337 K [31], and that bulk gold has a fcc crystalline structure. In Fig. 2.1 we show a cubic cell of the fcc structure and indicate the orientation of the three low-index planes, $\{100\}$, $\{110\}$, and $\{111\}$, that are of interest for our studies.

The periodic duplication of these three unit planes forms the corresponding three low-index surfaces. In Fig. 2.2 we show pictures of gold $\{110\}$, $\{100\}$, and $\{111\}$ surfaces. From the pictures we see that the gold $\{110\}$ surface has a rectangular lattice with a large interatomic distance. The gold $\{100\}$ surface has a square lattice. The gold $\{111\}$ surface has a hexagonal lattice which is close-packed.

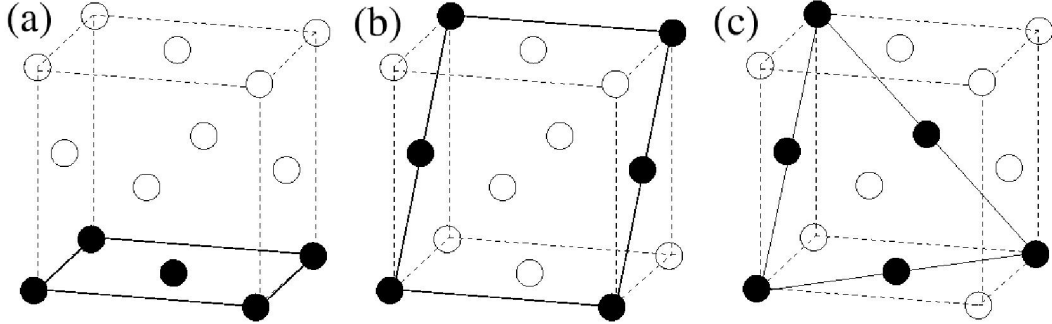
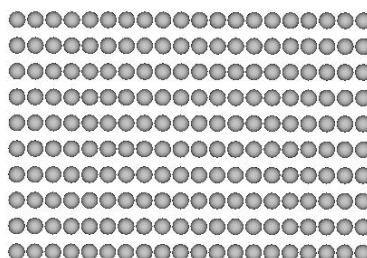


Fig. 2.1: Three low-index planes of the fcc structure: (a) $\{100\}$, (b) $\{110\}$, and (c) $\{111\}$. The involved particles are in black.

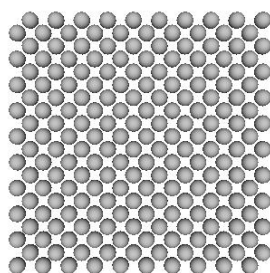
A long time ago a mechanism was suggested that the nucleation of melting in crystals happens first on the surface, then propagates into the bulk [32, 33]. This scenario has been verified in some recent experiments. Frenken and van der Veen [34] reported that the Pb $\{110\}$ surface starts to melt at approximately 40 K below the bulk melting temperature T_m , and the liquid surface thickens quickly as the temperature approaches T_m . Denier van der Gon *et al.* [35] found that surface melting occurs on the Al $\{110\}$ surface, and that the liquid layer thickness increases logarithmically with temperature.

More surface phenomena than melting can take place below the bulk T_m . According to Ref. [25], the most popular ones are:

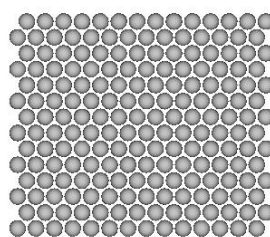
- *Relaxation.* Due to the fact that surface atoms have less neighboring atoms, the top-most planes rearrange the distances between them without changing the in-plane structure.
- *Reconstruction.* Surface atoms may also rearrange to form new bonds. After reconstruction, the surface free energy is lower, and the surface will have a different in-plane structure. The surface relaxation and reconstruction usually give the most stable state at $T = 0$.
- *Deconstruction.* As temperature increases to a certain point, the entropy is big



(a) Gold {110}



(b) Gold {100}



(c) Gold {111}

Fig. 2.2: Pictures of three low-index gold surfaces: (a) gold {110}, (b) gold {100}, and (c) gold {111}.

enough to remove the order of the reconstructed surface, and lead to a deconstruction phase transition.

- *Pre-roughening.* Some surfaces that do not reconstruct and deconstruct may have a pre-roughening transition. At the transition point, the surface becomes disordered but remains flat.
- *Roughening.* At a certain temperature above the transition point of deconstruction or pre-roughening, a roughening transition may occur. Above the roughening temperature T_R , the root mean square width of surface height fluctuations increases with the length of the surface.
- *Wetting.* Further increasing the temperature, the surface atoms on the roughened surface form a thin quasi-liquid film, because the bindings between layers are weak, and atoms diffuse. The wetting temperature is defined as where the first nucleation of liquid happens.
- *Melting* Above the wetting temperature, the thickness l of the quasi-liquid film grows with temperature. Melting occurs at the temperature T_m when l diverges.

However, surface melting does not happen on all kinds of crystal surfaces. Reported in the same paper Ref. [35], the Al {111} surface does not melt below the bulk T_m . Pb {111} is found to be stable even above the bulk T_m [36]. According to their melting behavior, crystal surfaces can be roughly classified into three categories [25]: (i) *Melting surface*: the surface forms a thin quasi-liquid film at a temperature well below the bulk T_m , its thickness l grows with temperature, and l diverges when the temperature reaches the bulk T_m . (ii) *Nonmelting surface*: the surface does not melt up to the bulk T_m . (iii) *Incomplete melting surface*: the surface may melt and develop several liquid layers as temperature increases, but the thickness of the liquid does not diverge as the bulk T_m is approached.

Much research effort has considered the thermal stability of low-index gold surfaces. Experiments done by Hoss *et al.* [37] concluded that the Au {110} surface

roughens at 680 K, and melts at 770 K. MD simulations of this surface with the interatomic “glue” model [38] performed by Ercolessi *et al.* [39] found that a liquid-like surface disorder appears near $T \simeq 1000$ K, below the $T_m = 1357$ K given by the glue model. In both cases the thickness of the liquid film grows with temperature and diverges at the bulk T_m . In contrast, again using MD simulations with the glue model, Carnevali *et al.* [23] found that the well-packed Au {111} surface does not melt up to the bulk T_m . Some experiments indicate that the Au {111} surface has no surface melting up to at least 1250 K [40, 41]. These results show that the Au {111} surface is a nonmelting surface. Unlike these two surfaces, X-Ray experiments [31, 42] observed that the Au {100} surface exhibits a thin, disordered surface film at $T > 1170$ K, but that the thickness of the film does not grow with temperature. The glue model simulation by Bilalbegović and Tosatti [43] also found this incomplete melting feature of Au {100}. From Fig.2.2 we see clearly that larger interatomic distances lead to higher surface energy, and thus poorer surface stability.

As expected from the thermal stability of gold surfaces, some experiments [44, 45] observed that, at temperatures around 1200 K, the surface of an equilibrium pure gold crystal of size $\sim 5 \mu\text{m}$ ($\sim 10^{13}$ atoms) is composed of {111} and {100} facets, connected to rounded surfaces by sharp edges. The unstable {110} facets are absent on the equilibrium gold crystal surface.

2.2 Structures of Nanoclusters

In this section we review some of the structures that have been suggested for crystalline nanoparticles. Because the hexagonal planar lattice is a close-packed structure, crystals always prefer to have their external surfaces covered by such hexagonal planes. However, when the surface area and the internal strain are taken into account, the competition between these effects can result in different kinds of crystalline structures. Some crystalline structures commonly found for noble metal nanoclusters include the Mackay icosahedron, decahedron, truncated decahedron, octahedron,

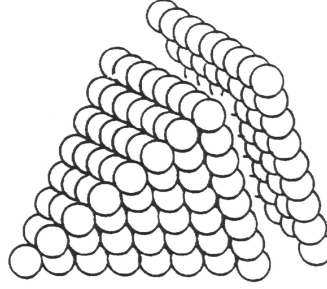


Fig. 2.3: A tetrahedron is built up layer by layer by hexagonal planes. Courtesy of Martin from Ref. [15].

truncated octahedron, and cuboctahedron, a specific form of truncated octahedron. We now briefly describe these structures, following the discussion in Ref. [15].

The Mackay icosahedron, or “Ih” structure, is made up of 20 fcc tetrahedra, each of which is built up layer by layer by hexagonal planes. A tetrahedron is shown in Fig. 2.3. The tetrahedra are combined to form an icosahedral shaped structure. The internal surfaces of the tetrahedra meet at twin planes with a local hcp structure, and the twin planes meet at edges, whose particles form an axis with 5-fold rotation symmetry. The external surfaces of the tetrahedra are $\{111\}$ surface facets. For an Ih structure with L shells (the central atom is denoted as $L = 0$), the magic number of atoms needed to construct a perfectly symmetric ideal icosahedron is,

$$N_L = \frac{10}{3}L^3 + 5L^2 + \frac{11}{3}L + 1. \quad (2.1)$$

In Fig. 2.4 we show the atomic configuration for an ideal Ih structure with the magic number of $N = 2869$ atoms ($L = 9$). Atoms are shaded to indicate local fcc, hcp, and “other” structure, which correspond to the facets, edges, and vertices on the surface of the cluster.

The icosahedron contains 20 tetrahedra built up by hexagonal planes, and is the most symmetric among all discrete point groups. However, it is a highly strained structure with the inter-layer interatomic distances smaller than the intra-layer ones.

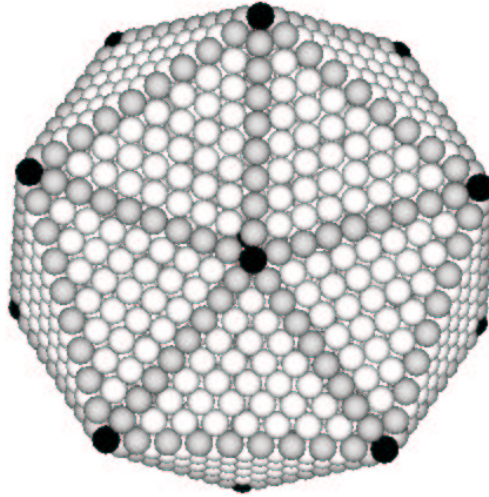


Fig. 2.4: An ideal I_h structure with the magic number of 2869 atoms. Atoms are shaded to indicate their local structure: fcc is white, hcp is gray, and “other” is black.

This suggests that the icosahedron is preferred by relatively small clusters with a high surface-to-volume ratio.

The decahedron also has a fivefold rotation symmetry. As shown in Fig. 2.5a, if we simply pack five tetrahedra together by sharing a common edge to build a decahedron, a gap appears. Alternatively, a perfect decahedron with internal strains can be built by allowing the tetrahedra to deform. Unlike the icosahedron whose layers are all centered at the center of mass, a decahedron grows its umbrella-like layers with the common vertex at the bottom, as shown in Fig. 2.5b. The total number of atoms in a decahedron with L shells is,

$$N_L = \frac{5}{6}L^3 + \frac{5}{2}L^2 + \frac{8}{3}L + 1. \quad (2.2)$$

Although the surface atoms are close-packed, the decahedron is not preferred at any cluster size because of the large surface area and internal strain. A truncated decahedron can partly take the advantage of a close-packed surface while having a more spherical-like shape to reduce the surface area. There are several ways to

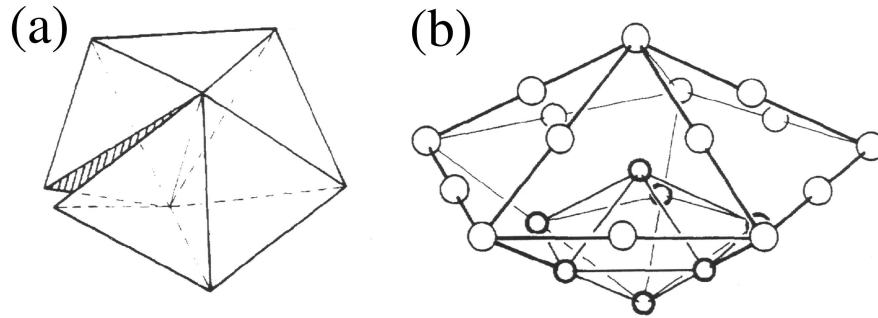


Fig. 2.5: (a) Five tetrahedra sharing an edge form a decahedron with a gap. (b) A decahedron built up by adding umbrella-shaped partial layers with a common vertex at the bottom. Courtesy of Martin from Ref. [15].

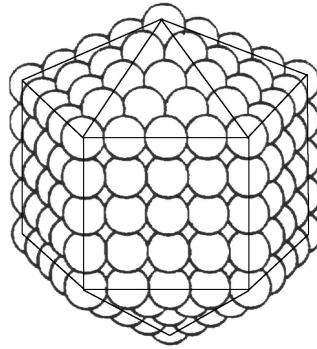


Fig. 2.6: A 309-atom truncated decahedron with square {100} facets. Courtesy of Martin from Ref. [15].

truncate the decahedron. One truncated decahedron with square {100} exposed surfaces is shown in Fig. 2.6. The total number of atoms in a truncated decahedron with L shells is,

$$N_L = \frac{10}{3}L^3 + 5L^2 + \frac{11}{3}L + 1. \quad (2.3)$$

A tradeoff for the more spherical-like shape is that the exposed {100} facets are not close-packed, and thus have a higher surface energy than {111} facets.

In contrast to the Ih structure and the decahedron, an octahedron is cut out of a pure fcc crystal, and is thus free of internal strain. The triangular facets of the

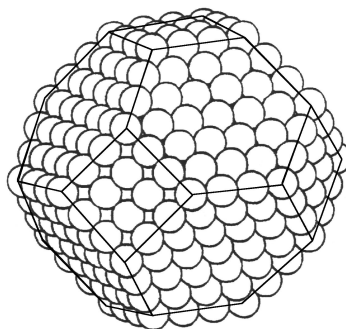


Fig. 2.7: A 586-atom truncated octahedron with square and hexagonal facets. Courtesy of Martin from Ref. [15].

octahedron are built up of only $\{111\}$ planes to have a low surface energy. The total number of atoms in an octahedron with L shells is,

$$N_L = \frac{2}{3}L^3 + 2L^2 + \frac{7}{3}L + 1. \quad (2.4)$$

Nevertheless, the octahedron is far from spherical, resulting a large surface area. Thus a truncated form of it is always preferred. The octahedron can be truncated in several ways. In Fig. 2.7 the sharp corners of the octahedron are truncated, leaving square $\{100\}$ and hexagonal $\{111\}$ facets on the surface.

If the octahedron is truncated by a cube, it forms a cuboctahedron (cube-octahedron) with six square $\{100\}$ facets and eight triangular $\{111\}$ facets. Although the square facets are not close-packed, it has the advantage that the total surface area is small. A cuboctahedron is shown in Fig. 2.8. The total number of atoms in a cuboctahedron is,

$$N_L = \frac{10}{3}L^3 + 5L^2 + \frac{11}{3}L + 1. \quad (2.5)$$

2.3 Gold Nanoclusters

As the size of atomic clusters scales down to the order of nanometers, the large surface-to-volume ratio causes the surface to play a more important role than merely

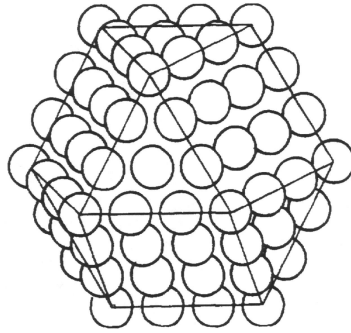


Fig. 2.8: A 147-atom cuboctahedron. Courtesy of Martin from Ref. [15].

as the possible nucleation source of bulk melting. In this size range the surface free energy is comparable to that of the interior. The balance of surface and interior free energies enables the nanoclusters to be equilibrated into several different kinds of crystalline structures, even nonperiodic and twinned ones, which would not be stable as macroscopic crystals. In particular, multiply twinned structures, such as the decahedra and the Ih structures, are sometimes favored by nanoclusters, because the energy expense of the strain caused by their internal twin planes can be compensated by the lower total surface energy gained from the lower energy $\{111\}$ facets, than the other facets one would have on simple single crystals.

Depending on the method of preparation, substrate, and other experimental conditions, gold nanoclusters with different structures have been observed in experiments. Grown from metal ions reduced at the oil-water interface, Ascencio *et al.* [8] found that gold clusters of the sizes of 10–20 Å (< 300 atoms) form fcc, decahedral, Ih, and amorphous structures. Pauwels *et al.* [9] produced Au clusters with diameters ~ 2 nm (~ 300 atoms) in a laser vaporization source and deposited on carbon-coated microscope grids with MgO substrates. Studied by HRTEM, they found cuboctahedral and decahedral clusters on carbon, and truncated octahedra on MgO. Tehuacanero *et al.* [10] prepared samples by a vacuum evaporation method with a NaCl substrate. The gold nanoclusters they obtained are with the size of less than 3 nm and with asymmetric decahedral and Ih crystal structures.

MD simulations have also found different structures for gold nanoclusters, when using various kinds of potential models. Wilson and Johnston [46] performed a continuous cooling MD procedure with the Murrell-Mottram potential on Au clusters consisting of 2–40 atoms and predicted global minimal structures of octahedra, decahedra, icosahedra, and hexagonal prisms (the last is shown in Fig. 2.9) for different sizes of gold nanoclusters. Chushak and Bartell [11, 47] used the embedded-atom-method (EAM) interaction potential [48] with a typical simulated equilibration time of 250 ps to study gold nanoclusters with several sizes from 459 to 3943 atoms. They found that upon cooling, most of the frozen clusters formed with an Ih structure, but imperfect truncated decahedra, twinned truncated octahedra, and hcp structures were also present. Employing a modified EAM, with a simulated 200 ps at each temperature, Shim *et al.* [49] found a truncated octahedron for gold clusters containing 140–6708 atoms. In agreement with experimental X-ray data, Cleveland *et al.* concluded from MD simulations with the EAM model that gold nanoclusters in the size range of about 1–2 nm (40–250 atoms) have a truncated-decahedral structure [20], and those in the size range of about 1.4–3.0 nm (100–1000 atoms) have a decahedral or truncated-octahedral structure [19]. Recently Nam *et al.* [12] found, by a continuous cooling MD procedure with the EAM potential, that gold nanoclusters with about 500–1000 atoms crystallize to an Ih structure. In contrast, by MD simulations with the glue potential, Ercolessi *et al.* [50] claimed that gold nanoparticles with $N \sim 100$ –1000 atoms favor cuboctahedral structures at $T = 0$.

Because the energy barriers between different structures are small, gold nanoclusters with less than about 1000 atoms can fluctuate between different crystal structures. Iijima and Ichihashi [51] irradiated gold particles of about 2 nm in size (~ 300 atoms) by an electron beam, and observed a continuous shape change accompanying the internal structural change between fcc, cuboctahedra, Ih, decahedra, and other structures. Cleveland *et al.* [22] observed in MD simulations with the EAM potential and a simulated time of about 1 ns, that the low-temperature optimal truncated



Fig. 2.9: A hexagonal prism gold nanocluster with 30 atoms. Courtesy of Wilson and Johnston from Ref. [46].

decahedra for $N = 75$ and $N = 146$ atoms, and fcc with a truncated-octahedral shape for $N = 459$ atoms, went through solid-to-solid structural transformations to Ih structures well below the bulk T_m . The fluctuation between different structures has also been verified by calculations of the Gibbs free energies done by Ajayan and Marks [52].

Despite various types of crystal structures and the uncertainty of their stability limits, it is in general agreement that the melting temperature T_m decreases with cluster size. Takagi [53] first observed experimentally that the melting points are lower for small metal crystals. Buffat and Borel [54] confirmed the size dependence of gold clusters by experiments, and their results are shown in Fig. 2.10. This phenomenon is verified by all of the simulation works (e.g. Refs. [49, 50, 55, 56]).

Whether the surface will premelt below the bulk melting temperature T_m in nanoclusters has been a topic of great interest. Monitoring both atomic diffusion and the pair correlation function, several theoretical works have studied the surface melting behavior in MD simulations. Surface premelting has been claimed to occur for truncated octahedra [49], cuboctahedra [50], and carved-out fcc spheres [55]. Since for bulk slab-like gold surfaces, only gold $\{111\}$ is a nonmelting surface, Ercolessi *et al.* [50] attribute the surface premelting of these structures to the presence of non- $\{111\}$ facets on these structures. They asserted that Ih structures, where only $\{111\}$ facets are present, should not have surface premelting. However, Liu *et al.* [56] claimed

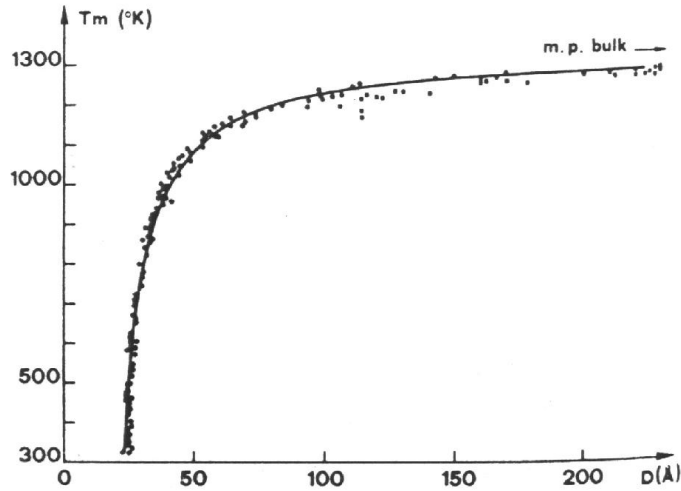


Fig. 2.10: Experimental values of the bulk melting temperature T_m of gold particles. The horizontal axis is the diameter of the particle in Å. The solid line is a theoretical fit to the experimental data. Courtesy of Buffat and Borel from Ref. [54].

that they observed surface premelting not only for cuboctahedra and several kinds of decahedra, but also for the Ih structures.

According to the melting temperature shown in Fig. 2.10, we may roughly divide gold nanoclusters into three categories according to their size. *Small* gold nanoclusters are those with less than several hundreds of atoms (diameter $d < 3$ nm). The melting temperatures T_m of these clusters increase drastically with size. The energy barriers between different crystal structures are very low, so that the clusters can easily undergo solid-to-solid structural changes. *Medium* gold nanoclusters are those with thousands of atoms ($d \sim 3$ –8 nm). These clusters have a mild increasing of T_m with size, and are more stable in structure. *Large* gold nanoclusters are those with more than ten thousands of atoms ($d > 8$ nm), whose T_m grow slowly with size, approaching the bulk melting temperature. The energy barriers between different stable structures are large, so that it is difficult for these clusters to undergo a solid-to-solid structural change.

Various sizes of gold nanoclusters have been used in different applications. Small ones with $d \sim 2\text{--}3$ nm were used as catalysts [6] and building blocks for electronic devices [4]. Lithium ion detection employed medium-sized gold nanoparticles with $d = 4$ nm [3], and 5 nm particles were used to detect DNA arrays [1]. Even much larger gold nanoparticles have their applications as a nano-oxidation mask ($d \sim 20$ nm) [5] and as a part of bio-bar-codes ($d \sim 30$ nm) [2].

From the above we see that most experimental and theoretical effort has been put on gold nanoclusters with sizes of less than several hundred atoms ($d < 3$ nm). Some simulation works (e.g. Refs. [11, 47, 49]) extended the size to thousands of atoms. However, larger clusters require more time to equilibrate. Thus although their simulated time of ~ 200 ps may be enough for small clusters, it makes their results about the medium-sized clusters questionable.

Stimulated by these works, in Chapter 4 we will present our results on MD simulations to study the equilibrium properties of the gold nanoclusters with $N = 600\text{--}5000$ atoms. We will show that the Ih structure is the thermally favored crystalline structure in this size range when cooling from the melt. Our simulated time of 43 ns at each temperature is tens of times longer than previous simulations to ensure better equilibration. We present for the first time calculations of surface curvature, average cluster shape, and a visualization of surface atom movement, in order to provide a more quantitative microscopic description of cluster behavior. Computing average shapes, instead of instantaneous fluctuating configurations, will give a better understanding of shape evolution with temperature. In contrast with the conclusion drawn by Liu *et al.* [56], we will also show that Ih gold nanoclusters do not have complete surface melting below T_m , although the diffusion of some surface atoms is liquid-like for some temperature range of $T < T_m$. The numeric tools developed in this project can be valuable for other studies of nanomaterials.

2.4 Gold Nanorods

In addition to studying the size dependence of physical properties of nanoclusters, recent research works have also been directed to find out how the shape of nanomaterials effect their physical properties.

The growth of gold nanorods has been, and still is, a very active field in experimental chemistry. Wang *et al.* [57] synthesized gold nanorods electrochemically using micelles as a capping material. The products fall into two categories: short gold nanorods with aspect ratios of 3–7 and widths of ~ 20 nm, and long gold nanorods (sometimes also called nanowires) with aspect ratios of 20–35 and widths of ~ 100 nm. Yacamán *et al.* [58] produced gold nanorods with an aspect ratio of ~ 8 and width of ~ 11 nm by a bioreduction process. Zhu and Hu [59] prepared gold nanorods and nanowires with widths of ~ 60 nm and lengths ranging from $0.5 \mu\text{m}$ to $6 \mu\text{m}$ by a one-step, seedless and template-free microwave-polyol method. Using seed-mediated growth procedures, Jana *et al.* [60] obtained gold spheroids with aspect ratios of 4.6, 13, and 18, all having a width of 16 nm. Most recently, some groups have been improving the seed-mediated growth methods to grow longer gold nanorods in a more controlled fashion [61, 62, 63, 64, 65, 66, 67].

Despite the large number of experiments, only a few groups have reported on both the surface and internal structure of their synthesized gold nanorods. Both Ref. [62] and Ref. [63] gave a penta-tetrahedral twin model with five long $\{100\}$ side facets and five $\{111\}$ end facets (see Fig. 2.11) for their gold nanorods. Ref. [57] described the structure of their long Au nanorods by the twin plane model shown in Fig. 2.12. Their short rods have a different structure from the long ones. Fig. 2.13a shows the HRTEM image of one of the short rods, and the structural model is shown in Fig. 2.13b. In this model the rods have an aspect ratio of 3.0, and their sides consist of four large $\{100\}$ and four large $\{110\}$ facets oriented parallel to the rod axis. Each end has a $\{001\}$ facet and four small $\{111\}$ facets connecting the $\{110\}$ and the $\{001\}$ facets. The long axis of the nanorod lies parallel to the $[100]$ direction of the fcc body.

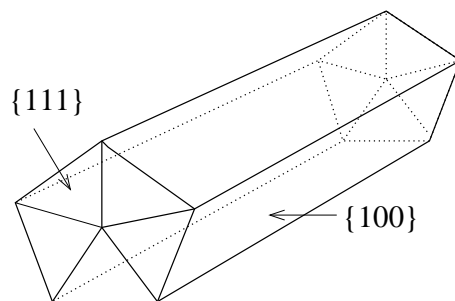


Fig. 2.11: Elongated cyclic penta-tetrahedral twin model of gold nanorods.

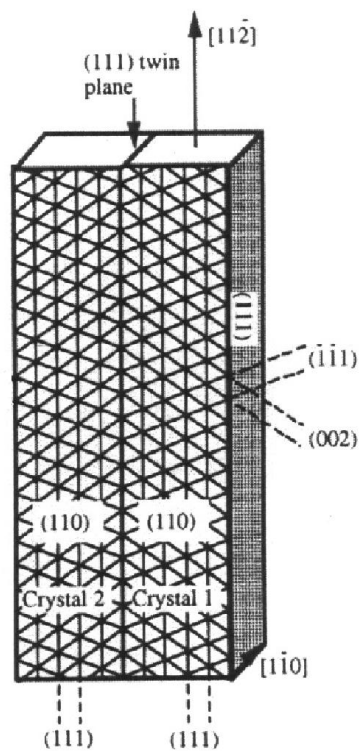


Fig. 2.12: The structure model of the long Au nanorods observed in Ref. [57]. Courtesy of Wang et al. from Ref. [57].

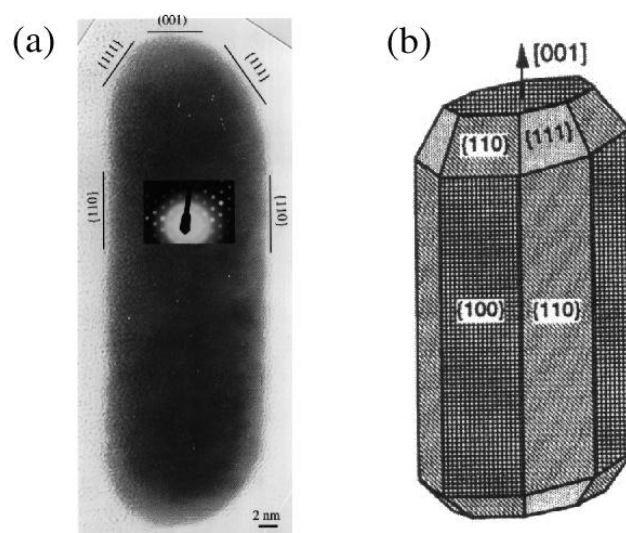


Fig. 2.13: (a) HRTEM image of an Au nanorod. The inset is the electron diffraction pattern recorded from the rod, which proves the single crystalline structure of the rod. (b) A structural model of the Au nanorod shown in (a). Courtesy of Wang et al. from Ref. [57].

Although some groups studied the thermal stability of their rods [28, 61], only the authors of Ref. [57] did serious laser heating experiments to study in depth the thermal stability of their gold nanorods. They found that the melting of the rods takes at least 30–35 ps, independent of the used laser power of 5–20 μJ or the rod aspect ratio of 1.9–3.7 [68]. The femtosecond laser beam melts the nanorods to near spherical particles, while the nanosecond pulses turn them to smaller near spherical fragments [69]. With the exposure of femtosecond laser pulses, the energy needed for complete melting of the rods is about 0.01 J cm^{-2} [70]. They also used HRTEM to study the surface reconstruction of the unstable $\{110\}$ surface and suggested that the $\{110\}$ surface reconstructs into stripes of $\{111\}$ facets due to the absence of rows of atoms along the $[\bar{1}10]$ direction, at defect sites where the capping micelle molecules are missing [71] (see Fig. 2.14). They suggested a scheme for the melting process of the gold nanorods in order to explain the point and planar defects (see Fig. 1.2) formed during laser heating [30]. According to this scheme, shown in Fig. 2.15, the local melting generated by the pulsed laser light nucleates as a point defect in the interior of the nanorod (see Fig. 2.15a). Twins and stacking faults are then formed around these point defects (see Fig. 2.15b). Surface diffusion happens at the same time to encourage the growth of the twinned crystal (see Fig. 2.15c). Because of this growth, the unstable $\{110\}$ facets vanish, and only $\{111\}$ and $\{100\}$ facets exist on the crystal surface (see Fig. 2.15d).

Several other experimental papers have studied interesting features of gold nanorods. Hu *et al.* [72] studied the vibrational response of gold nanorods to ultrafast laser-induced heating both theoretically and experimentally. Jana *et al.* [73] observed the formation of liquid crystalline phases of high aspect ratio (13–18) gold nanorods. Nikoobakht *et al.* [74] studied the self-assembly of gold nanorods using TEM. However, these topics are beyond the scope of this thesis.

Unlike gold nanoclusters, almost no theoretical studies have been focused on the thermal stability and structural changes of gold nanorods. Yu and Duxbury [75] used

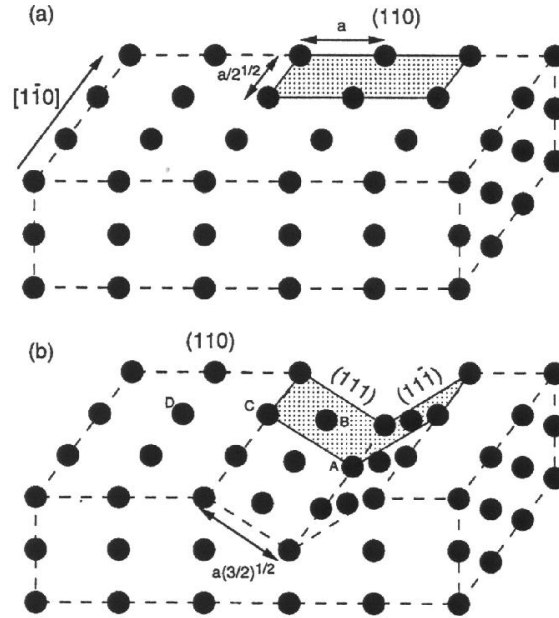


Fig. 2.14: Atomic models of (a) an ideal $\{110\}$ surface and (b) the reconstructed $\{110\}$ surface with missing rows. Courtesy of Wang et al. from Ref. [71].

the glue potential to study the shape change of gold nanorods up to $N = 800$ atoms, which are unstable in their simulated time range of about 200 ps. They drew the conclusion that the small nanorods go through a shape change by a nucleation process, while large clusters change their shapes by surface diffusion. Combe *et al.* [76] studied the shape changing mechanism for general nanomaterials by kinetic Monte Carlo simulations, and concluded that shape change through atomic surface diffusion can only be applied at high temperatures; below the roughening temperature, relaxation is governed by the slower nucleation of a critical germ on a facet.

Thus there is an abundance of experimental results but a lack of theoretical studies of the thermal stability of gold nanorods. To try to fill this gap, the second main topic of the thesis will be to carry out MD simulations for the structural and morphological transitions of gold nanorods in a range of 1000–10 000 atoms. We will report on our results in Chapters 5 and 6. Simulations of rods with sizes comparable to the experimental ones (more than 10^6 atoms) are beyond the limited

computational capability we currently have. For the same reason, simulating long nanorods are very difficult. Thus we studied short gold nanorods (aspect ratio of 3.0) with thousands of atoms, which are stable at room temperature (~ 300 K) in our simulated time of 43 ns. They are with the same surface and internal structure of the short rods reported by Ref. [57] (see Fig. 2.13), and we expect our results to give a better explanation for some of the phenomena observed in the laser heating experiments [28, 29, 30].

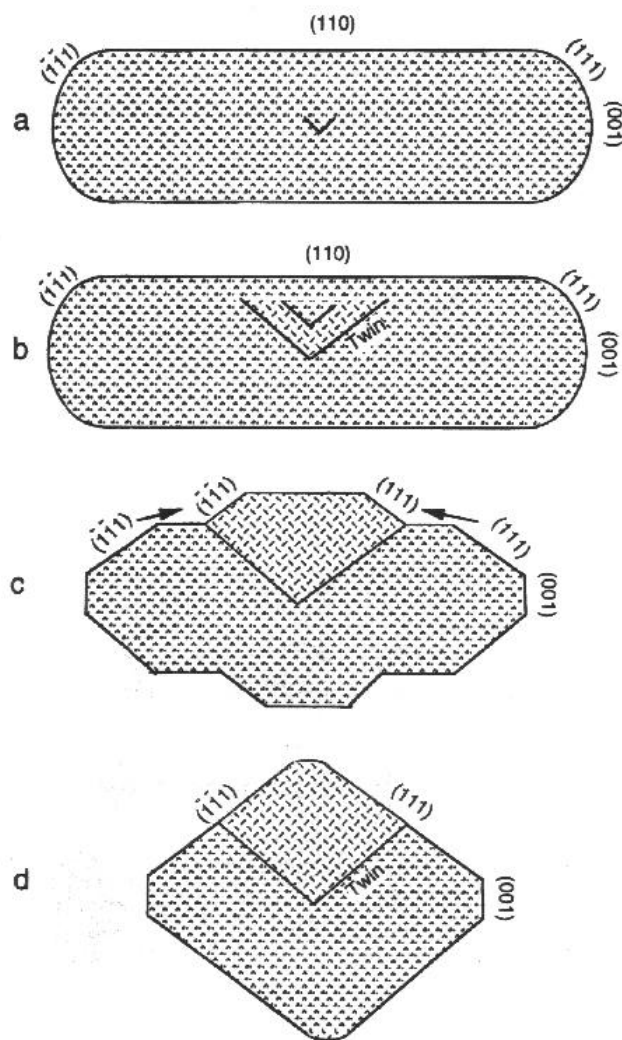


Fig. 2.15: A schematic process suggested in Ref. [30] for the structural transformation from nanorod to nanosphere. Courtesy of Link et al. from Ref. [30].

3. METHODS

In this chapter we will describe the numerical methods and tools we use in our simulations. Some of these methods, such as the empirical potential model for gold, the methods of molecular dynamics, and the bond orientational order parameters, are standard methods in this field. Others of these methods, such as our method for identification of surface particles, the computation of average cluster shape, and the computation of surface curvatures, are newly developed for this work.

3.1 Glue Potential Model

An accurate description of interaction energies can be generated by *ab initio* methods, which solve the Schrödinger equations for electrons and nuclei, without reference to experimental data. On today's computers, *ab initio* methods can be used to simulate systems consisting of up to hundreds of atoms [77]. However, such methods are too computationally demanding to allow long simulation times. Using less accurate but computationally less expensive model potentials, one can extend the size of simulated gold nanoclusters to more than ten thousand atoms. The goal of these model potentials is to replace the complicated interactions of ionic cores and conduction electrons by simpler effective interaction potentials that depend only on the ionic positions.

The Lennard-Jones potential [78] is the widely used empirical potential with a very simple form of $E(r) = C_1/r^{12} - C_2/r^6$, where r is the interatomic distance, and C_1 and C_2 are two constants. Although known to be good for rare gases, it is not suitable for modeling noble metals like gold. The Murrell-Mottram potential

[79] includes a Rydberg two body term and a damped polynomial three body term with parameters fitted by experimental data. This potential model has been used to study semiconductors and metals [80], Au surfaces [81], and gold clusters [46]. The many-body Gupta potential [82] contains a short-range repulsive pair potential and an attractive effective band term representing the n -body cohesive energy of the metallic bonding. It has also been used to study the structure and energetics of gold nanoclusters [21].

Hohenberg and Kohn [83] have shown that the energy is a functional of density, and established a functional density theory (DFT) for interatomic calculations. Within the frame of DFT, the embedded atom method (EAM) [84] fits experimental data to obtain the forms of the energy as a functional of the electron density and the electrostatic pair potential as a function of the distance between atoms. The EAM method has been fitted for various kinds of metals including gold [48].

In this study, we have chosen another potential model, the many-body “glue” potential [38], because it was found to yield an accurate description of the bulk, defect and surface properties of gold [38]. Many simulations have been done using the “glue” model for slab-like bulk gold surfaces as well as for gold nanoclusters. Most of these works are in good agreement with experiments (refer to Chapter 2 for the overview). Thus our choice of the “glue” model allows us to compare our results directly with many existing simulations as well as experiments.

In the “glue” model, the potential energy of a system of N atoms consists of a sum of pair potentials ϕ and a many-body “glue” energy U ,

$$V = \frac{1}{2} \sum_i \sum_{j \neq i} \phi(r_{ij}) + \sum_i U(n_i). \quad (3.1)$$

Here the sums run over all particles, $r_{ij} = |\mathbf{r}_i - \mathbf{r}_j|$ is the interatomic distance between atoms i and j , and $\phi(r)$ is the pair interaction energy. The many-body “glue” energy $U(n_i)$ depends on an effective coordination number n_i of atom i , which is defined by

$$n_i = \sum_j \rho(r_{ij}). \quad (3.2)$$

Here $\rho(r)$ is a short-ranged monotonically decreasing function of the interatomic distance r . We use the specific forms for the pair potential $\phi(r)$, and the glue terms $U(n)$ and $\rho(r)$, as given by Ercolessi *et al.* in Ref. [38]. The plots of these three functions are shown in Fig. 3.1.

We will simulate our gold nanomaterials by treating each atom as a classical particle. This classical approximation can be justified as follows. The glue potential is an empirical classical potential model designed to reproduce the movements of nuclei in the electron sea. Quantum mechanical effects associated with the *electron gas* are therefore included implicitly. As for quantum effects associated with the motion of the gold nuclei, these are negligible at the temperatures we are interested in. The thermal deBroglie wavelength for a gold atom at 500 K is about 0.08 Å, which is small compared to the size of a gold atom and much smaller than the average interatomic spacing ~ 3 Å.

3.2 Molecular Dynamics Methods

We integrate the classical Newton's equations of motion using the velocity Verlet algorithm [85]. At each time step, the position $\mathbf{r}_i(t)$ of atom i is updated according to the total force on the atom, $\mathbf{F}_i(t)$, and the velocity, $\mathbf{v}_i(t)$, from the previous step,

$$\mathbf{r}_i(t + \Delta t) = \mathbf{r}_i(t) + \mathbf{v}_i(t)\Delta t + \frac{\mathbf{F}_i(t)}{2m}\Delta t^2, \quad (3.3)$$

where t is the simulation clock time, Δt is the time interval between successive steps, and m is the mass of one atom. After all the atomic positions are updated, the forces are then updated according to the glue Hamiltonian of Eq. (3.1). Finally the velocities are updated according to,

$$\mathbf{v}_i(t + \Delta t) = \mathbf{v}_i(t) + \frac{\mathbf{F}_i(t + \Delta t) + \mathbf{F}_i(t)}{2m}\Delta t. \quad (3.4)$$

A relatively large time interval of $\Delta t = 4.3$ fs has been chosen for our simulations in order to save computational time. However, we find that this Δt is still small enough

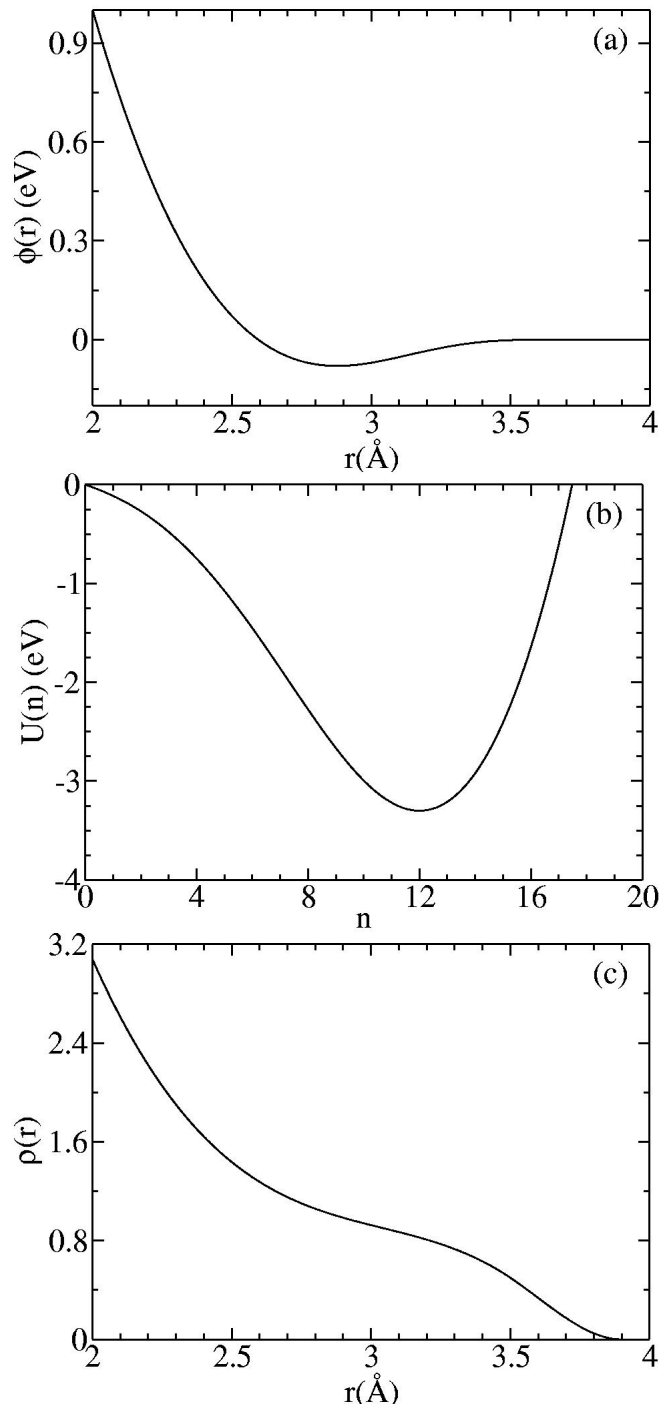


Fig. 3.1: Three functions $\phi(r)$, $U(n)$, and $\rho(r)$ of the glue potential model optimized for gold.

to keep the numerical error in the energy, caused by the finite time step, to be of order 10^{-5} eV per atom.

Because the many-body “glue” potential uses a cutoff, a cell index method [86] can be used to reduce the computational time. In this method, the simulation box is divided into cubic cells with side lengths larger than the cutoff distance (3.9 Å for the gold glue model). When calculating energies and forces one considers only interactions between atoms within the same cell and the neighboring 26 cells. This approach reduces the required computation time from order N^2 to order N . On a PC equipped with a 1.5 GHz AMD Athlon CPU and 1 GB of memory, 25 000 steps can be carried out per CPU-hour for a system of 2624 atoms propagating the system for about 100 ps.

The basic molecular dynamics (MD) step described above conserves the total energy, thus it intrinsically samples in a microcanonical ensemble. To sample instead in the canonical ensemble, we supplement this basic MD step according to two different well known methods. The Andersen thermostat [85] is a MD method that mimics a system coupled to a heat bath with constant temperature. At the end of each MD step a particle is chosen randomly and assigned with a new velocity sampled from the Boltzmann distribution of a given temperature. The Andersen thermostat samples both configuration and momentum spaces correctly, so that the instantaneous total kinetic energy fluctuates, as is the case for a real physical system. However, the Andersen thermostat method does not conserve linear and angular momenta, and so will cause the system’s position and orientation to drift over the course of the simulation. This would complicate our analysis of cluster shape as well as atomic diffusion, since we want to measure these quantities with respect to coordinates that stay fixed with respect to the cluster.

We therefore will also use a second approach [11, 23] which is to keep the total kinetic energy of the system rigidly fixed at a constant temperature. We do this by rescaling all velocities $\mathbf{v}_i(t + \Delta t)$ at the end of each MD step by a constant factor,

so that the average kinetic energy stays fixed at $\frac{1}{2}m\langle\mathbf{v}_i^2\rangle = \frac{3}{2}k_B T$. This scheme is unphysical in the sense that the instantaneous kinetic energy does not fluctuate. Nevertheless, it correctly samples configuration space, and so gives correct equilibrium averages as long as our study does not measure quantities in momentum space. We call this method constant temperature MD. This method has the advantage of conserving both linear and angular momenta, thus keeping the cluster at a fixed position and orientation.

In our simulations of the gold nanocluster in Chapter 4, our first goal will be to cool our cluster to low temperature from a liquid melt to see what solid structure forms. To do this we use the Andersen thermostat method since we believe it models more closely the true dynamics of the physical system, and hence will incorporate effects that may be due to kinetics rather than just pure thermodynamics. Later, to observe the equilibrium shape and other properties of the cluster, we will use the constant temperature MD to heat back through melting. This will keep the cluster position and orientation fixed, and so simplify our analysis. Since all our measured quantities depend on positional coordinates only, this constant temperature MD is sufficient to give accurate results.

A continuous heating MD approach can also be used to simulate the laser heating of samples, which almost uniformly transfers heat to each atom. Instead of rescaling the temperature to a constant as in the constant temperature MD described above, in the continuous heating MD, the kinetic energy of each atom is rescaled to increase by a fixed amount of energy at each time step. In this way the system total energy is increased linearly, as the laser heating does to the real system. In Chapter 5 we will use the continuous heating MD to simulate the behavior of gold nanorods by laser heating.

The continuous heating MD simulates a kinetic rather than an equilibrium procedure. For moderate heating rates, the system will not in general be fully relaxed to equilibrium during the simulation. Temperature varies continuously and measured

properties may depend on the heating rate. The effective quantities are measured as instantaneous functions of time rather than as ensemble averages at a fixed temperature. In Chapter 6 we therefore reinvestigate the heating of gold nanorods, but this time using a “quasi-equilibrium heating” procedure similar to that used earlier for our clusters. With this approach we can average over many configurations at the same temperature to compute average thermal properties. We believe that this quasi equilibrium approach is dynamically equivalent to continuous heating but at a much slower rate.

3.3 Quantifying Structure by Bond Orientational Order Parameters

Throughout this thesis, we will define the neighboring atoms of a given atom i as those atoms which have an interatomic distance less than a cutoff radius of 3.8 Å. The value of this cutoff has been taken to be equal to the distance to the minimum between the first and the second peaks of the pair correlation function, which is the probability distribution $g(r)$ of finding another particle to sit at a distance r from the given particle. In Fig. 3.2 we show our computation of the pair correlation functions of a gold nanocluster with $N = 2624$ atoms at $T = 100$ K with the Ih structure, and at $T = 1500$ K in the liquid state.

To determine the crystalline structure of our gold nanomaterials, we will use the method of bond orientational order parameters [87], which we now review. A bond is defined as the vector joining a pair of neighboring atoms. The idea of the bond order parameters is to capture the symmetry of bond orientations regardless of the bond lengths. The local order parameters associated with a bond \mathbf{r} are the set of numbers,

$$Q_{lm}(\mathbf{r}) \equiv Y_{lm}(\theta(\mathbf{r}), \phi(\mathbf{r})), \quad (3.5)$$

where $\theta(\mathbf{r})$ and $\phi(\mathbf{r})$ are the polar and azimuthal angles of the bond with respect

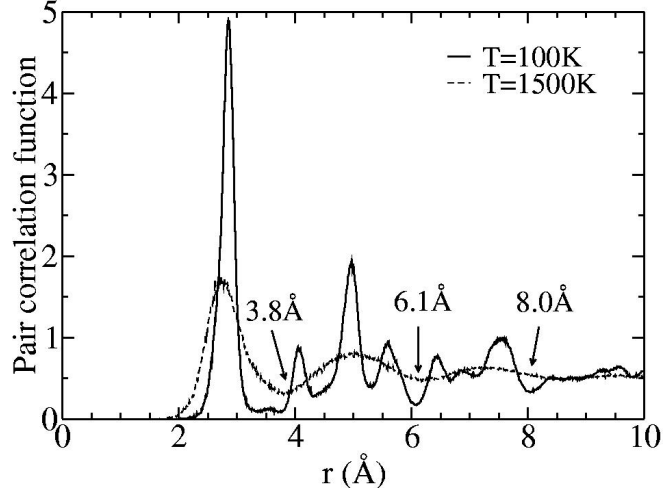


Fig. 3.2: Pair correlation functions of the gold nanoclusters with $N = 2624$ atoms at $T = 100$ K with the Ih structure, and at $T = 1500$ K in the liquid state.

to an arbitrary but fixed reference frame, and $Y_{lm}(\theta(\mathbf{r}), \phi(\mathbf{r}))$ are the usual spherical harmonics. Since the bond between atoms i and j may be arbitrarily taken as either \mathbf{r}_{ij} or $\mathbf{r}_{ji} = -\mathbf{r}_{ij}$, it is useful to consider only the even- l bond parameters Q_{lm} , since only these are invariant to such bond inversions. Global bond order parameters can then be calculated by averaging $Q_{lm}(\mathbf{r})$ over all bonds in the system,

$$\overline{Q}_{lm} \equiv \frac{1}{N_b} \sum_{\text{bonds}} Q_{lm}(\mathbf{r}), \quad (3.6)$$

where N_b is the number of bonds. To make the order parameters invariant with respect to rotations of the reference frame, the second-order invariants are defined as,

$$Q_l \equiv \sqrt{\frac{4\pi}{2l+1} \sum_{m=-l}^l |\overline{Q}_{lm}|^2}, \quad (3.7)$$

and the third-order invariants are defined as,

$$W_l \equiv \sum_{\substack{m_1, m_2, m_3 \\ m_1 + m_2 + m_3 = 0}} \begin{pmatrix} l & l & l \\ m_1 & m_2 & m_3 \end{pmatrix} \overline{Q}_{lm_1} \overline{Q}_{lm_2} \overline{Q}_{lm_3}, \quad (3.8)$$

where the coefficients (\dots) are the Wigner $3j$ symbols [88]. It is standard to define a normalized quantity,

$$\hat{W}_l \equiv \frac{W_l}{(\sum_m |Q_{lm}|^2)^{3/2}} \quad (3.9)$$

which, for a given l , is independent of the magnitudes of the $\{Q_{lm}\}$.

The four bond order parameters $Q_4, Q_6, \hat{W}_4, \hat{W}_6$ are generally sufficient to identify different crystal structures. In Table 3.1 we give their values for ideal periodic fcc, hcp, sc (simple cubic), and bcc (body-centered-cubic) crystal structures. In Chapter 4 we will be interested particularly in the Mackay icosahedral (Ih) structure. Since the Ih structure is not periodic, it may in principle have values for the bond order parameters that depend on the cluster size. In Fig. 3.3a we plot the values of the four bond orientational order parameters vs. the cluster size N for several ideal Ih structures. Although there is a strong size dependence for small clusters, the bond parameters saturate to well defined values as N increases, and we list these in Table 3.1. Note that although, for large N , most of the atoms in the Ih structure have a local fcc structure, the values of the bond order parameters are different from those of a pure fcc crystal; this is due to averaging the order parameters over the differing orientations of the 20 fcc tetrahedra that make up the Ih structure.

The bond orientational order parameters, averaged over all bonds, will be used to monitor global structural changes of our systems. In particular, a large liquid cluster will have vanishing values for the bond order parameters. Thus the decay of the bond parameters from their finite low temperature values to zero will be a signature of the melting transition. In our works we will pay much attention to the behavior of atoms on the surface of the nanomaterials. Surface structures of

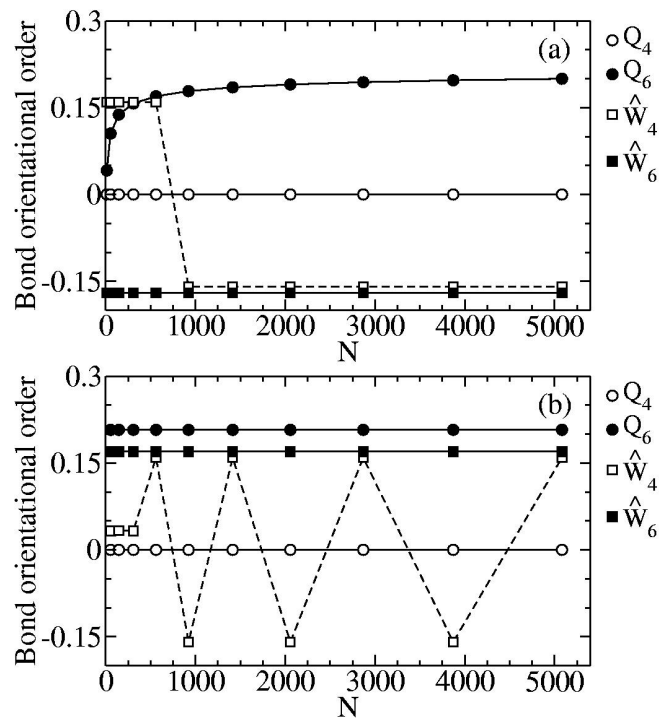


Fig. 3.3: The values of (a) the bulk and (b) the surface bond orientational order parameters vs. the cluster size N of several Ih structures. Only magic numbers N that give ideal Ih structures are used.

Tab. 3.1: Bond order parameters for 3D face-centered-cubic (fcc), hexagonal-close-packed (hcp), simple-cubic (sc), body-centered-cubic (bcc), liquid, and Mackay icosahedral (Ih) bulk structures, as well as 2D Ih surface, gold {110} surface, gold {100} surface, and gold {111} surface structures.

Geometry	Q_4	Q_6	\hat{W}_4	\hat{W}_6
fcc	0.190 94	0.574 52	-0.159 32	-0.013 16
hcp	0.097 22	0.484 76	0.134 10	-0.012 44
sc	0.763 76	0.353 55	0.159 32	0.013 16
bcc	0.082 02	0.500 83	0.159 32	0.013 16
liquid	0	0	0	0
Ih bulk	0	0.199 61	0.159 32	-0.169 75
Ih surface	0	0.207 29	$\pm 0.159 32$	0.169 75
{110} surface	1	1	0.134 10	-0.093 06
{100} surface	0.829 16	0.586 30	0.124 97	-0.007 21
{111} surface	0.375 00	0.740 83	0.134 10	-0.046 26

nanomaterials can often be quite different from the bulk. We therefore will consider separately the *bulk* bond order parameters, computed by averaging over only those bonds connecting atoms that are in the internal “bulk” of the cluster, vs. the *surface* bond order parameters, computed by averaging over only those bonds connecting pairs of atoms that lie on the surface of the cluster. In Fig. 3.3b we plot the values of such surface bond order parameters for an ideal Ih structure vs. cluster size N . Again we see that they approach well defined constants as N increases, except for \hat{W}_4 which oscillates. The values of these large N surface bond parameters are also listed in Table 3.1. Note that for the same Ih structure, the bulk bond parameters have different values than the surface bond parameters, since they are measuring properties of three dimensional vs. two dimensional structures, respectively.

The above computations of the 2D surface bond order parameters actually measure the 2D closed shell structure. It is also useful to calculate the bond order parameters for flat planes to identify the 2D surface structure of individual facets. In Table 3.1 we also list the bond order parameters for the three low-index surfaces shown in Fig. 2.2.

3.4 Radius of Gyration to Monitor the Shape Change

As gold nanorods are heated, one often observes a change in their aspect ratio. A convenient way to monitor the shape change of gold nanorods is by measuring the *radius of gyration*,

$$r_g = \sqrt{\frac{1}{N} \sum_i [\mathbf{r}_i(t) - \mathbf{r}_c]^2}, \quad (3.10)$$

where the sum runs over all particles and \mathbf{r}_c is the center of mass of the rod. The radius of gyration is large for rods with large aspect ratio and reaches its minimum value for a spherical shape.

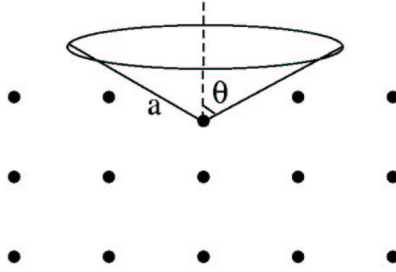


Fig. 3.4: Schematic of the cone algorithm.

3.5 Geometrical Analysis of the Surface

In this section we describe the algorithms that we use for quantifying the geometrical behavior of the gold nanomaterials.

3.5.1 Cone Algorithm

The first step in our analysis is to identify the surface particles of the nanomaterials accurately according to their geometrical positions. We have developed a new algorithm, which we call the “cone” algorithm, to do this. For a given particle, we define an associated *cone region* as the region inside a cone of side length a and angle θ , whose vertex resides on the particle. A *hollow cone* is a cone region with no other particles inside it. We take a particle to be on the surface if at least one associated hollow cone can be found.

The cone algorithm is intrinsically consistent with the general definition of surface particles. It can pick up all of the particles on a convex surface. For the particles on a concave surface, the precision of identifying a surface atom relies on the choice of the parameters a and θ (see Fig. 3.4). By visual examination of our generated configurations, we found that the two parameters $a = 5.0 \text{ \AA}$ and $\theta = \pi/3$ gave good results for our gold nanomaterials.

The cell index method mentioned above, and other numerical optimization ap-

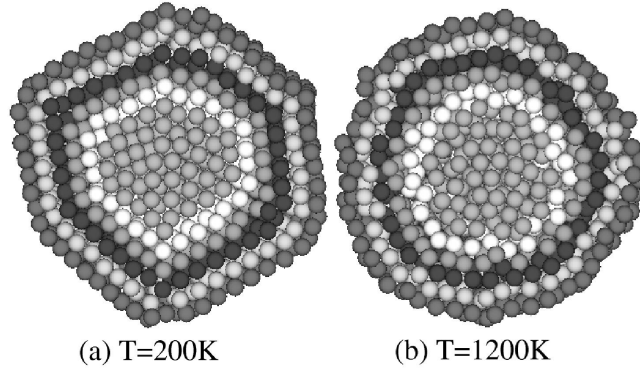


Fig. 3.5: Cross sections of a gold cluster with 2624 atoms at (a) $T = 200$ K in an Ih structure and (b) $T = 1200$ K in the liquid, with the 5 topmost layers, as determined by the cone algorithm, marked by different gray scales.

proaches, have improved the computational speed of the implementation of this algorithm. For a gold cluster with 5082 atoms, we need only one and a half seconds CPU to determine the surface atoms. The cone algorithm can also be applied recursively to divide particles into surface and sub-surface layers to allow inter-layer analysis. Fig. 3.5 shows a planar slice cut through an instantaneous configuration of a gold cluster with 2624 atoms at a) $T = 200$ K in an Ih structure and b) $T = 1200$ K in the liquid, respectively. From this figure we can see that the cone algorithm works well on both solid and liquid configurations.

3.5.2 Curvature

Having identified the surface particles, we next want to quantify the surface morphology of the clusters. To do this, we compute two different measures of the surface curvature, the *bond curvature* and the *maximal local surface curvature*, as defined below.

Our first step is to determine a tangent plane to the cluster surface at each surface particle. To do this, we consider the collection of particles determined by the particle of interest and all its neighboring particles which are also on the surface. Denote the

coordinates of these particles by $\mathbf{r}_i \equiv (x_i, y_i, z_i)$, $i = 1 \dots N_s$, where N_s is the number of the particles under consideration. We define the tangent plane to pass through the center of mass of these particles, and we determine its orientation by minimizing the mean square distance of the particles to the plane. Specifically, we solve for this plane as follows. If $\hat{\mathbf{n}} \equiv (n_x, n_y, n_z)$ is the unit normal vector of the tangent plane and $\mathbf{r}_c \equiv (x_c, y_c, z_c)$ is the coordinate of the center of mass, then the distance from the i th particle to the tangent plane is,

$$d_i = \hat{\mathbf{n}} \cdot (\mathbf{r}_i - \mathbf{r}_c). \quad (3.11)$$

We determine the normal vector $\hat{\mathbf{n}}$ by minimizing $\sum_i d_i^2$ subject to the constraint $\hat{\mathbf{n}}^2 = 1$. Introducing an undetermined Lagrange multiplier λ , we solve for,

$$\frac{\delta}{\delta \mathbf{n}} \left[\sum_i d_i^2 - \lambda (\hat{\mathbf{n}}^2 - 1) \right] = 0. \quad (3.12)$$

Eq. (3.12) leads to the symmetric eigenvalue problem,

$$\begin{pmatrix} XX - \lambda & XY & XZ \\ XY & YY - \lambda & YZ \\ XZ & YZ & ZZ - \lambda \end{pmatrix} \begin{pmatrix} n_x \\ n_y \\ n_z \end{pmatrix} = 0, \quad (3.13)$$

where $XY = \sum_i (x_i - x_c)(y_i - y_c)$, and other quantities are computed similarly. The smallest of the three possible eigenvalues λ determines the minimum value of $\sum_i d_i^2$, and its associated eigenvector (n_x, n_y, n_z) is the normal vector $\hat{\mathbf{n}}$ of the tangent plane.

We now define the *bond curvature*, c_b , of a bond connecting two neighboring surface particles. Consider two neighboring surface particles at positions \mathbf{r}_1 and \mathbf{r}_2 and let $\hat{\mathbf{n}}_1$ and $\hat{\mathbf{n}}_2$ be the unit normal vectors of their corresponding tangent planes. We can uniquely fit a circle that passes through the two points, such that $\hat{\mathbf{n}}_1$ and $\hat{\mathbf{n}}_2$ are normal to the circle. The bond curvature c_b is then defined in terms of the radius R of this fitted circle,

$$c_b \equiv \frac{1}{R} = \frac{2\sin(\theta/2)}{r_{ij}}, \quad (3.14)$$

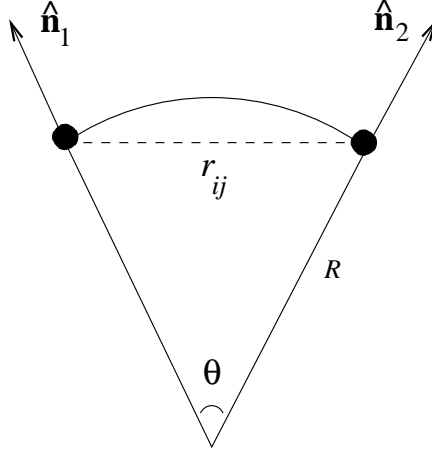


Fig. 3.6: Schematic for the calculation of the bond curvature.

where $\theta = \text{acos}(\hat{\mathbf{n}}_1 \cdot \hat{\mathbf{n}}_2)$ is the angle between the two normal vectors and $r_{ij} = |\mathbf{r}_1 - \mathbf{r}_2|$ is the distance between the two particles. The geometry of this fit is illustrated in Fig. 3.6.

Alternatively, we can compute the *surface curvature* at each particle on the surface as follows. Consider a particle on the surface, and all its neighboring particles that are also on the surface. Since the geometry of these points roughly defines a surface in 3D space, we find the best fit of a paraboloid surface to these points. The *maximal local curvature*, κ_M , and the *minimal local curvature*, κ_m , are then given by the two principle curvatures of the fitted paraboloid. The schematic of this method is shown in Fig. 3.7. To fit the paraboloid at the surface particle \mathbf{r}_0 , we take the normal vector $\hat{\mathbf{n}}$ to the tangent surface at \mathbf{r}_0 , as computed above, and define this to be the local z -axis. We place the origin at \mathbf{r}_0 and then choose arbitrary but fixed x and y axes in the tangent plane. We then define the coordinates (x_i, y_i, z_i) of neighboring particle \mathbf{r}_i in this coordinate system. Next we choose a paraboloid function,

$$f(x, y) = a_{xx}x^2 + 2a_{xy}xy + a_{yy}y^2, \quad (3.15)$$

and fit it through the neighboring points \mathbf{r}_i by minimizing

$$S = \sum_i (z_i - f(x_i, y_i))^2, \quad (3.16)$$

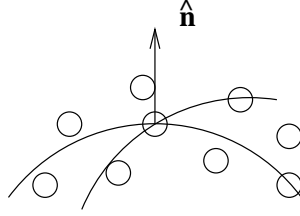


Fig. 3.7: Schematic for the calculation of the local surface curvatures.

with respect to a_{xx} , a_{xy} , and a_{yy} . This leads to the following set of linear equations,

$$\begin{pmatrix} \sum_i x_i^4 & \sum_i x_i^3 y_i & \sum_i x_i^2 y_i^2 \\ \sum_i x_i^3 y_i & \sum_i x_i^2 y_i^2 & \sum_i x_i y_i^3 \\ \sum_i x_i^2 y_i^2 & \sum_i x_i y_i^3 & \sum_i y_i^4 \end{pmatrix} \begin{pmatrix} a_{xx} \\ 2a_{xy} \\ a_{yy} \end{pmatrix} = \begin{pmatrix} \sum_i x_i^2 z_i \\ \sum_i x_i y_i z_i \\ \sum_i y_i^2 z_i \end{pmatrix}. \quad (3.17)$$

Solving Eq. (3.17) for a_{xx} , a_{xy} , a_{yy} , we diagonalize the symmetric matrix with the elements $a_{\mu\nu}$ to obtain the two principle axes and the corresponding eigenvalues λ_1 and λ_2 . The local curvatures are then given by $\kappa_{1,2} = \frac{1}{2}\lambda_{1,2}$. We will see that the maximal local curvature will be very helpful for visualizing the vertex, edge and facet atoms of the cluster surface.

To test our above methods, we consider the ideal Ih gold cluster with a magic number of atoms $N = 2869$, shown earlier in Fig. 2.4. In Fig. 3.8 (top row) we show the resulting histograms of bond curvature and maximal local curvature for this cluster. Both histograms consist solely of δ functions, corresponding to the facets, the edges and the vertices of the Ih structure. For the bond curvature histogram there are *two* separate peaks for the vertices, corresponding to the bond curvatures between the vertex atoms and the edge atoms, and the vertex atoms and the facet atoms. We also test our method for the average shape of a liquid gold cluster with 2624 atoms at $T = 1200$ K (shown in Fig. 3.9c), which is a nearly perfect sphere. We show our results in Fig. 3.8 (bottom row). Both histograms have just one peak of finite width, centered at $1/R = 0.047 \text{ \AA}^{-1}$, with $R = 21.5 \text{ \AA}$ the radius of the spherical liquid drop. Note that while the average shape of the liquid drop is close to a perfect sphere, the histogram of its curvatures seems relatively broad. We have

found that this is due to the small discrete number of neighboring surface particles that is used to define the fitted paraboloid. Even small deviations of these particles from a constant radius can lead to noticeable variations in the fitted curvatures. We find that we can reduce the width of the curvature histogram for the liquid cluster by increasing the cutoff length used to define neighboring particles, and so have more particles included in the fits to the local paraboloids. However, while this improves the calculation for a spherical cluster, it makes it worse for high curvature regions near edges and vertices in an Ih cluster, where curvature varies rapidly as one moves across the surface. With this understanding of our method's limitations, we therefore leave our cutoff as given above.

3.5.3 Average Shape

At low temperatures, the atoms in the gold cluster remain at well defined equilibrium positions and only thermally oscillate around the vicinity of these equilibrium positions. The shape of the cluster is thus easily determined from an instantaneous configuration. At high temperatures, however, atoms become more mobile and the macroscopic shape of the cluster fluctuates dramatically from configuration to configuration. In this case it becomes necessary to average over many fluctuating configurations to define the average cluster shape. Since our constant temperature MD conserves both linear and angular momenta, the configurational shape changes we average over represent fluctuations of the surface atoms rather than trivial shifts or rotations of the cluster as a whole.

At high temperatures, simply averaging the position of each atom throughout the course of the simulation does not give the average shape because the atoms are in general no longer bound to specific sites but may diffuse many interatomic spacings through the cluster. We therefore use the following approach to define the average cluster shape. We divide the surface of the cluster into equal solid angles, and then average the instantaneous surface atom positions in each solid angle. This average

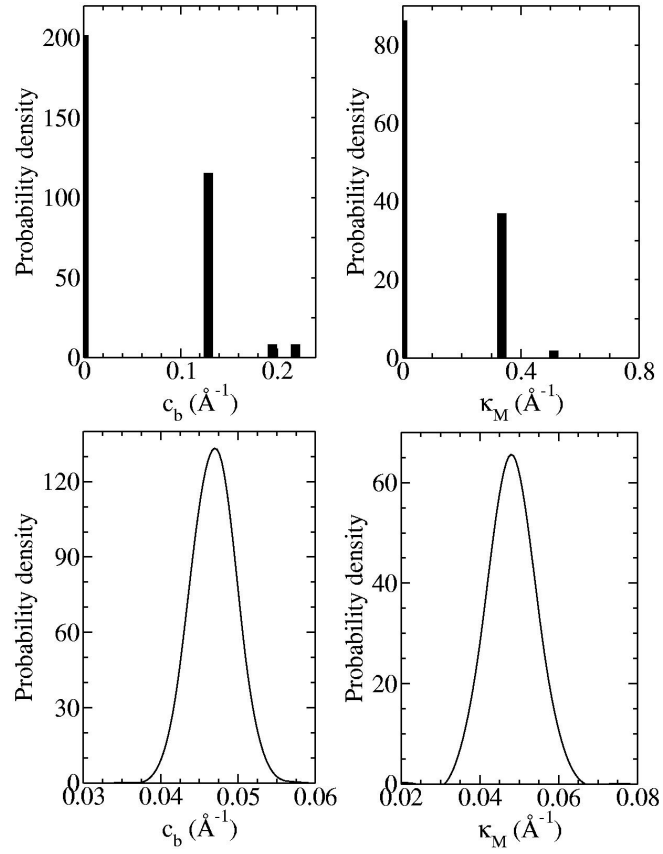


Fig. 3.8: Histograms of bond curvature c_b and maximal local curvature κ_M of (i) top row: an ideal Ih cluster with $N = 2869$ atoms, and (ii) bottom row: the average shape of a liquid cluster with $N = 2624$ atoms.

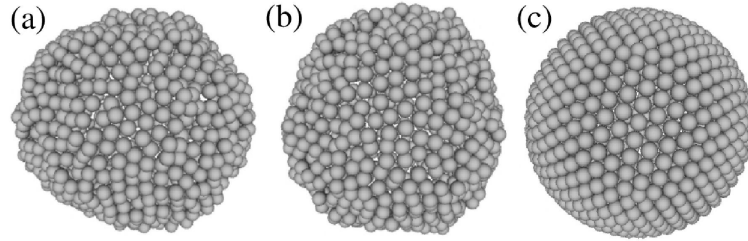


Fig. 3.9: A liquid gold cluster with 2624 atoms at $T = 1200$ K. (a) and (b) are two instantaneous configurations. (c) is the shape averaged over 1000 such instantaneous configurations.

position in each solid angle then defines the profile of the cluster's average shape. This average shape does not contain information about the individual surface atom positions, since generally a given solid angle may contain the instantaneous positions of different surface atoms at different times. To define our solid angle division, we use the best covering spherical codes with icosahedral symmetry [89] to divide the 4π total solid angle of the sphere centered at the center of mass into cone cells with almost equal solid angles. Choosing different numbers of solid angles results in different resolutions; we always choose a number of solid angles that matches as close as possible to the number of surface atoms in the cluster.

We illustrate this method for a liquid gold cluster with 2624 atoms at $T = 1200$ K. In Figs. 3.9a and b we show two arbitrary instantaneous configurations of the cluster. Theoretically, a liquid cluster should have a perfect sphere as the equilibrium shape. However, we see that the instantaneous configurations can have noticeably large fluctuations about the average shape. Applying our shape averaging procedure above on 1000 configurations sampled at equal time intervals from 43 ns of simulated time, we recover that the average shape, shown in Fig. 3.9c, is a perfect sphere as expected. Note that in Figs. 3.9a and b, the small spheres represent instantaneous atomic positions. In contrast, in Fig. 3.9c, they represent not specific atoms, but rather the average surface position within the given solid angle.

Although this shape averaging method works well with spherical-like clusters, it is unsuitable for rod-shape crystals, because the 4π solid angle division would give a nonuniform mesh. In Section 6.3, for gold nanorods, we will introduce a simpler method to compute only the cross-sectional average shape to monitor the side surface evolution of the rods.

3.6 Atom Diffusion Analysis

With enough kinetic energy, atoms can hop around their crystal sites and even travel across the whole cluster. The mean squared displacement (MSD) [85], $\Delta r^2(t)$, is a convenient way to measure the average movement of a group of atoms. It is defined as

$$\Delta r^2(t) = \frac{1}{MN_s} \sum_{j=1}^M \sum_{i=1}^{N_s} [\mathbf{r}_i(t_j + t) - \mathbf{r}_i(t_j)]^2, \quad (3.18)$$

where \mathbf{r}_i , $i = 1 \dots N_s$ are the positions of the N_s atoms under consideration, and t is the time interval over which the motion takes place. We average over M non-overlapping time intervals, with $t_j \equiv t_{j-1} + t$. For an infinite three dimensional bulk system, we expect that $\Delta r^2 = 6Dt$ as $t \rightarrow \infty$, where D is the diffusion coefficient. In a finite cluster, however, the MSD will eventually saturate on a length scale comparable to the cluster size. We therefore determine the diffusion coefficient D by fitting $\Delta r^2(t)$ to the early time linear part before saturation takes place.

We will also find that a convenient way to visualize individual atomic displacements is through an *ellipsoid of displacement*. We compute this ellipsoid as follows. For a given atom traced through K successive configurations for a simulated time t , the mean squared displacement correlations are given by the 3×3 matrix \mathbf{C} with elements,

$$C_{\mu\nu} \equiv \frac{1}{K} \sum_{i=1}^K (r_{i\mu} - \langle r_\mu \rangle)(r_{i\nu} - \langle r_\nu \rangle), \quad (3.19)$$

where $\mu, \nu = x, y, z$, $r_{i\mu}$ is the μ -coordinate of the atom in configuration i , and $\langle r_\mu \rangle$ is the average of the coordinate over all K configurations. The probability for the atom

to be at position \mathbf{r} is then approximated as $P(\mathbf{r}) \sim \exp(-\frac{1}{2}[(\mathbf{r} - \langle \mathbf{r} \rangle) \cdot \mathbf{C}^{-1} \cdot (\mathbf{r} - \langle \mathbf{r} \rangle)])$, and so the surface of our ellipsoid of displacement is given by the equation,

$$(\mathbf{r} - \langle \mathbf{r} \rangle) \cdot \mathbf{C}^{-1} \cdot (\mathbf{r} - \langle \mathbf{r} \rangle) = 1. \quad (3.20)$$

The eigenvectors of $C_{\mu\nu}$ and the square root of their corresponding eigenvalues then define the axes and principal radii of the ellipsoid, which we center on the average atom position $\langle \mathbf{r} \rangle$. This ellipsoid provides a convenient visualization of the directional distribution of root mean squared displacements over the time t .

4. MELTING OF MACKAY ICOSAHEDRAL GOLD NANOCLUSTERS

In this chapter we report on our results for the melting of gold nanoclusters. As we have explained in Section 2.3, small gold nanoclusters with hundreds of atoms can undergo transitions between several different crystalline structures even at low temperatures [22, 51, 52], and have been studied in several previous theoretical works. On the other hand, large gold clusters with more than 5000 atoms require too much computational time to allow for the long simulated times we want in order to explore the equilibrium behavior. Thus in this work, we have simulated several clusters in the range of 600 to 5000 atoms. In our results below, we will concentrate on the moderate size of $N = 2624$ atoms, for which we have done our most complete and careful analysis. We will also give less detailed results for two smaller sizes, $N = 603$ and $N = 1409$, in order to illustrate general trends. Note that these values of N are *not* among the magic numbers (see Eq. 2.1) needed to construct a perfect Mackay icosahedron (Ih). Nevertheless we will show that these clusters still form Ih structures upon cooling. We have also studied several clusters *with* a magic number of atoms, by explicitly constructing the Mackay icosahedron at low temperature, and heating through melting. We will give results for sizes $N = 922$ and $N = 5082$ in order to compare with the other more generic values of N . Note that these values are actually one atom smaller than the magic number N given by Eq. (2.1). This is because we construct these clusters with a missing central atom, in order to be consistent with

the clusters we found from cooling, as will be described in Section 4.1. In order to observe the equilibrium properties of gold nanoclusters, our simulated time is of the order of tens of nanoseconds, which is about tens or hundreds of times longer than the previous simulation works we have reviewed in Section 2.3.

4.1 Mackay Icosahedra with a Missing Central Atom

Our first goal is to cool a liquid cluster through the melting transition to determine what is the thermodynamically preferred crystalline structure into which it solidifies. We therefore started with a liquid gold cluster with $N = 2624$ atoms which we roughly equilibrated at 1500 K, before cooling to 1200 K where we equilibrated longer. We then cooled the cluster down to 200 K, with temperature intervals of 100 K. At each temperature the system is equilibrated for 5×10^6 steps (21.5 ns) using the Andersen thermostat method. With this cooling method we find that our cluster solidifies into an Ih structure [14].

In Fig. 4.1 we show an instantaneous configuration of this $N = 2624$ gold cluster at $T = 200$ K, which is our lowest temperature. To find out what structure this cluster has, we have calculated the local curvatures for each surface atom according to the method of Section 3.5.2. In Fig. 4.1a we shade each atom according to the maximal local curvature; the greater the curvature, the darker the gray scale. Comparison with Fig. 2.4 strongly suggests that our cluster has an Ih structure. Large curvature regions correspond to edges and vertices, while low curvature regions are the flat $\{111\}$ facets of the fcc tetrahedra. Note that some vertices have low curvature; this is because these vertices have their top most atom missing, and so form a small local flat region.

To further illustrate that our cluster has an Ih structure, we have computed the local bond order parameters for each atom, averaging over all bonds that connect the

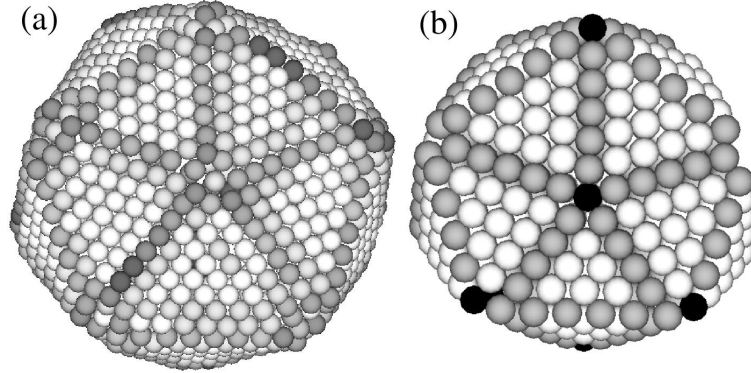


Fig. 4.1: *Ih* structure of an $N = 2624$ atom gold cluster at $T = 200$ K. (a) Surface of an instantaneous configuration with atoms shaded according to the maximal local curvature; the larger the curvature, the darker the gray scale. (b) The same configuration with the three outermost layers peeled away. Atoms are shaded according to their local crystal structure: fcc is white, hcp is gray, and “other” is black.

given atom to its neighbors. Using the values in Table 3.1, we then identify each atom with its local crystal structure. We regard atoms with $Q_4 > 0.17$ and $\hat{W}_4 < -0.10$ as having a local fcc structure, and atoms with $Q_4 < 0.13$ and $\hat{W}_4 > 0.07$ as having a local hcp structure; all other atoms are simply labeled as “other”. Because the surface layer and the two sub layers closest to the surface exhibit surface reconstruction and have frozen in surface fluctuations, we have peeled them away by use of the cone algorithm of Section 3.5.1. The resulting interior of the cluster is shown in Fig. 4.1b, where fcc atoms are shaded white, hcp atoms gray, and “other” atoms black. The *Ih* structure of the cluster is readily apparent. One clearly sees the flat $\{111\}$ facets of the fcc tetrahedra, the edges of the facets corresponding to the hcp twin grain boundaries, and the vertices with 5-fold rotation symmetry.

We have also applied the same cooling procedure on smaller gold clusters with $N = 603$ and $N = 1409$ atoms. In Fig. 4.2 we show the instantaneous configurations of $N = 603$ and $N = 1409$ at $T = 200$ K, with surface atoms shaded by their maximal

local curvature (as was done in Fig. 4.1a for $N = 2624$). We again clearly see the Ih structure, however for the smaller cluster, the edges and facets appear slightly rounded.

An interesting feature of our clusters that cannot be seen in Figs. 4.1 and 4.2 is that all of our clusters formed with a missing central atom. The energetics of such vacancies at the center of Ih clusters were first considered by Boyer and Broughton [90] for Lennard-Jones clusters and later by Mottet *et al.* [91] for Cu, Ag, and Au particles. Above a certain material dependent critical size, the central vacancy lowers the energy of the cluster by partially releasing the strain caused by the mismatch of the tetrahedral units. Mottet *et al.* concluded that for gold particles, the introduction of the central point defect does not lower the energy enough to make the Ih structure competitive with crystallographic octahedra and Wulff polyhedra. However, their energy calculations neglected the entropic contributions at finite temperature. Therefore, our simulations at finite temperature suggest that such a vacancy can in fact stabilize the Ih clusters of thousands of atoms, making them the observed structure upon cooling.

It is interesting to note in Figs. 4.1 and 4.2 that the fcc tetrahedra of our clusters are not all of equal size. To check if this asymmetry is merely caused by the non-magic number N of atoms, we have also cooled clusters with magic numbers $N = 560$ and $N = 1414$ from liquid to 200 K using the exact same cooling procedure. Note that these sizes are actually one atom less than the magic number given by Eq. 2.1 since we have constructed these atoms with a missing central atom to be consistent with our results obtained from cooling the other more generic sizes. These clusters also formed asymmetric Ih structures with 20 facets of slightly unequal sizes. This suggests that our cooling procedure, while slow enough to balance surface vs. bulk free energy and find the Ih structures, is not slow enough to achieve the perfect global equilibration which one expects would result in perfectly symmetric Ih structures for magic numbers N .

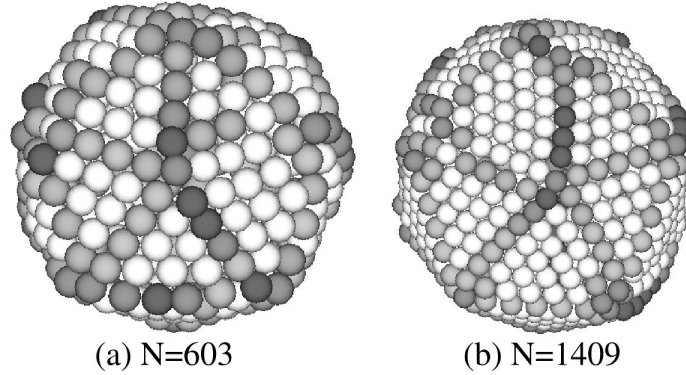


Fig. 4.2: Ih structure of gold clusters with (a) $N = 603$ and (b) $N = 1409$ atoms at $T = 200$ K. The atoms on the surfaces of these instantaneous configurations are shaded according to the maximal local curvature; the larger the curvature, the darker the gray scale.

4.2 Melting and the Bond Orientational Order Parameters

Having determined that our cooled from liquid clusters have the Ih structure, we then heated up the clusters using constant temperature MD instead of the Andersen thermostat, so that the total linear and angular momenta are conserved and vanish; this ensures that our clusters neither translate nor rotate during the course of our simulations. We heat in temperature intervals of 100 K when far from T_m , but use smaller intervals when approaching T_m . At each temperature the clusters have been equilibrated for 10^6 MD steps (4.3 ns), followed by 10^7 steps (43 ns) to collect data.

In Fig.4.3 we show the caloric curve (average potential energy per atom vs. temperature) for several of our cluster sizes, upon heating. The sharp kink in each curve indicates the cluster melting transition. Several expected trends [50] are clearly seen: (i) the melting temperature increases as the cluster size increases, and (ii) the average potential energy per atom increases as the cluster size decreases, due to the larger surface to volume ratio. No qualitative difference is seen between the magic

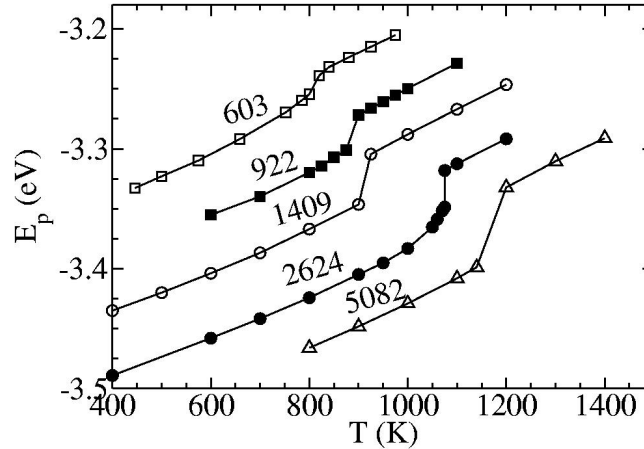


Fig. 4.3: Caloric curve of Ih gold clusters with $N = 603$, 1409, and 2624 atoms, as well as with magic numbers of $N = 922$ and 5082 atoms with a missing central atom.

number sizes, $N = 922$ and 5082, and the others. Note that the glue model gives a melting temperature of 1357 K for bulk gold, well above that of our biggest cluster [38]. The experimentally measured melting temperature of bulk gold is 1337 K [31].

We have done our most careful heating for the $N = 2624$ atom cluster, taking fine temperature increments near T_m . Heating at the above rate of 43 ns per temperature, we find that the cluster has a first order melting transition at $T = 1075$ K. However, when we simulated the cluster at the slightly lower temperature of $T = 1070$ K for more than 240 ns, we found that it also ultimately melted. Thus the estimates of T_m from Fig. 4.3 are most likely slightly higher than the true equilibrium values. This superheating that we find is perhaps related to the extraordinary stability of the gold $\{111\}$ surface, as was also observed in a slab-like geometry [25].

To check for hysteresis about the melting transition, we have also cooled our $N = 2624$ cluster very slowly from a liquid drop at $T = 1200$ K, using temperature intervals of 5 K with a simulated time of 43 ns at each temperature. We found, however, that the cluster remains a perfect liquid down to temperatures as low as 955 K. One can thus question the accuracy of our melting transition temperature

$T_m \simeq 1075$ K. However, it is well known [25] that crystal forming liquids are much more easily supercooled than is the crystal superheated. Experimental results, shown in Fig. 2.10, suggest that our $N = 2624$ atom cluster, with diameter ~ 4.3 nm, should melt at ~ 1050 K. We therefore believe that our estimate of T_m from heating is indeed fairly close to the true melting transition, and our results from slow cooling just reflect the higher metastability of the supercooled liquid as compared to the superheated solid.

Next we explore the melting transition from the perspective of the bond orientational order parameters, defined in Section 3.3. In order to separate the behavior of the surface from that of the interior, we use the cone algorithm recursively to group the atoms of the cluster into successive layers. The outer most layer of atoms is identified as the surface layer; the atoms immediately below the surface layer are called the first sub layer, then the second sub layer, and so on. For the cluster of $N = 2624$ atoms there are totally 9 such layers. We label the atoms lying below the fourth sub layer as “interior” or “bulk” atoms. For $N = 2624$, we show in Table 4.1 the number of atoms in each layer for various temperatures up through melting. We can see from the table that for $T < T_m \simeq 1075$ K, for all layers below the second sub layer, the number of atoms in a given layer remains essentially constant within about ~ 5 . However, for the surface and top two sub layers, the numbers have a more noticeable variation, suggesting changes on the surface of the cluster well below melting.

Having made this division into layers, we then compute the four bond orientational order parameters Q_4 , Q_6 , \hat{W}_4 , and \hat{W}_6 , defined in Section 3.3, separately for each layer and for the bulk. In Fig. 4.4 we show our results for the $N = 2624$ atom cluster; Fig. 4.4a is for the interior atoms, while Fig. 4.4b is for the surface atoms. Comparing to the values listed in Table 3.1, or equivalently as shown in Fig. 3.3, we see that the values found at low temperature are quite consistent with the bulk and surface values for an ideal Ih structure except \hat{W}_4 , which now is approximately zero,

Tab. 4.1: Average numbers of atoms in the surface layer, the sub layers and the bulk of an $N = 2624$ atom gold cluster at different temperatures.

T	Surface	Sub layer 1	Sub layer 2	Sub layer 3	Sub layer 4	Bulk
400 K	855 ± 0.6	602.8 ± 0.8	428.3 ± 1.1	307.4 ± 1.1	207.2 ± 0.8	219.6 ± 1.1
600 K	859.8 ± 1.2	602.2 ± 1.4	427.9 ± 1.2	307.3 ± 1.1	207.2 ± 0.9	219.7 ± 1.1
900 K	867.7 ± 2.4	594.9 ± 2.6	427.5 ± 1.4	307.0 ± 1.2	207.0 ± 1.0	219.9 ± 1.1
1060 K	869.9 ± 3.6	582.4 ± 4.0	436.2 ± 3.2	311.3 ± 2.6	208.6 ± 2.2	215.7 ± 3.2
1100 K	874.7 ± 3.9	572.4 ± 4.2	436.2 ± 4.2	308.7 ± 4.0	209.9 ± 3.7	222.1 ± 5.1

rather than the negative or positive number shown in Table 3.1. Note that errors for all parameters except \hat{W}_4 are reasonably small, however for \hat{W}_4 the estimated error is quite large, representing large shape to shape fluctuations. Since \hat{W}_4 oscillates between the positive and negative values for the perfect Ih structure shown in Fig. 3.3, we conclude that \hat{W}_4 is very sensitive to the exact symmetry of the Ih structures; structural changes between instantaneous configurations induce the very large sample to sample fluctuations for \hat{W}_4 , which then average out to zero.

In Fig. 4.4a for the interior atoms, we see that the bulk bond orientational order parameters remain roughly constant until just above 1000 K, before taking a sharp drop towards zero at the same melting temperature, $T_m \simeq 1075$ K, as found from the caloric curve of Fig. 4.3. Thus the bond orientational order parameters give a good signature of the melting transition. The sharp decrease of the bond parameters indicates that the interior atoms remain with a highly ordered Ih structure until just before melting. Note that the values in the liquid above T_m are not identically zero, but have small finite values due to the finite size of the liquid cluster; this effect is biggest for Q_6 .

In Fig. 4.4b for the surface atoms, we again see that the bond orientational order parameters remain with their Ih values at low temperatures, and then vanish towards zero at the *same* T_m as for the bulk atoms. Thus we reach one of our most important conclusions: the presence of finite surface bond orientational order up until the bulk melting transition indicates that the surface $\{111\}$ facets of the Ih structure do *not* premelt, but rather *the $\{111\}$ facets melt at the same temperature as the bulk*. Since no sharp changes are seen in the surface bond orientational order parameters below T_m , we conclude that there are no other types of surface phase transitions below T_m . However, one noticeable difference in the behavior of the surface bond orientational order parameters as compared to the bulk is that the surface parameter Q_6 starts a noticeable decrease from its low temperature value at $T \sim 800$ K, considerably below

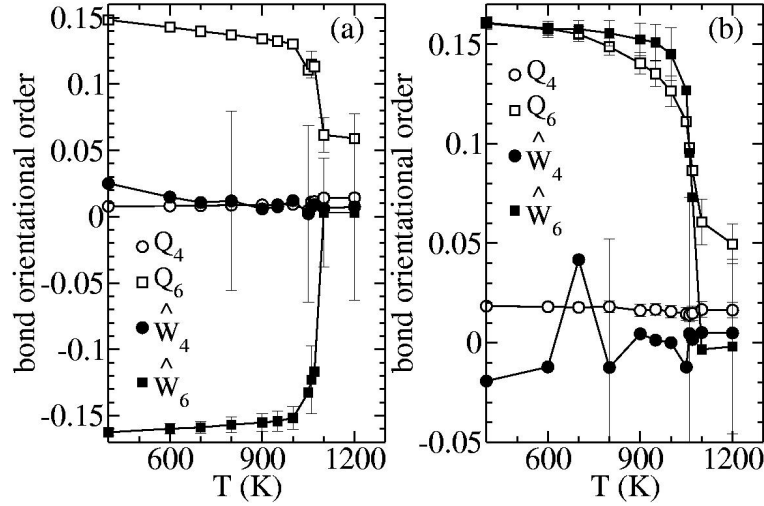


Fig. 4.4: Bond orientational order parameters of the $N = 2624$ atom cluster for (a) the interior atoms, and (b) the surface atoms. Sample error bars, representing configuration to configuration fluctuations, are shown.

the melting T_m . We interpret this as a softening of the surface, and we will study this phenomenon by analyzing the behavior of the surface in the following sections.

Besides the interior and the surface, we have also measured the bond orientational order parameters for the first through fourth sub layers of the cluster. In Fig. 4.5 we show the measured value of Q_6 , which is the bond order parameter most sensitive to the surface softening, for the different sub layers. Because the different layers have slightly different values of Q_6 at low temperatures, we show in Fig. 4.5 the normalized values $Q_6^*(T) \equiv Q_6(T)/Q_6(T = 400\text{K})$ to see the tendency of softening in each layer. We see that the surface and the first sub layer have an almost identical softening behavior which is already obvious at $T = 800$ K. In contrast, no significant softening can be seen for the deeper layers or the bulk below T_m .

We have also tested the sensitivity of our definition of the “interior” atoms of the cluster, by redefining it to be *all* the atoms below the surface layer. Computing the bulk bond orientational order parameters defined this way gives no qualitative change from the behavior seen in Fig. 4.4a.

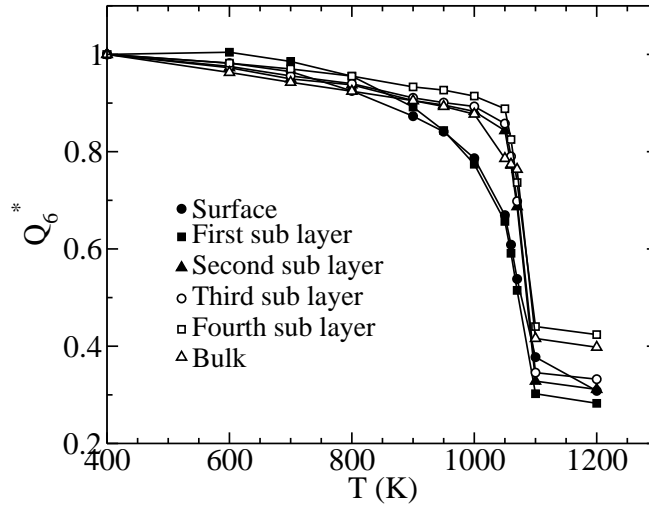


Fig. 4.5: Q_6^* for different layers of the $N = 2624$ atom cluster. In order to see the tendency of softening in each layer clearly, the values of Q_6 have been normalized by their values at low temperature $T = 400$ K, $Q_6^* = Q_6(T)/Q_6(400 \text{ K})$.

In Figs. 4.6 to 4.9 we show similar plots of interior and surface bond orientational order parameters for our other cluster sizes, $N = 603, 922, 1409$ and 5082 . We see the same qualitative behaviors as in Fig. 4.4, with surface and bulk melting at the same temperature. This melting temperature, which increases with cluster size, agrees with the values found from the caloric curves of Fig. 4.3. Surface *softening* tracks the melting temperature and starts to be noticeable about 200 K below T_m . The surface softening is somewhat enhanced for the smaller cluster sizes. There appears to be no qualitative differences for our magic number clusters, $N = 922$ and 5082 , as compared to the other sizes.

4.3 Average Shape and Surface Curvature

To understand the physical reasons for the surface softening indicated by the surface bond orientational order parameters, we now look at the average shapes of our cluster,

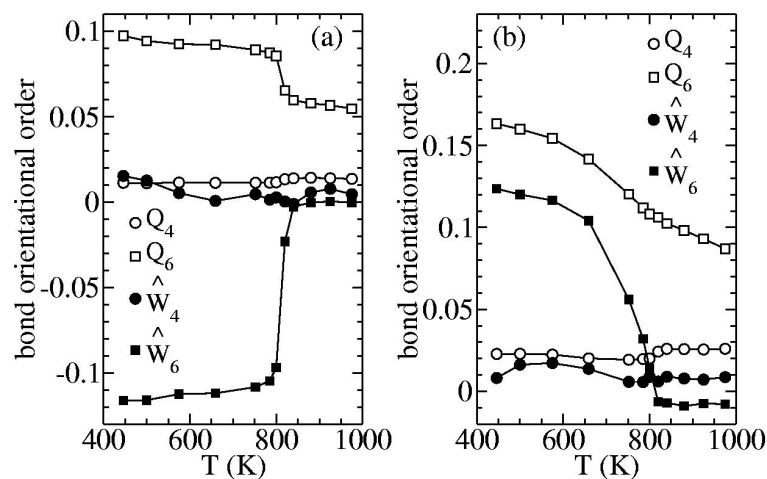


Fig. 4.6: Bond orientational order parameters of the $N = 603$ atom cluster for (a) the interior atoms, and (b) the surface atoms.

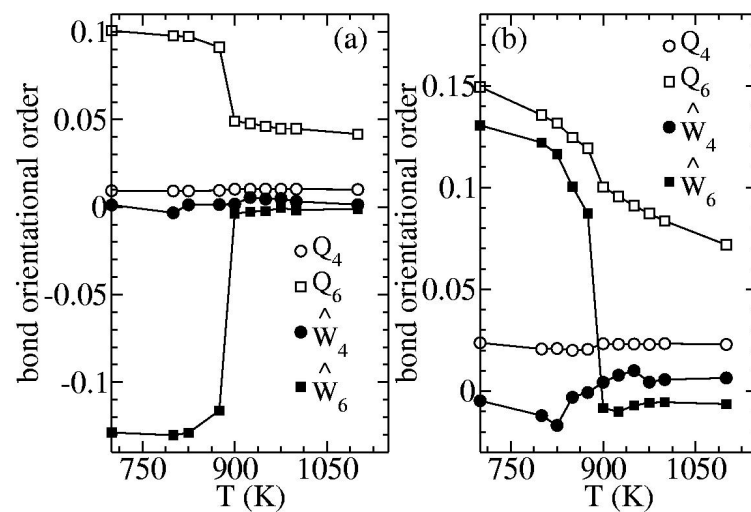


Fig. 4.7: Bond orientational order parameters of the magic number $N = 922$ atom cluster for (a) the interior atoms, and (b) the surface atoms.

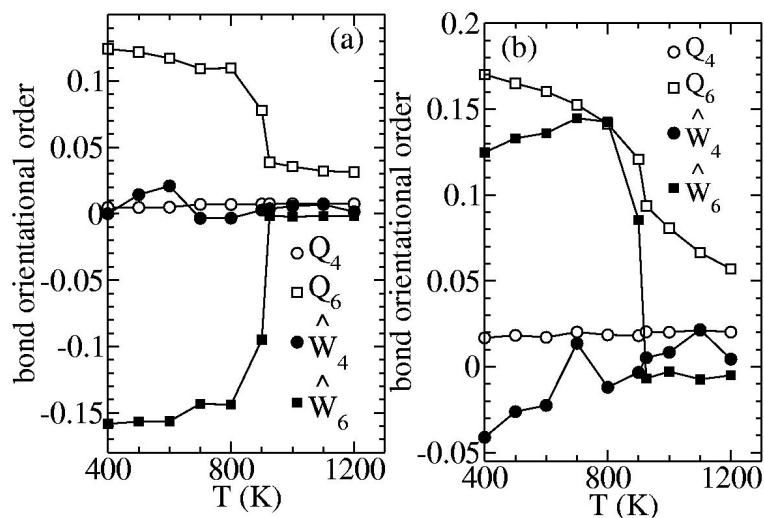


Fig. 4.8: Bond orientational order parameters of the $N = 1409$ atom cluster for (a) the interior atoms, and (b) the surface atoms.

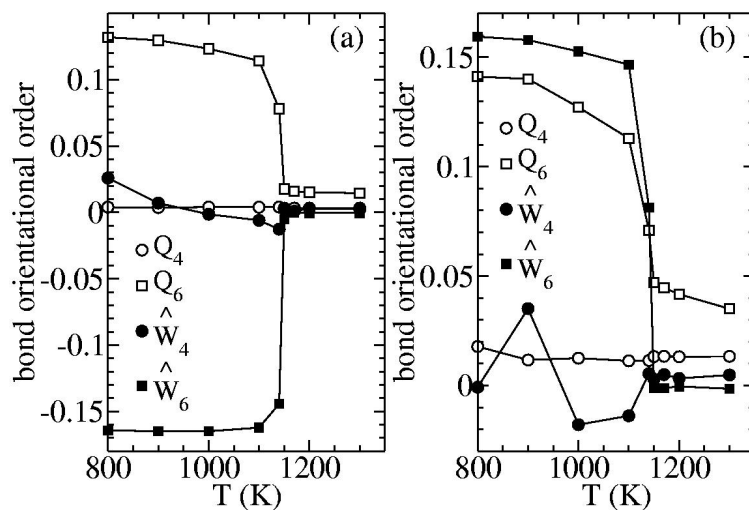


Fig. 4.9: Bond orientational order parameters of the magic number $N = 5082$ atom cluster for (a) the interior atoms, and (b) the surface atoms.

computed according to the method of Section 3.5.3. We first focus on our cluster of $N = 2624$ atoms. For this case, we have divided the 4π total solid angle into 842 almost equal solid angles, using the icosahedral covering of Ref. [89]. We have chosen this number since it is closest to the typical number of surface atoms in this cluster (see Table 4.1). At each temperature over 1000 instantaneous configurations, sampled at equal intervals throughout the simulated time of 43 ns, have been included in our average. We show the resulting average shapes in Fig. 4.10. We present results for the following temperatures: 400 K, representing the low temperature configuration in which atoms only vibrate about their crystal sites; 600 K where small changes start to appear on the surface; 900 K where softening of the surface orientational order parameter Q_6 is obvious; 1060 K, just below the melting $T_m \simeq 1075$ K; and $T = 1100$ K just above T_m .

In the top row of Fig. 4.10 we show pictures constructed similarly to that in Fig. 3.9c of Section 3.5.3, which showed the average shape of the liquid cluster at $T = 1200$ K. The small spheres represent the average position of the surface within the given solid angle. Additionally, we have now shaded these spheres according to the value of the maximal local surface curvature, as we did earlier in Fig. 4.1a for an instantaneous configuration at $T = 200$ K; the darker the gray scale, the larger the curvature. This method of shading is used to highlight any edges and facets that are on the cluster surface. The view point for these pictures is taken at infinity, so as to show a full hemisphere of solid angle.

In the bottom row of Fig. 4.10 we show the corresponding average shapes using a smooth 3D contour plot with overhead lighting. The view point for these bottom row pictures is now taken to be a finite distance from the cluster, in order to highlight the straight edges and 5-fold rotation symmetry about the vertices.

The pictures in Fig. 4.10 illustrate the following scenario as the cluster is heated. At low temperatures the cluster is almost fully faceted, with flat facets meeting at sharp edges and vertices. By 900 K the facets have shrunken slightly in size and

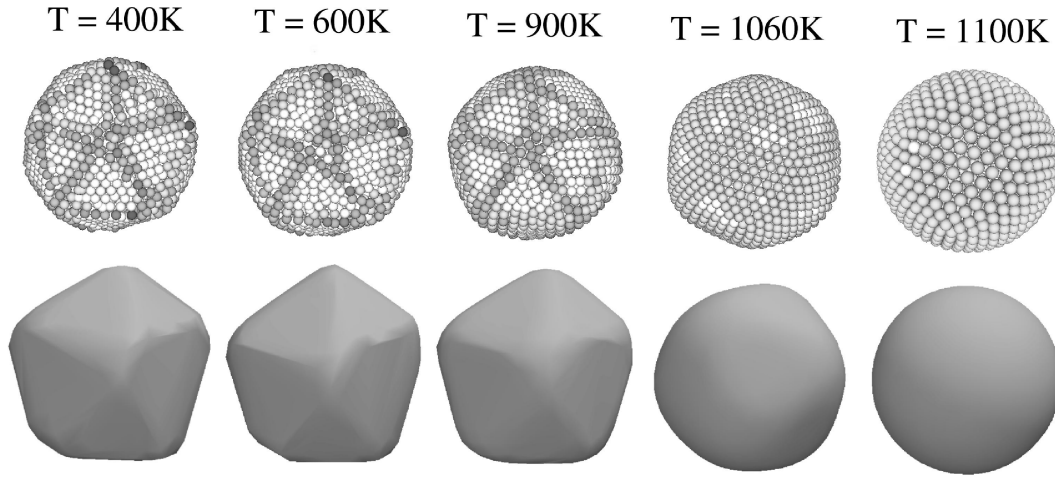


Fig. 4.10: Average shapes of an $N = 2624$ atom cluster at 400, 600, 900, 1060 and 1100 K. The top row shows each of the discretized solid angles of the surface shaded according to the value of the maximal local curvature; the darker the gray scale, the larger the curvature. The viewpoint of these pictures is set to infinity, to show a full hemisphere of solid angle. The bottom row is the corresponding smooth contour plot, with a finite viewpoint so as to highlight the straight edges and 5-fold rotation symmetry about the vertices.

the edges and vertices have noticeably rounded. At 1060 K, just below melting, the facets have shrunk to almost negligible size, and the cluster is almost spherical. Above melting, the cluster is essentially a perfect sphere.

To quantify the cluster shapes we have computed the bond curvatures c_b and the maximal local surface curvatures κ_M , as defined in Section 3.5.2. In Figs. 4.11a–d we show histograms of bond curvature c_b for the four temperatures 600, 900, 1060 and 1100 K. The solid curves show the histograms of bond curvatures as computed over the surface bonds of the *average* cluster shape shown in Fig. 4.10. In contrast, the dashed curves show the histograms of bond curvatures computed for an *instantaneous* cluster configuration, and then averaged over the 1000 instantaneous configurations

saved in our simulated time of 43 ns. Note that we have only one average configuration for the average shape, so the corresponding histograms have some fluctuations due to the relatively small number of data points. We have smoothed these fluctuations by using a Gaussian smoothing function with a width of 4 bins. The bin size here is 0.006 \AA^{-1} . In Figs. 4.12a–d we show the analogous histograms for the maximal local curvature κ_M . The bin size here is 0.02 \AA^{-1} . Note that κ_M can be negative, corresponding to a region where the surface is locally concave; an example of when this can happen is near a vertex which is missing its top most atom.

Both Figs. 4.11 and 4.12 illustrate the same scenario. First let us consider the histograms of the average cluster shapes (solid lines). At low temperatures, the histograms have a strong peak at zero, representing the low curvatures of the large flat facets. The histograms also show either a second peak or plateau at higher curvature, with a long high curvature tail, representing the large curvatures at edges and vertices. These two features correspond to the δ functions in Fig. 3.8 for the ideal Ih structure. In the liquid above $T_m \simeq 1075 \text{ K}$, the histograms are a single sharp peak at finite curvature, representing the uniform curvature of the spherical liquid cluster. Just below melting, at $T = 1060 \text{ K}$, the histograms similarly show a single peak near that of the liquid, only noticeably broader than for the liquid; this indicates the shrinkage of the flat facets to negligible size and a rounded cluster that is not yet a perfect sphere.

Comparing the histograms for the average vs. the instantaneous shapes, the latter (dashed lines) are in general broader, especially for high temperatures near T_m . For $T = 1060 \text{ K}$ just below T_m , and for $T = 1100 \text{ K}$, just above T_m , the histograms for the instantaneous configurations have a low curvature peak corresponding to a spherical or nearly spherical cluster, just like the histograms for the average shape. However, they also have more low curvature data, and a broad high curvature tail, similar to the histograms at lower temperatures. This suggests that even at high temperatures, the instantaneous configurations can still develop small local facets

on the surface, which contribute to the lower and higher curvatures than the peak value corresponding to the sphere. A similar observation has previously been made by Lewis *et al.* for clusters of hundreds to thousands of atoms [55]. Averaging over the instantaneous fluctuations results in a smoothing out of the facets to negligible size when one considers the *average*, rather than the instantaneous, cluster shape. We have seen evidence for this scenario by visual inspection of instantaneous cluster configurations. See for example Fig. 3.9, where one can see small flat regions on the irregular surface of the *instantaneous* shapes in Figs. 3.9a and b.

For comparison with other sizes, we show in Fig. 4.13 average cluster shapes for our $N = 1409$ atom cluster at temperatures 800 K and 900 K, where $T_m \simeq 925$ K. In Fig. 4.14 we show average shapes for our magic number $N = 5082$ atom cluster at temperatures 1000 K and 1140 K, where now $T_m \simeq 1150$ K. The gray scale in these figures is the same as used in Fig. 4.10. Again we see facets shrinking, and the cluster becoming more spherical, as T_m is approached.

4.4 Diffusion of Atoms

In this section we present evidence that the physical mechanism behind the surface softening is the diffusion of atoms on the vertices and edges of the cluster. We will consider in this section primarily the cluster of $N = 2624$ atoms.

We first consider the *inter*-layer mixing of atoms in the cluster. We define an inter-layer mixing parameter $\langle n \rangle$ as follows. At each temperature we label the atoms in the initial configuration by an integer $n' = 0, 1, 2, \dots, 5$ according to whether the atom is on the surface, in the first sub layer, second sub layer, \dots , or interior of the cluster. At the end of the simulation for that temperature, we assign a new integer n to each atom, according to which layer the atom is now in. In Fig. 4.15 we plot $\langle n \rangle$ vs. T , where n is averaged separately over each group of atoms indexed by their initial layer number n' . The noticeable difference of $\langle n \rangle$ from the initial n' indicates significant inter-layer mixing of the atoms from layer n' into other layers. From

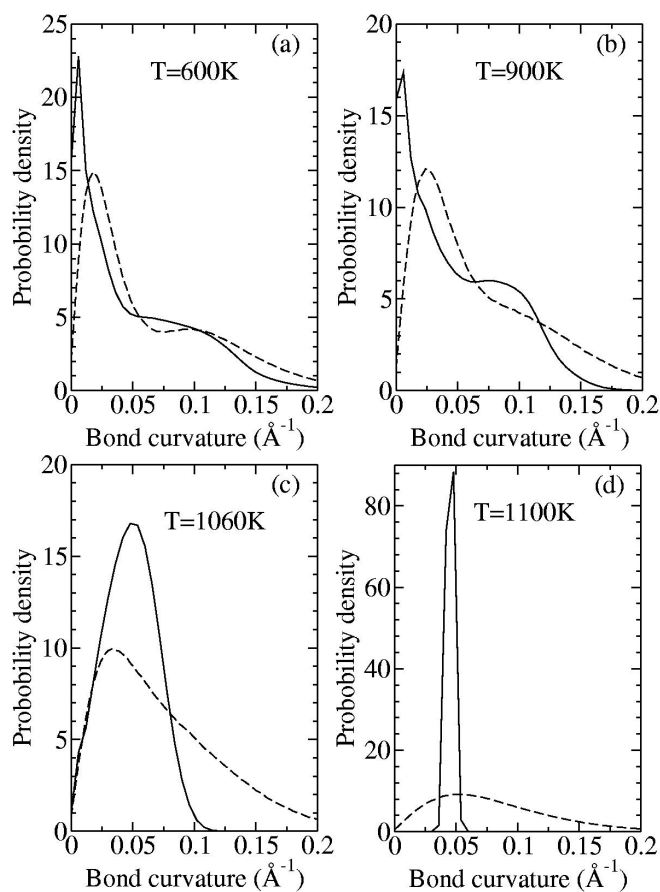


Fig. 4.11: Histograms of bond curvature c_b for the average cluster shape (solid lines) and the instantaneous cluster configurations (dashed lines) at (a) $T = 600\text{K}$, (b) $T = 900\text{K}$, (c) $T = 1060\text{K}$, and (d) $T = 1100\text{K}$. The cluster size is $N = 2624$ atoms.

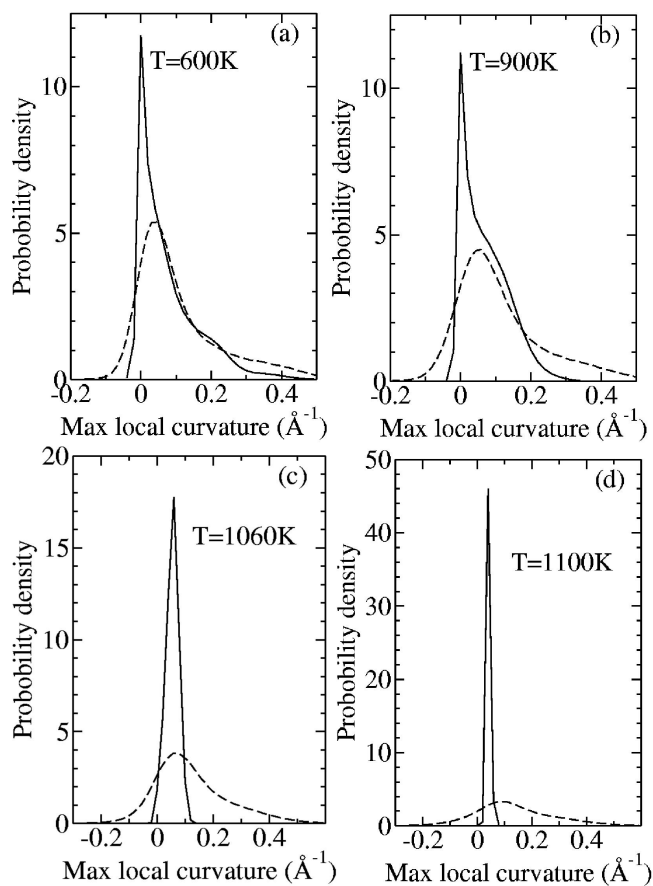


Fig. 4.12: Histograms of maximal surface curvature κ_M of the average cluster shape (solid lines) and the instantaneous cluster configurations (dashed lines) at (a) $T = 600\text{K}$, (b) $T = 900\text{K}$, (c) $T = 1060\text{K}$, and (d) $T = 1100\text{K}$. The cluster size is $N = 2624$ atoms.

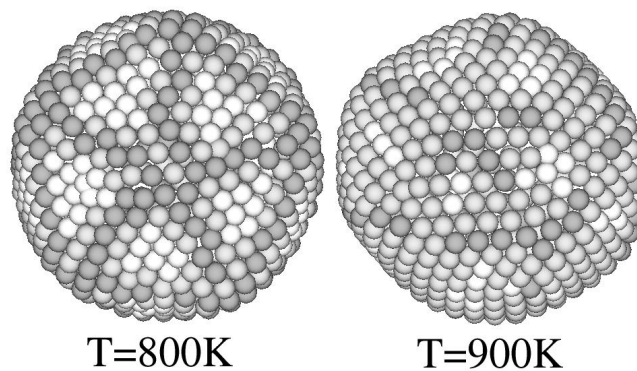


Fig. 4.13: Average cluster shapes for an $N = 1409$ atom cluster at temperatures 800 K and 900 K, where $T_m \simeq 925$ K. Points are shaded according to the value of the maximal curvature; the darker the gray scale, the larger the curvature.

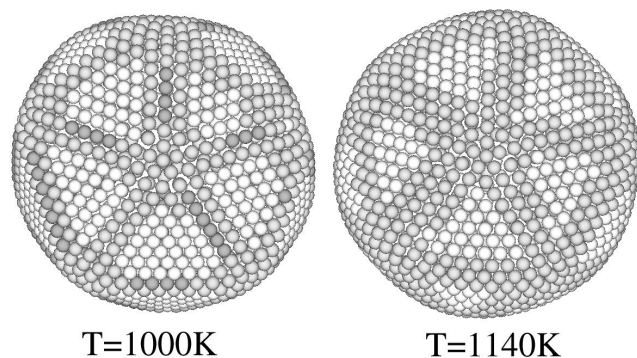


Fig. 4.14: Average cluster shapes for an $N = 5082$ atom cluster at temperatures 1000 K and 1140 K, where $T_m \simeq 1150$ K. Points are shaded according to the value of the maximal curvature; the darker the gray scale, the larger the curvature.

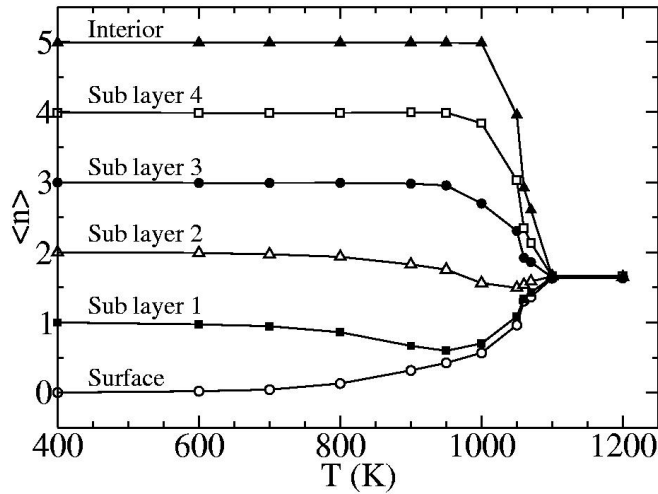


Fig. 4.15: Interlayer mixing parameter $\langle n \rangle$ vs. T , for atoms initially on the surface, in the first sub layer, ..., and in the interior. The cluster size is $N = 2624$ atoms.

Fig. 4.15 we see that noticeable inter-layer mixing takes place between the surface and the first sub layer as low as 700 K; these two layers are almost evenly mixed by 950 K, more than 100 K below the melting $T_m \simeq 1075$ K. As T_m is approached, additional layers start to mix together. At T_m and above, all layers are evenly mixed during the course of the simulation, indicating that in the liquid all atoms diffuse equally throughout the entire cluster.

Next we consider the diffusion of the atoms in the cluster by computing the mean squared displacements, $\Delta r^2(t)$, defined in Eq. (3.18). We compute $\Delta r^2(t)$ separately for each layer of the cluster (and the interior) by averaging only over the atoms that are *initially* in a given layer. In Figs. 4.16a–d we plot our results for $\Delta r^2(t)$ vs. t , layer by layer, for the four different temperatures, 600, 900, 1060 and 1100 K. Note that since atoms in different layers can mix (see Fig. 4.15), the division into different layers in Fig. 4.16 contains some ambiguity; an atom initially in the first sub layer, for example, might during the course of the simulation wind up on the surface, however we continue to average its motion in with that of the first sub layer.

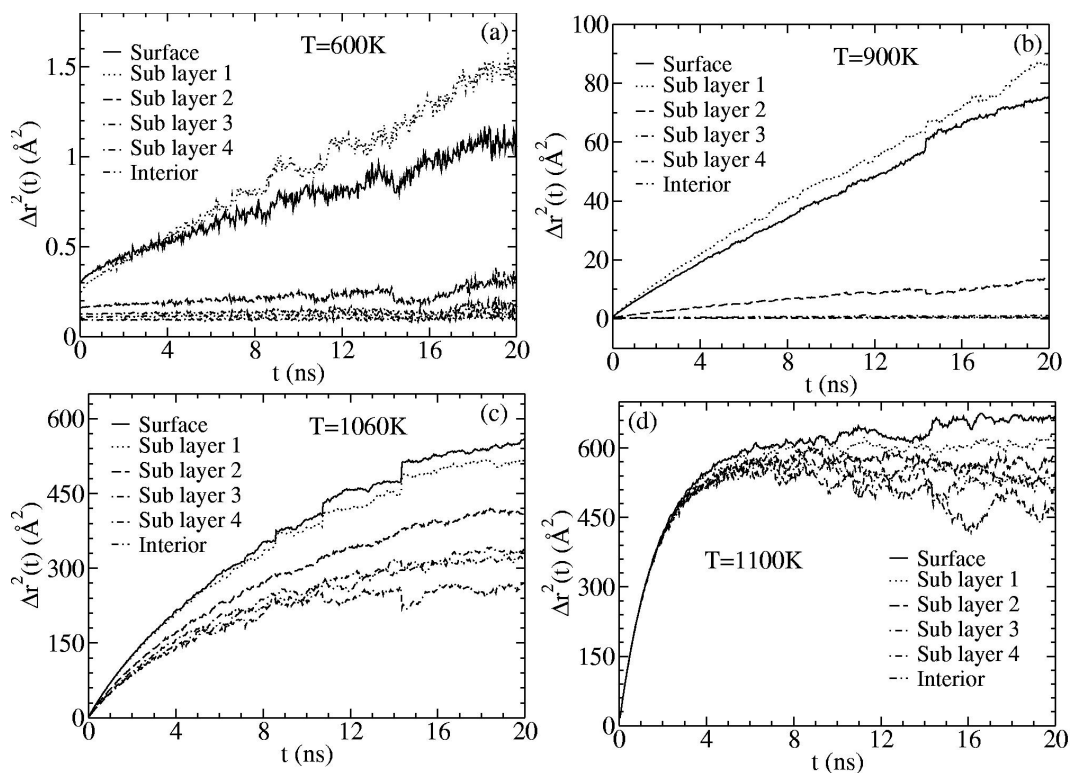


Fig. 4.16: Mean squared displacements for the $N = 2624$ atom cluster averaged over the atoms in the surface layer, first through fourth sub layers, and interior for (a) 600 K, (b) 900 K, (c) 1060 K, and (d) 1100 K.

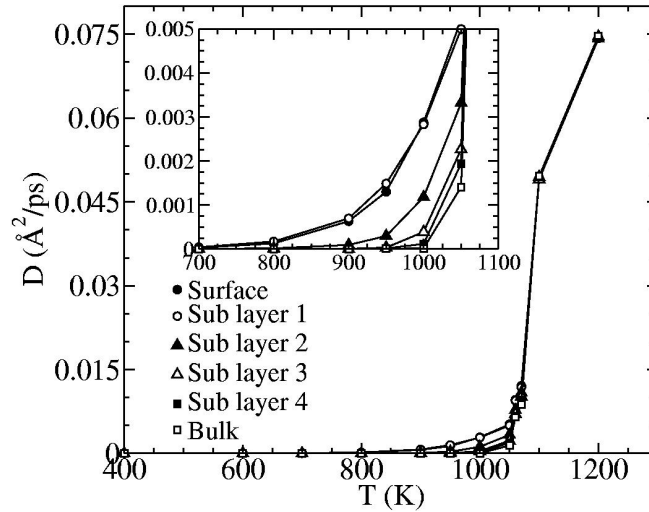


Fig. 4.17: Diffusion coefficients D vs. T for different layers of the $N = 2624$ atom cluster. The inset shows an expanded range for D in a temperature range below melting, 700 – 1050 K.

Several expected features are apparent in Fig. 4.16. In Fig. 4.16d at 1100 K, above the melting $T_m \simeq 1075$ K, we see that the mean squared displacements of all layers saturate at $\Delta r^2 \sim 600 \text{ \AA}^2$, representing that all the atoms can diffuse throughout the entire liquid cluster, no matter which layer they were initially in. At the low temperature of 600 K, where the average cluster shape remains almost fully faceted, the results in Fig. 4.16a show that diffusion is almost negligible. Even for the two top layers, atoms on average move less than one inter-atomic spacing ($\sim 3 \text{ \AA}$) over the observation time of 20 ns. At 900 K, where the edges and vertices of the average cluster shape have noticeably rounded, we see in Fig. 4.16b that diffusion in the top two layers is significant, with atoms on average traveling a root mean square distance equal to several inter-atomic spacings. The second sub layer also shows a noticeable diffusion. The diffusion of all other layers are negligible. At 1060 K, just below the melting $T_m \simeq 1075$ K, we see that all atoms are diffusing throughout the cluster, with the top two layers almost reaching the long time saturation value $\sim 600 \text{ \AA}^2$ found in the liquid.

In Fig. 4.17 we plot the diffusion constant $D = \Delta r^2/6t$ vs. T for each of the cluster layers, obtained by fitting to the early time linear part of the curves in Fig. 4.16. We fit our diffusion constant for the surface layer to the simple form $D = D_0 \exp(-E_A/k_B T)$ to extract the activation energy, $E_A = -d(\ln D)/d(1/k_B T)$. We find the values of $E_A = 0.21$ eV at low temperatures, ~ 500 K, where the cluster is fully faceted. At high temperature, ~ 1200 K, in the liquid, we find $E_A = 0.35$ eV. Note that the first value corresponds to surface diffusion, while the second value corresponds to *bulk* diffusion in the liquid, since in a liquid the atoms initially on the surface will easily diffuse into the bulk. Boisvert et al. [92] did a first principles (*ab initio*) calculation for the gold {111} surface at low temperatures and found $E_A = 0.22 \pm 0.03$ eV, in good agreement with our value. Chushak and Bartell [11] reported the value of $E_A = 0.25$ eV using the EAM model for a liquid gold nanocluster. Considering the tendency of the EAM model to systematically give lower energy values (as pointed out in Ref. [93]), our result for the liquid is in reasonable agreement.

Returning to Fig. 4.16, it seems paradoxical that, for the lower temperatures of Figs. 4.16a and b, the diffusion of atoms in the first sub layer appears to be greater than that for atoms on the surface. By noting that the Δr^2 in Fig. 4.16 represents an *average* over *all* the atoms in a given layer, we can explain the paradox as follows. The surface layer has more atoms than the first sub layer. If we multiply the values of Δr^2 in Figs. 4.16a and b by the number of atoms N_i in each respective layer, we find that $N_i \Delta r^2$ is almost equal or slightly larger for the surface layer than the first sub layer. This suggests that at low temperatures it is a similar *small number of atoms* in each of the two top layers that are diffusing. These are the atoms along the edges and vertices of the layers (i.e. on the hcp twin grain boundaries separating the fcc tetrahedra). When the temperature increases to 1060 K, most of the atoms in the two layers are now diffusing, and the average mean squared displacements Δr^2 of the two layers become roughly equal.

In order to know how many atoms contribute to the diffusion in each layer, we have computed the number of *moved* atoms in each layer. At each temperature, the moved atoms are defined as those atoms that *once* have traveled a distance from their initial positions larger than a certain cutoff. Sampling over 500 configurations from the simulated time of 21.5 ns, we count the number of moved atoms in each surface layer and the bulk, respectively for the three different cutoff distances of 3.8 Å, 6.1 Å, and 8.0 Å. These distances are the minima between the peaks of the pair correlation function (see Fig. 3.2). The fraction of moved atoms is calculated by dividing the number of moved atoms by the total number of atoms in each layer shown in Table 4.1. The resulting plots are shown in Fig. 4.18. For $T > T_m$, the fraction of moved atoms for all of the layers is equal to 1, showing that, in liquid state, all atoms are free to move. For $T < T_m$, because it is energetically easier for the atoms to hop to neighboring positions than to diffuse over larger distances, the data in Fig. 4.18a are systematically higher than those in Figs. 4.18b and c. There is not much difference however between Figs. 4.18b and c, indicating that now the moved atoms are most likely diffusing, rather than just hopping around their initial crystal sites. We therefore use Fig. 4.18c to discuss the number of diffusing atoms.

As shown in Fig. 4.18c, below $T = 600$ K, in our simulated time of about 20 ns, almost no atoms diffuse. Between 600–900 K similar fractions of atoms in the surface and the first sub layer diffuse, while diffusion in deeper layers remains small. At $T = 1000$ K, almost all of the atoms in the outer most two layers diffuse, some atoms in the second sub layer diffuse, while almost no atoms diffuse in the deeper layers.

Similar plots for the clusters with $N = 1409$ and 5082 atoms, using the cutoff distance of 8.0 Å, are shown in Fig. 4.19 and Fig. 4.20, respectively. Again we see that almost all of the surface atoms diffuse at a temperature somewhat below T_m .

Combining all the above we infer the following scenario for diffusion at the temperatures below T_m : below 1000 K, only atoms on the surface and in the first sub

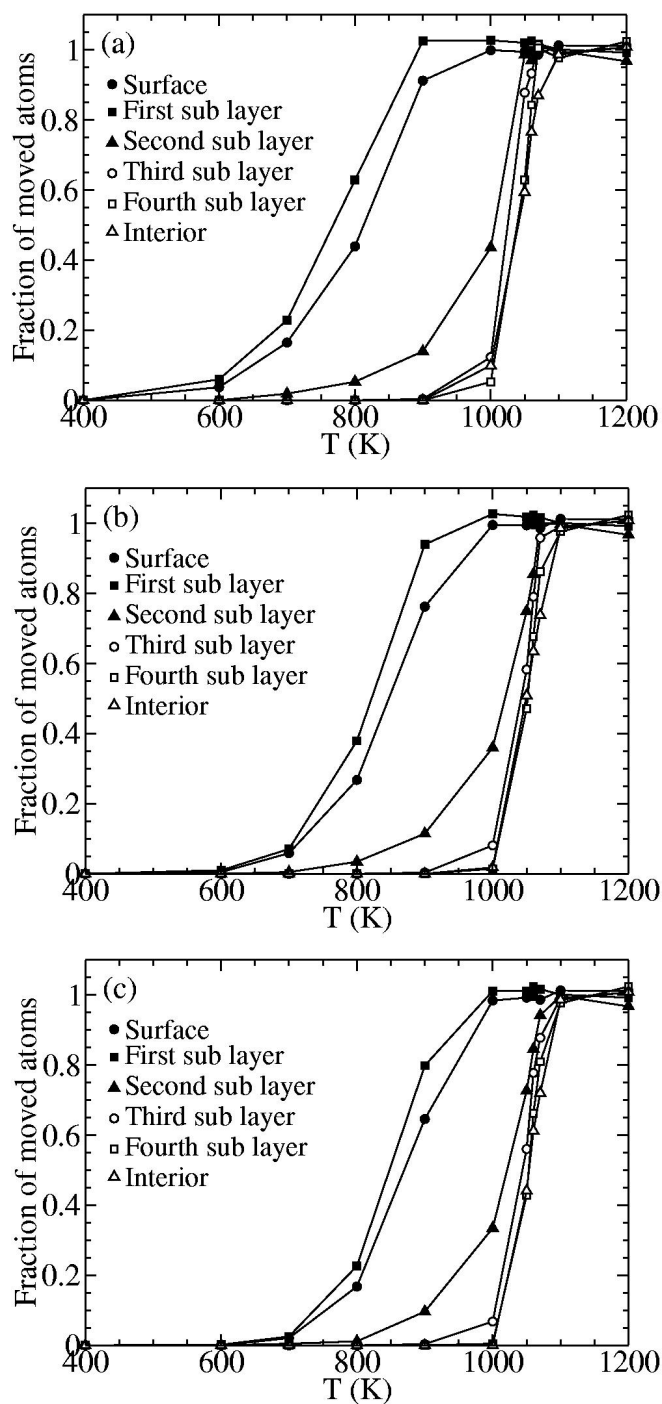


Fig. 4.18: Number of moved atoms for the cluster with $N = 2624$ atoms in the surface layer, first through fourth sub layers, and the interior with the cutoffs of (a) 3.8 \AA , (b) 6.1 \AA , and (c) 8.0 \AA .

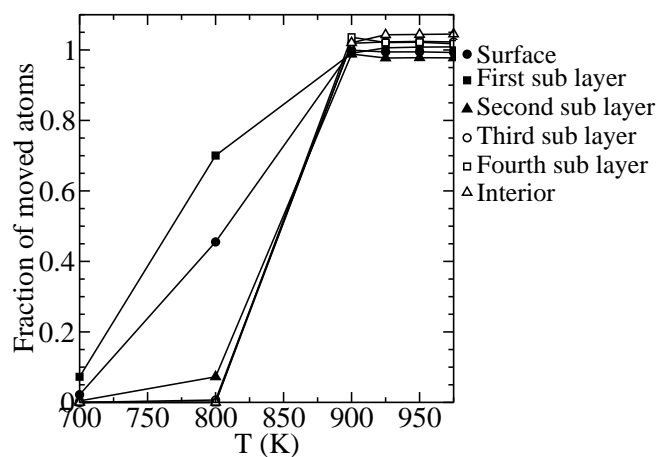


Fig. 4.19: Number of moved atoms for the cluster with $N = 1409$ atoms in the surface layer, first through fourth sub layers, and the interior with the cutoff of 8.0 \AA .

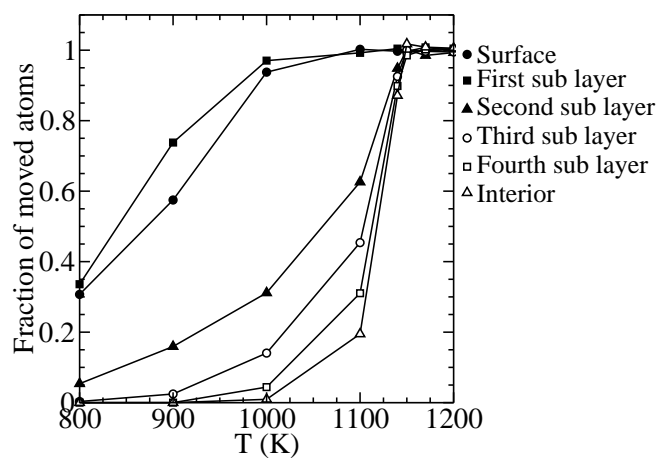


Fig. 4.20: Number of moved atoms for the cluster with $N = 5082$ atoms in the surface layer, first through fourth sub layers, and the interior with the cutoff of 8.0 \AA .

layer show any noticeable diffusion well below T_m . The atoms in these two layers that diffuse are the same atoms which mix between the two layers (see Fig. 4.15), and these are the atoms along the edges and vertices of each layer. The atoms from the first sub layer diffuse by migrating first to the surface, and then diffusing upon the surface, until mixing back into the first sub layer. Above 1000 K, almost of the atoms in the outer most two layers diffuse, however our bond order parameters indicate that the surface remains with a finite structural order. We can reconcile the existence of this bond orientational order and the complete surface atom diffusion as follows. As the vertex and edge atoms become more mobile, with increasing temperature, more and more atoms on the $\{111\}$ facets become disordered, and the facets surrounded by the “liquid” edges become smaller. By the temperature of $T = 1000$ K, the $\{111\}$ facets are so small that most of the atoms on the facet lie on the edges of the facet. These atoms can easily exchange with atoms in the surrounding “liquid” of edge atoms. Thus even atoms on the ordered facets can now diffuse on the surface. However, this atom exchange does not destroy the orientational order of the facets.

To verify the above picture, we plot in Fig. 4.21 the displacement ellipsoids, defined in Section 3.6, for all atoms initially on the surface of our $N = 2624$ cluster. We show results for temperatures 400, 600, 900, 1060 and 1100 K, corresponding to the same temperatures for which we showed the average cluster shape in Fig. 4.10. In the top row we show ellipsoids averaged over a simulated time of 1.075 ns. We expect that atoms which are diffusing, with $\Delta r^2 \sim t$, should have their displacement ellipsoid roughly double in size when the time interval goes up by a factor of four. Hence in the bottom row of Fig. 4.21 we show results for a simulated time of 4.3 ns, i.e. four times longer than the top row. We see the following observations. At 400 K there is no observable diffusion of surface atoms. At 600 K we see diffusion of atoms at the vertices of the Ih cluster. At 900 K we see stronger diffusion at the vertices, as well as diffusion along the edges. One also can see several of the ellipsoids oriented normal to the surface, indicating atoms which are mixing in with the first sub layer.

Atoms at the centers of the facets remain without diffusion. At 1060 K and above almost all of the atoms are clearly diffusing.

4.5 Discussion and Conclusions

We have carried out long time equilibrium molecular dynamics simulations to study the behavior of gold nanoclusters cooled from the liquid, and their melting upon reheating. For three different generic cluster sizes, $N = 603, 1409$ and 2624 , we found that the liquid clusters crystallized to a slightly asymmetric Mackay icosahedral structure with a missing central atom.

We then slowly heated up through melting the above crystallized clusters, as well as several other “magic number” Mackay icosahedra with a missing central atom with up to $N = 5082$ atoms that we constructed by hand. The caloric curves indicate that the melting temperature of the gold clusters decreases when the gold cluster becomes smaller. However, by measuring surface and bulk bond orientational order parameters, we find no surface premelting or roughening of the $\{111\}$ facets of our Ih clusters, and the $\{111\}$ facets on the surface remain ordered up until T_m . Nevertheless, the surface bond parameters decrease from their low temperature values significantly below T_m , indicating a softening of the surface prior to melting. We find that the onset of this surface softening appears to track the size dependent melting, occurring roughly 200 K below $T_m(N)$.

The average shape of our clusters shows that this surface softening corresponds to a rounding of the edges and vertices of the cluster, with a corresponding shrinkage of the $\{111\}$ facet area. The average cluster shape is nearly spherical just below the melting T_m . As the temperature increases towards melting, and in the liquid above T_m , instantaneous cluster configurations can display large thermal fluctuations about this average shape.

Measuring the diffusion of atoms in the cluster, we conclude that the mechanism for this surface softening is the onset of diffusion of atoms, first at the vertices and

then at the edges of the cluster surface, as temperature is increased. As temperature further increases, the mobility of these atoms increases. More and more atoms near the edges of the facets diffuse, until the number of atoms remaining stationary on the facets becomes almost negligibly small near T_m . Simultaneous with this increasing diffusion, interlayer mixing increases, with surface and first sub layers mixing first, and then deeper layers mixing in as one approaches close to T_m .

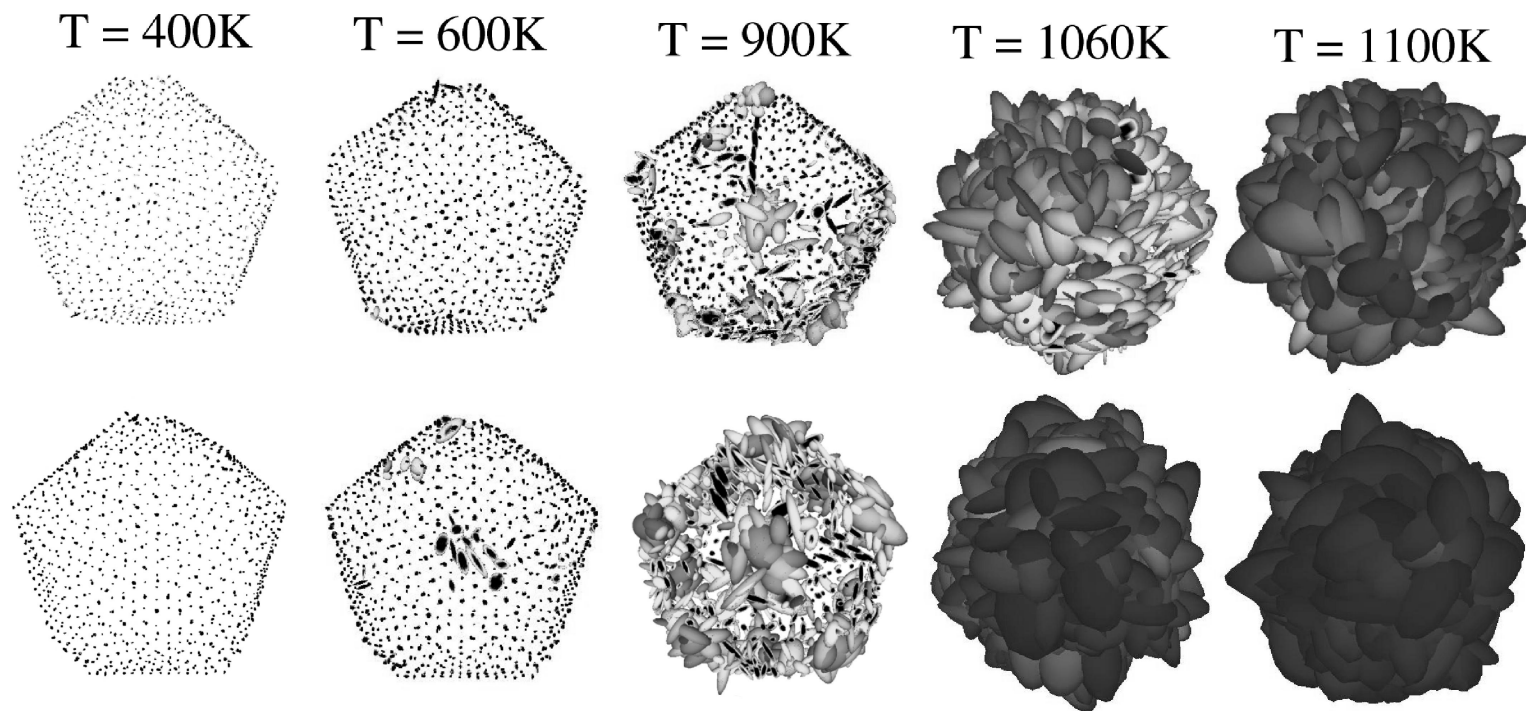


Fig. 4.21: Ellipsoids of displacement at 400, 600, 900, 1060 and 1100 K for the cluster of $N = 2624$ atoms. Each ellipsoid is centered at the average position of the given atom, and shows the directional distribution of root mean squared displacements. The top row gives results obtained for a simulated time of 1.075 ns , while the bottom row is for 4.3 ns .

5. CONTINUOUS HEATING OF GOLD NANORODS

In this chapter we report on our results for gold nanorods under simulated continuous heating, which mimics the experimental laser heating procedure. Our numerical results are compared with experiment.

Since gold nanorods with less than 1000 atoms are unstable in the simulated time of hundreds of picoseconds [75], and simulations of more than 10 000 atoms are computationally too expensive for a thorough statistical analysis, we focus on gold nanorods with 1000 to 10 000 atoms in the present study. In particular, we carry out a detailed analysis of the shape transformation for a rod with $N = 2624$ atoms. Although this size range is much smaller than the experimental rods containing more than 10^6 atoms, we hope our study can qualitatively help in the understanding of experimental results.

5.1 Initial Structure and Heating Rate

As the initial structure for our simulations, we construct a nanorod with the geometry of the short gold nanorods with an aspect ratio of 3.0 studied experimentally by Wang *et al.* [57]. The structural model of these rods has been shown in Fig. 2.13b. They are carved out from a pure fcc crystal with the long axis of the rod along the [100] crystal direction. Their sides consist of four large {100} and four large {110} facets oriented parallel to the rod axis. The end caps of the rod consist of a {001} facet,

four small $\{111\}$ facets connecting the $\{110\}$ and the $\{001\}$ facets, and four small $\{110\}$ facets connecting the $\{100\}$ and the $\{001\}$ facets.

In the experiments [29], the gold nanorods are heated continuously by nanosecond laser pulses, essentially without affecting their environment. To simulate this experimental procedure, we use the continuous heating MD method described in Section 3.2. This method increases the kinetic energy by a fixed amount at each MD step by rescaling the velocities, so that the *total* energy increases linearly in time. Note that since the total energy is the sum of kinetic and potential energies, and since the potential energy can change upon a structural rearrangement of the rod, the kinetic energy alone need not increase strictly linearly in time. We choose a heating rate of 7×10^{12} K/s, which takes 10^5 simulation steps (430 ps) to heat our $N = 2624$ atom rod from 5 K to about 1468 K, well above the melting temperature of bulk gold, $T_m = 1357$ K, given by the glue model [38].

Although we do not have the experimental heating rate, a rough comparison can be made by evaluating the time required to melt the rods. Experimentally it takes at least 30 ps to heat the rods from room temperature (~ 300 K) to complete melting (~ 1300 K) [68]. In Fig. 5.1 we show the instantaneous temperature vs. time during our simulated continuous heating of the rod with $N = 2624$ atoms. Here and throughout the rest of the thesis the instantaneous temperature is defined as $T = 2K/3N$, where K is the instantaneous total kinetic energy, and N is the number of particles. In this curve the sudden increase of the temperature at about 20 ps is due to the surface reorganization which decreases the potential energy of the rod. The flat region around 300 ps is where the melting transition happens, when the system potential energy increases while the temperature keeps relatively unchanged at about 1200 K. From this plot we find that in our simulation, it takes about 280 ps to heat the rod from 300 K to complete melting (~ 1200 K). By noting that 30 ps is the lower bound in experiments, we conclude that our heating rate is roughly in the range comparable to experimental ones.

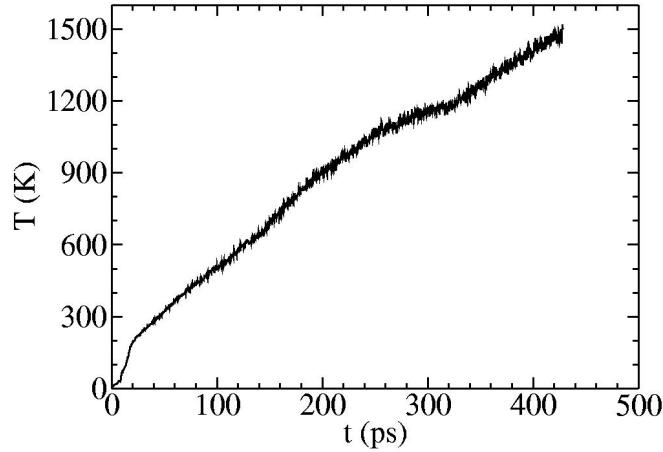


Fig. 5.1: Instantaneous temperature vs. time during continuous heating of the gold nanorod with $N = 2624$ atoms.

5.2 Shape Transformation and Melting Transition

Results from our simulations for the continuous heating of the rod with $N = 2624$ atoms are shown in Figs. 5.2–5.4. Fig. 5.2 shows configurations of the rod at the four instantaneous temperatures of 5, 515, 1064, and 1468 K, representing typical points in the shape transformation and melting process. During heating, the rod becomes slightly shorter at 515 K. Then the rod becomes shorter and wider acquiring an aspect ratio of ~ 1.8 at 1064 K. At 1468 K, above the melting temperature, the rod forms a liquid sphere.

The evolution of some system parameters during heating is depicted in Fig. 5.3 and Fig. 5.4. The average total energy per atom and the average potential energy per atom vs. instantaneous temperature is shown in Fig. 5.3a. The slope of the E vs. T curve changes significantly at about 200, 650, and 1100 K indicating the occurrence of structural and morphological transitions. Fig. 5.3b shows the temperature dependence of the radius of gyration (described in Section 3.4) of the gold nanorod. Before the temperature reaches 200 K, the radius of gyration oscillates due to a thermally

excited long wavelength deformation. Then the radius of gyration decreases very slowly up to 500 K, after which the radius of gyration drops quickly, indicating that the rod collapses to a shorter and wider shape. At 600 K, it plateaus out and then decreases slowly up to 1140 K, when the melting begins and the shorter and wider rod collapses to a liquid sphere. After melting the radius of gyration grows slowly and linearly with temperature reflecting the thermal expansion of the liquid sphere.

The globally averaged bond order parameters (described in Section 3.3) of the internal atoms are shown in Fig. 5.4. Here an internal atom is defined as any atom not on the surface, where the surface atoms are determined by using the cone algorithm described in Section 3.5.1. Comparing with the values given in Table 3.1, we see that for temperatures below 300 K, the internal structure remains almost pure fcc. Then the bond order parameters change slowly with increasing temperature. At about 650K, the internal structure changes quickly to be hcp-dominated, as indicated by the rapid rise of \hat{W}_4 from negative to positive values. This hcp structure stays nearly unchanged until the temperature reaches about 1140 K when the rod melts and the internal atoms acquire the structure of a liquid. Comparing with the radius of gyration plot in Fig. 5.3b, we see that the onset temperature of shape change (about 500 K) is lower than that of structural change (about 650 K). Both the shape and the internal structure remain almost unchanged from about 700 K to about 1140 K. At about 1140 K, both the radius of gyration and the bond order parameters change quickly towards the values corresponding to a liquid drop, showing that the cluster is melting.

The above results indicate that continuous heating induces the gold nanorod to go through two distinct transformations: (1) a shape transformation, in which the initial rod shrinks to the shorter and wider intermediate state with an aspect ratio of ~ 1.8 and (2) the melting transition. The shape change is accompanied by a structural change of the interior atoms of the gold nanorod.

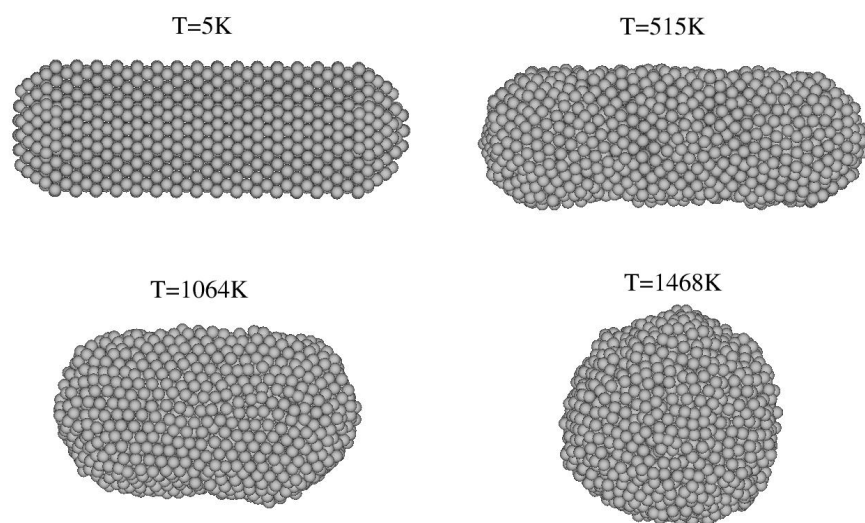


Fig. 5.2: Snapshots from a continuous heating run of a gold nanorod with 2624 atoms at temperatures of 5, 515, 1064, and 1468 K.

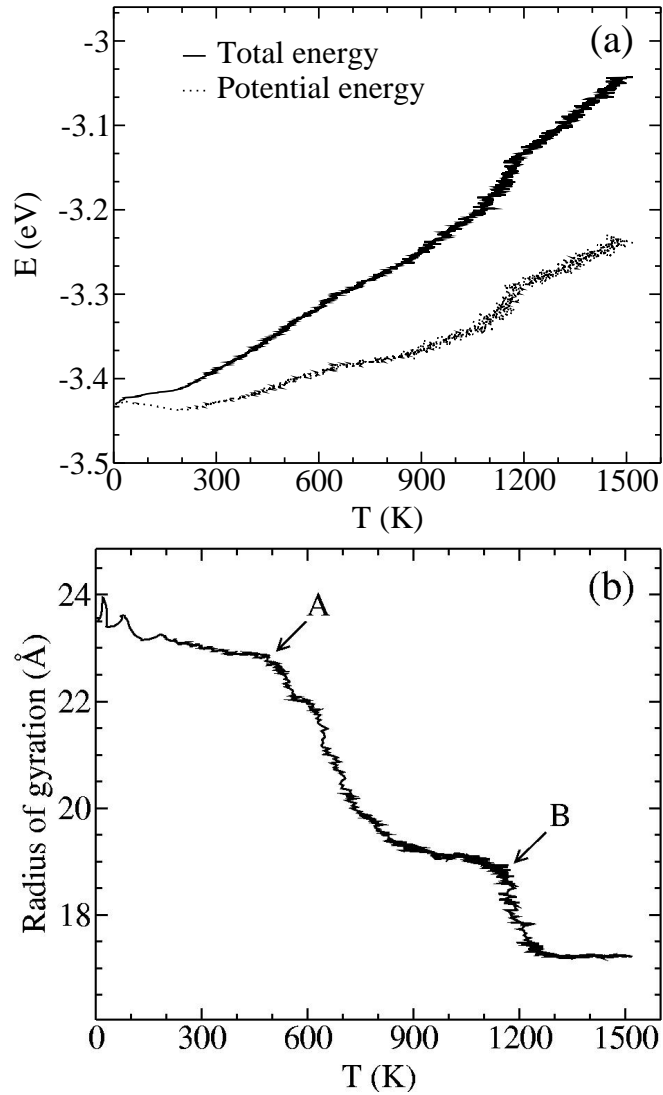


Fig. 5.3: Temperature dependence of (a) total and potential energy and (b) the radius of gyration for the $N = 2624$ atom rod during continuous heating with a heating rate of 7×10^{12} K/s. The letter A indicates the onset of the shape transformation and the letter B indicates the onset of the melting transition.

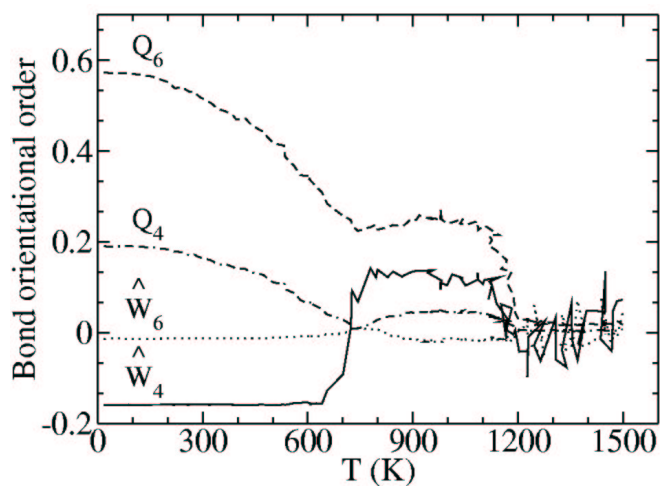


Fig. 5.4: Temperature dependence of bond order parameters averaged over the internal atoms for the gold nanorod with 2624 atoms during continuous heating with a heating rate of 7×10^{12} K/s.

The same simulation has been repeated with a heating rate three times higher (2.1×10^{13} K/s, Fig. 5.5) and three times lower (2.3×10^{12} K/s, Fig. 5.6). The intermediate-state phenomenon occurred in both simulations, but with some differences in the details. The most significant difference is that the internal structure of the intermediate state during the slower heating returns to an fcc-dominated structure after a short jump to hcp-dominated, rather than remaining hcp-dominated (as was the case for the faster heatings). Thus, the occurrence of a shape transformation and the appearance of intermediate stable states appear to be qualitatively independent of the heating rate, but changes in the internal structure have a pronounced heating rate dependence. We will return to this point in Chapter 6 when we describe quasi-equilibrium heating of the nanorods.

Analogous computer simulations were also performed for gold nanorods with the same initial shape but different sizes of 1404, 2094, 3610, 4960, 5870, 7552, 9678 and 11 076 atoms. In Figs. 5.7 and 5.8 we show the radius of gyration and bond order parameters for $N = 7552$ and $N = 11\,076$ atoms, respectively. Essentially the same phenomenology was observed in all of the simulations and the aspect ratio of the intermediate nanorods are all very close to 1.8. However, like for the case of different heating rates, the internal structures of the intermediate states range from hcp-dominated to fcc-dominated with different hcp/fcc ratios.

It is well known that the melting temperature T_m of gold nanoclusters decreases with cluster size. Our simulations indicate that the onset of the shape transformation, T_s , has a strong size dependence as well. The instantaneous temperatures of the onsets of the shape transformation and the melting transition, T_s and T_m , (corresponding to points A and B in Fig. 5.3b) are shown in Fig. 5.9. These temperatures were determined by visual inspection of the radius of gyration and bond order parameters vs. temperature curves. Both the onset of the shape transformation and of the melting transition increase with increasing sizes, but that of the melting transition increases more slowly.

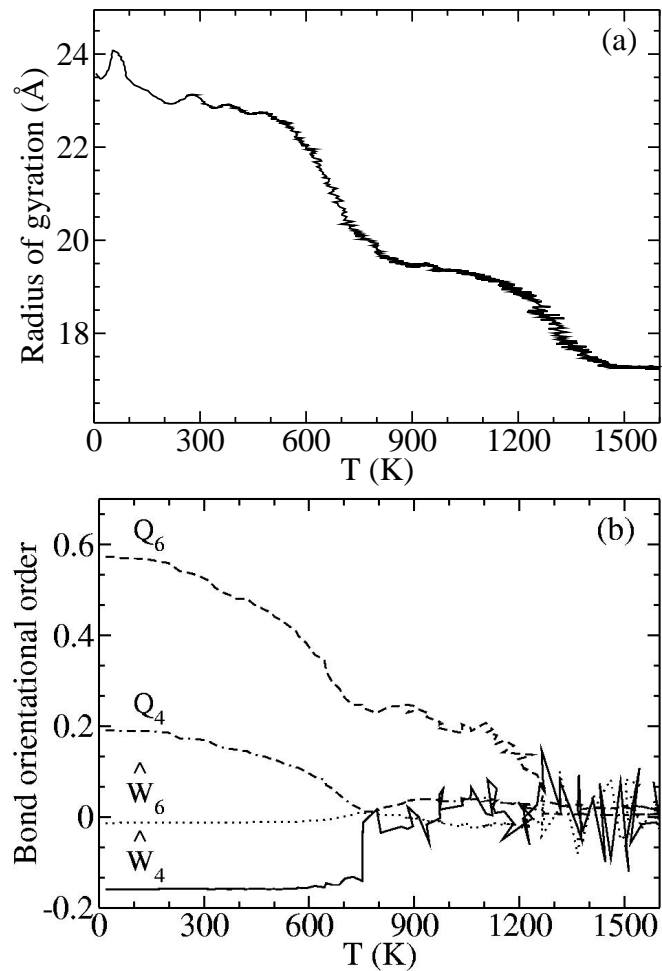


Fig. 5.5: Temperature dependence of (a) the radius of gyration and (b) the average bond order parameters for internal atoms, for the $N = 2624$ atom rod during continuous heating with a rate of 2.1×10^{13} K/s.

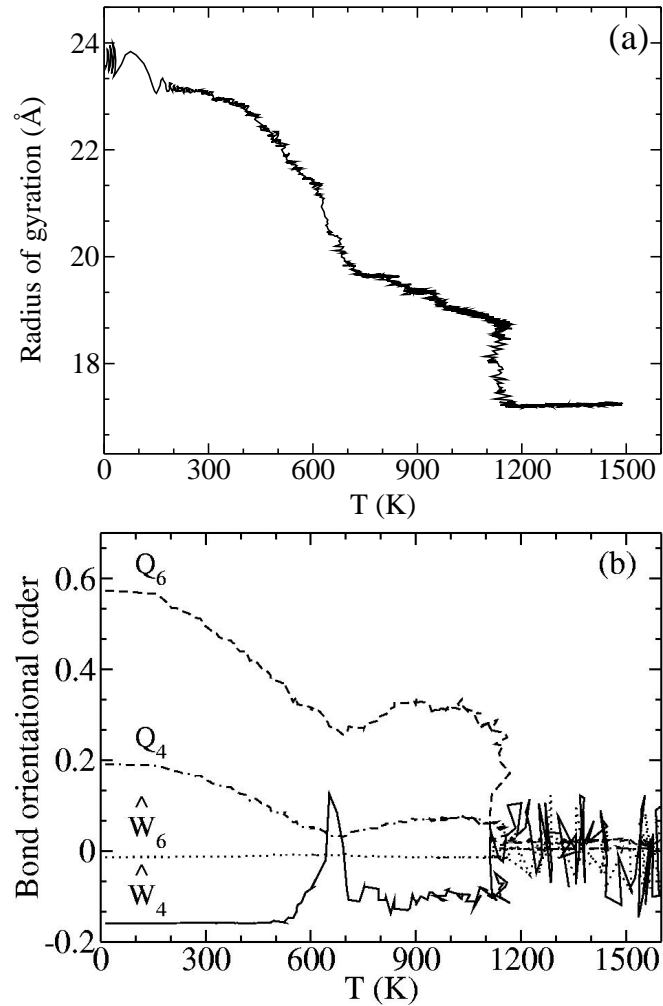


Fig. 5.6: Temperature dependence of (a) the radius of gyration and (b) the average bond order parameters for internal atoms, for the $N = 2624$ atom rod during continuous heating with a rate of 2.3×10^{12} K/s.

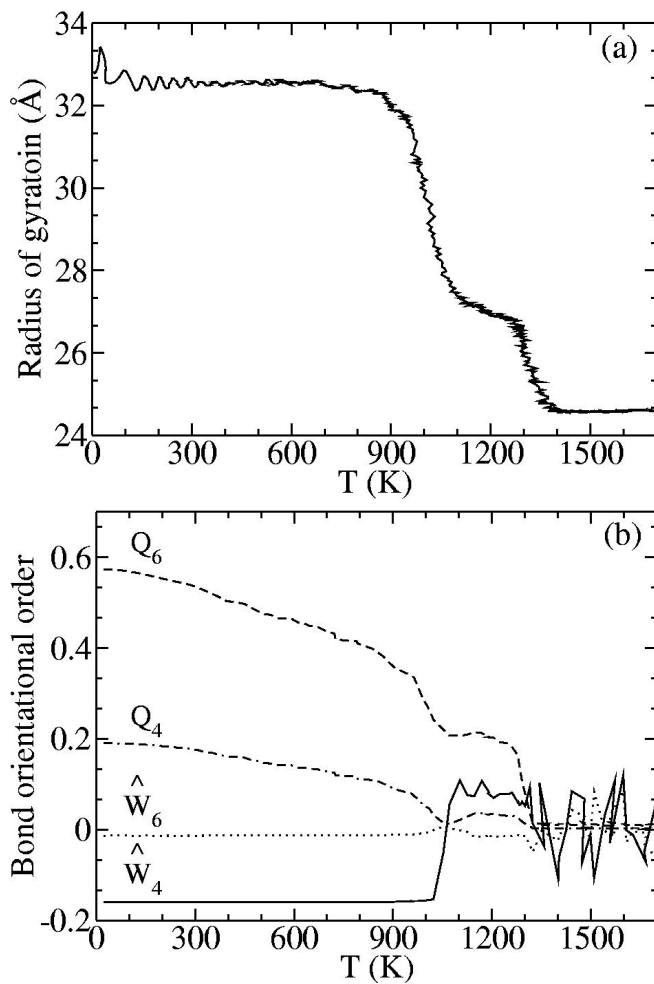


Fig. 5.7: Temperature dependence of (a) the radius of gyration and (b) the average bond order parameters for internal atoms, for the $N = 7552$ atom rod during continuous heating with a rate of 7×10^{12} K/s.

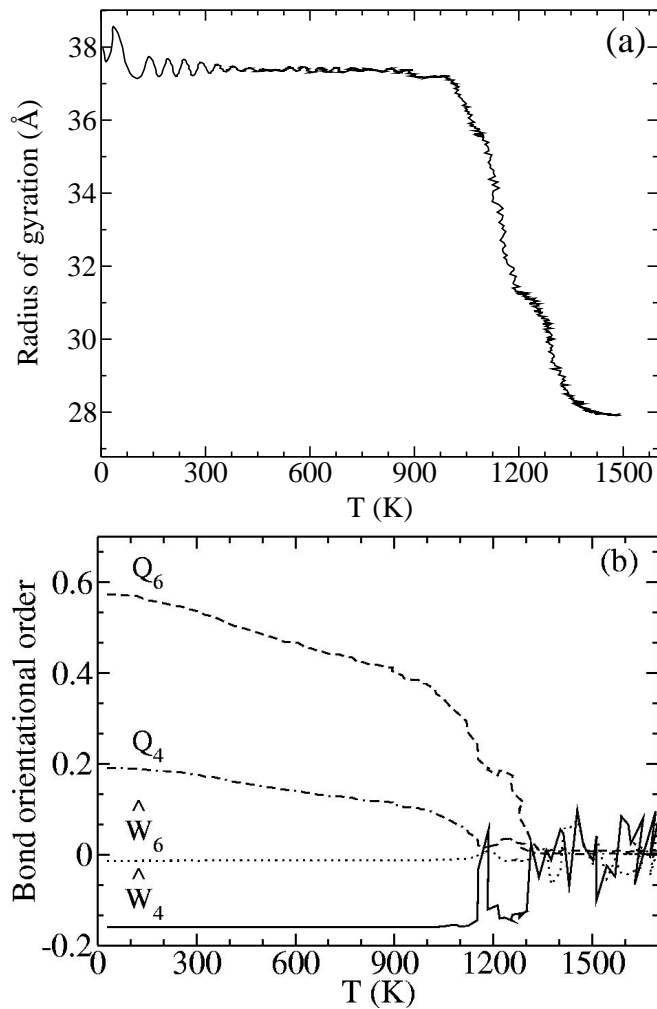


Fig. 5.8: Temperature dependence of (a) the radius of gyration and (b) the average bond order parameters for internal atoms, for the $N = 11076$ atom rod during continuous heating with a rate of 7×10^{12} K/s.

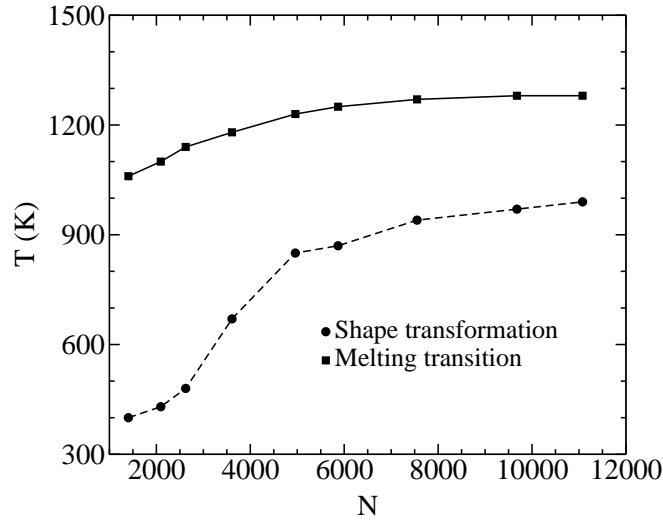


Fig. 5.9: The temperatures of the onsets of the shape transformation (T_s) and melting transition (T_m) for gold nanorods of various sizes. These temperatures were determined by visual inspection of the R_g vs. T curves as indicated by the arrows A and B in Fig. 5.3b.

5.3 Intermediate State

For the gold nanorod with $N = 2624$ atoms, the intermediate state appears to be stable on the simulated time scale for temperatures up to 1140 K. We have verified this (meta)stability by equilibrium simulation. Several configurations of the intermediate state at different instantaneous temperatures upon continuous heating were saved, and then simulated further using a microcanonical constant energy MD. Configurations at 743, 905, and 1033 K were found to be stable for more than 400 ps. However, we cannot exclude the possibility that the intermediate state would undergo a transformation to a more spherical shape after a much longer simulated time. Particularly at high temperatures, curvature driven surface diffusion provides a mechanism for such a transformation [76]. This stability of the intermediate state will be further studied and discussed in Chapter 6, where we use a quasi-equilibrium MD procedure.

Tab. 5.1: *Aspect ratios of the intermediate states.*

Number of atoms	Initial aspect ratio	Intermediate aspect ratio
3610	3.0	1.8
3900	4.1	2.5
3810	5.0	2.8
3686	6.0	4.2

We found the aspect ratio of the intermediate state to be 1.8 for all rods with different sizes but an identical initial aspect ratio of 3.0. This raises the question of whether an aspect ratio of 1.8 is universal for nanorods which undergo the shape transformation. To answer this question, we have also carried simulations of nanorods consisting of 3900, 3810, and 3686 particles with initial aspect ratios of 4.1, 5.0, and 6.0, respectively. Different aspect ratios of the intermediate state have been found as listed in Table 5.1, suggesting that the shape (aspect ratio) is not sufficient to characterize the stable intermediate state completely.

5.4 Local Structure Analysis

In order to understand the mechanism for the shape transformation during heating, we carry out an analysis of the local crystal structure for the gold nanorod with 2624 atoms. From the globally averaged bond order parameters of the internal atoms shown in Fig. 5.4, we already know that the structure changes from fcc-dominated to hcp-dominated. We therefore concentrate on the analysis of fcc and hcp local structures and proceeded as follows. During heating, instantaneous configurations have been periodically saved. We then use a conjugate gradient method [94] to relax all the atoms to their local potential energy minimum, to eliminate thermal vibration noise in the crystal structure. For each such relaxed configuration, local bond order parameters have been calculated for each internal atom, as we have done

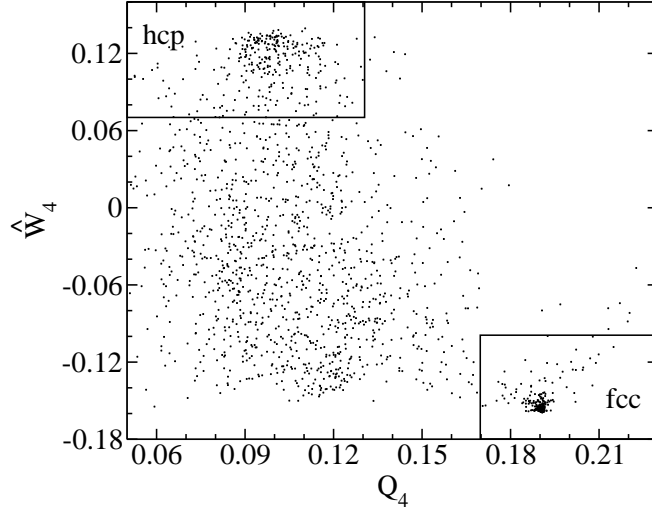


Fig. 5.10: Order parameters Q_4 and \hat{W}_4 for internal atoms in a set of structures of the 2624-atom gold nanorod at $T = 691$ K. The atoms with $Q_4 < 0.13$ and $\hat{W}_4 > 0.07$ are considered atoms with local hcp structure. Those with $Q_4 > 0.17$ and $\hat{W}_4 < -0.10$ are atoms with local fcc structure.

previously for the Ih cluster in Section 4.1 (see Fig. 4.1b). The surface atoms are identified and excluded from this structure analysis, because they do not have a full three dimensional local structure.

Bond order parameters characteristic for the rod at 691 K, in the intermediate state, are displayed in Fig. 5.10 as a density plot of \hat{W}_4 vs. Q_4 . The surface atoms have been excluded from this plot. We see that the data cluster primarily in two regions, which we identify as local fcc and hcp structures. Most atoms in the interior of the rod are found to have fcc (bottom right corner) or hcp (top left corner) local structures. Other atoms represented by data scattered elsewhere in the \hat{W}_4 vs. Q_4 plane, are found to lie near the surface, and are labeled as having “other” local structure.

The fractions of surface atoms and atoms with fcc, hcp and “other” structures are shown in Fig. 5.11 as a function of temperature. Because the aspect ratio of the rod decreases with increasing temperature, and rods with smaller aspect ratio

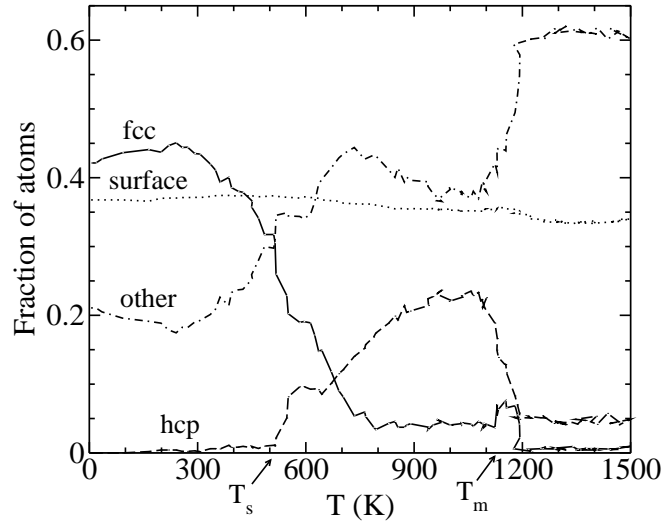


Fig. 5.11: Fractions of surface atoms and internal atoms with fcc, hcp, and “other” local structures vs. temperature for the gold nanorod with 2624 atoms.

have smaller surface area, the fraction of surface atoms decreases very slowly with increasing temperature. For temperatures below 300 K, the fractions keep almost unchanged. For temperatures above 300 K and below the shape transformation temperature $T_s \sim 500$ K, the population of hcp-atoms remains very small, but the population of fcc-atoms decreases due to the growth of “other” structure atoms. At about 500 K, the population of hcp-atoms jumps to a higher value and keeps growing until at the end of the shape transformation (~ 800 K). In the intermediate state region, the population of all kinds of atoms keeps almost constant. At near the onset of the melting transition (~ 1140 K), the populations of fcc-atoms has a small but noticeable increase. The fractions of both fcc and hcp atoms decrease quickly to near zero at ~ 1250 K, when the nanorod is completely melted and the system is unstructured.

In Fig. 5.12 we show cross sections of configurations of the nanorod with $N = 2624$ atoms at different temperatures with atoms colored according to their local structures. Below the shape transformation (~ 500 K) the nanorod consists almost entirely of fcc-atoms (yellow) with some atoms at the surface (gray). With increasing

temperature the number of atoms with “other” structure grows, but the structure in the interior remains of fcc type. At a temperature of 517 K, there appear some hcp atoms along the $\langle 111 \rangle$ direction of the initial crystal orientation. At 551 K, there are three groups of hcp atoms along three different $\langle 111 \rangle$ directions across the fcc body. With increasing temperature, the number of hcp-atoms in these three groups keeps growing. At the same time, the number of “other” structure atoms increases (691 K). At 794 K, only three layers of fcc are left along the long axis of the rod at the top, the bottom and in middle of the hcp body. It is interesting to note that the surface of the nanorod at this temperature appears to be more ordered than at lower temperatures, and the crystal orientation now changes. At 1088 K there is only a middle layer of fcc along the long axis of the rod besides several solitary fcc atoms. At 1156 K, the number of fcc-atoms increases again and the whole body is more ordered with an increasing number of hcp-atoms. At a slightly higher temperature of 1193 K, melting sets in and the cluster becomes completely disordered and spherical at 1305 K. The two configurations at 1180 K and 1192 K suggest that the melting propagates quickly from the outside to the inside of the gold nanorod.

In order to gain a better understanding of the type of movement of the atoms leading to the shape change, we have determined a vector field shown in Fig. 5.13. Each vector connects the position of an atom when the shape transformation just starts to occur (511 K) to the position of the same atom after completion of the shape transformation (794 K). It is evident that surface atoms originating in the end caps move towards the center and that surface atoms at the middle move radially away from the rod axis. While the center atoms move little, other internal atoms slide along the rod axis towards the center. This flow pattern is consistent with formation of the ϕ -shaped particles observed experimentally [28, 29]. However, we never detected such ϕ -shaped particles in our simulation. This might be due to the large size differences between our simulated nanoparticles and the ones studied in experiments.

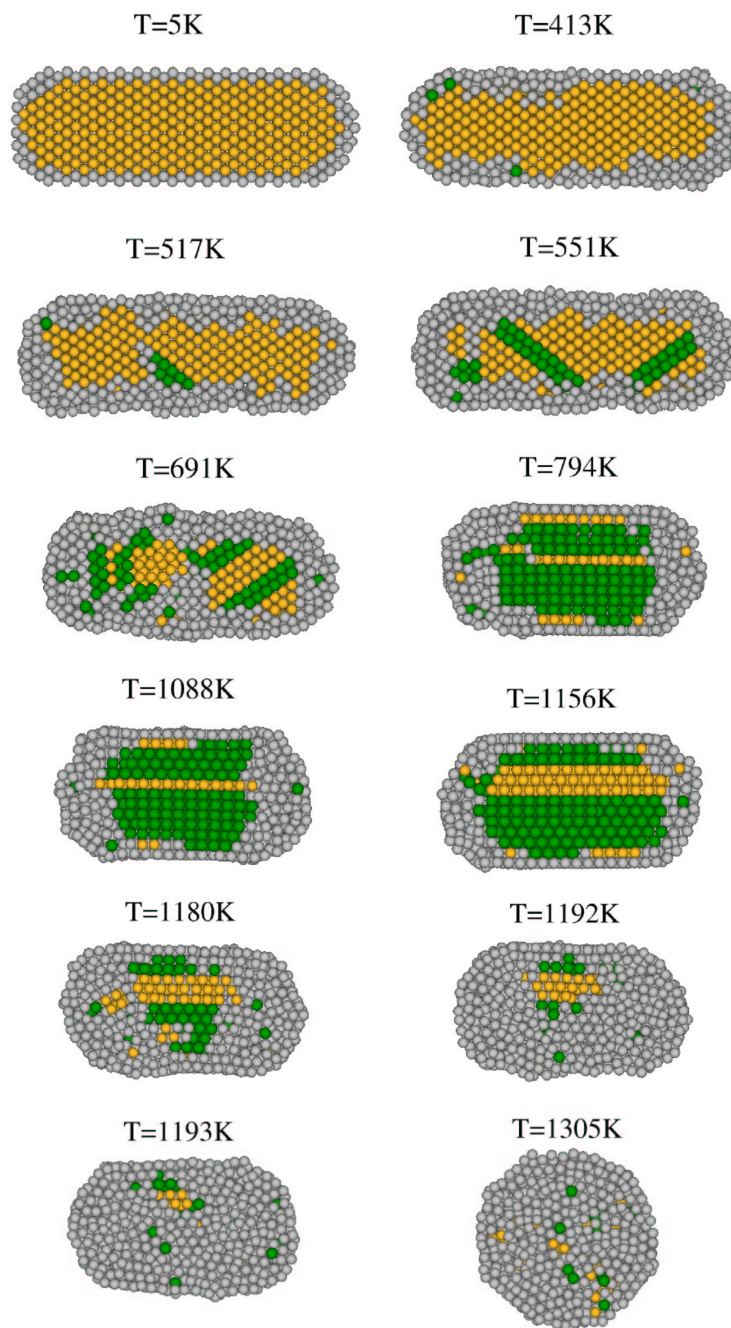


Fig. 5.12: Cross sections of the $N = 2624$ atom gold nanorod at different temperatures with atoms colored according to their local structure: fcc is yellow, hcp is green, and “other” is gray.

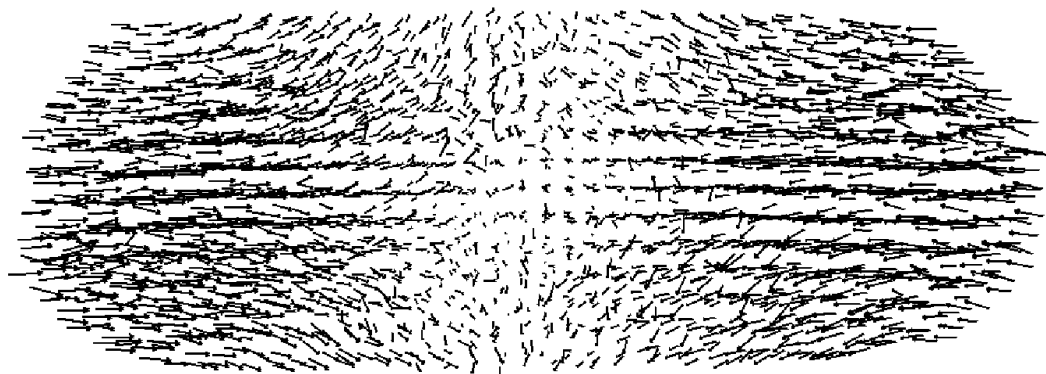


Fig. 5.13: Motion of atoms during the shape transformation. The initial configuration is at 511 K and the final configuration is at 794 K.

5.5 Discussion and Conclusions

Summarizing the above simulation results, two main transformations occur during continuous heating of gold nanorods: a shape transformation and a melting transition. The shape change is accompanied by a structural change. The exact aspect ratio and the structure of the intermediate state depend on rod size, heating rate and initial aspect ratio.

From the simulation results discussed above the following phenomenological picture for the morphological and structural changes emerges. Initially, at very low temperature (5 K in our case), the gold nanorod has a defect-free fcc body by construction. During the heating towards the onset of the shape transformation, the surface atoms display increasing deviations from their original positions. This not only leads to more irregularly arranged surface atoms, but also helps the atoms beneath the surface to leave their original fcc positions (see Fig. 5.12, $T = 511$ K). With increasing temperature, more and more atoms beneath the surface deviate from the local fcc structure so that the number of fcc atoms decreases (see Fig. 5.11).

It might be this build up of the atoms with “other” structures which eventually drives the nanorod through the morphological transformation to a shorter rod with smaller surface area. When this happens, planes of atoms slide with respect to each

other transforming fcc-atoms into hcp-atoms and vice versa. Such sliding events can happen independently at several different positions and in different directions (see Fig. 5.12, $T = 517$ K and $T = 551$ K). The resulting configurations are consistent with the experimentally observed planar defects inside the rods produced by laser heating [30].

During the shape transformation, the nanorod becomes shorter and wider. At the same time, the internal structure keeps changing from fcc-dominated to hcp-dominated (see Fig. 5.12, $T = 691$ K). In the case of $N = 2624$ atoms, the shape transformation stops when the body is of almost pure hcp structure (see Fig. 5.12, $T = 794$ K). In clusters of different size or with different heating rates, however, the shape transformation can produce intermediate states with fcc-dominated structure. The heating rate, the size and the initial aspect ratio all affect the shape and structure of the intermediate state as well. The intermediate state is stable within a certain range of temperatures (see Fig. 5.12, $T = 1088$ K, the range is shorter in the case of Fig. 5.6) and corresponds to the shorter and wider gold nanorods found in experiments [28, 29].

As the temperature keeps increasing, more atoms with “other” structures reorganize to be fcc or hcp, and more fcc layers transform from hcp (see Fig. 5.12, $T = 1156$ K). As the cluster reaches the melting temperature, both the surface and internal atoms become unstructured (see Fig. 5.12, $T = 1193$ K) and the cluster quickly collapses to a liquid nanosphere (see Fig. 5.12, $T = 1305$ K).

Although the continuous heating scenario is consistent with the experiments, it is a kinetic rather than a thermodynamical procedure. Only instantaneous properties can be obtained, and the continuous increase of total energy drives the simulated nanorods to be in nonequilibrium states all the time. In order to gain a clearer understanding of the behavior of nanorods upon heating, in Chapter 6 we will use a quasi-equilibrium MD procedure to reinvestigate the shape transformation of gold nanorods. As we will see, some of the phenomenological conclusions presented here

will remain, but we will arrive at a deeper physical understanding of what is driving the transformations of the nanorod.

6. QUASI-EQUILIBRIUM HEATING OF GOLD NANORODS

In order to obtain a deeper physical understanding of the phenomena we have observed in the continuous heating of gold nanorods, in this chapter we use “quasi-equilibrium” heating MD to reinvestigate the shape transformation of gold nanorods. We only report on the rod with $N = 2624$ atoms. The results will be compared with those for the continuous heating MD simulation in Chapter 5, and those for the Ih gold cluster with the same size in Chapter 4. Unless otherwise stated, when we refer to the continuous heating simulation, we are referring to the case with a heating rate of 7×10^{12} K/s.

This chapter is arranged as follows. First we will show, by the radius of gyration, bond order parameters for the internal atoms, and the caloric curve, that the quasi-equilibrium heating is equivalent to a continuous heating method with a much slower heating rate. Because we believe that the surface plays an important role in the shape transformation of gold nanorods, we will then study the surface behavior by computing the average shape of the sides and the surface bond curvature distributions. The snapshots of instantaneous configurations will be given to help understand how the interior changes simultaneously with the surface. We will find that the shape transformation is driven by the preference of the nanorod to restructure itself so that, like the Ih cluster, its surface consists of stable $\{111\}$ facets. Finally we will clarify that no atomic diffusion is involved in the transformation.

6.1 Quasi-equilibrium Heating

We construct the $N = 2624$ atom gold nanorod with an aspect ratio of 3.0 at low temperature exactly as was done in Chapter 5 (see Fig. 2.13). We then heat the rod temperature by temperature using constant temperature MD, similar to what has been done for Ih gold clusters in Chapter 4. The constructed gold nanorods are first relaxed at 5 K, then heated up from 100 K to 1300 K, well above T_m , with temperature intervals of 100 K. The intervals are reduced to 10 K near T_m . At each temperature the nanorod goes through constant temperature MD for 10^7 steps (43 ns). Note that the true *equilibrium* shape of the nanorod would not be rod-like at all, but would be a more spherical shape with an aspect ratio ~ 1 , such as the Ih clusters of Chapter 4. However, relaxation of the global shape to such a true equilibrium shape requires much longer times than we simulate. Here we are interested instead in how the rod relaxes its shape over long but finite times. The procedure of relaxation is more important to us than the true equilibrium properties at a certain temperature. Thus we denote the present simulations as a “quasi-equilibrium” heating procedure. Using such a quasi-equilibrium heating will allow us to compute averages over physical quantities at fixed temperatures, while allowing the rod to relax to locally preferred structures, thus allowing us to see what instabilities drive the shape transformation seen in Chapter 5.

In Fig. 6.1 we plot the radius of gyration (described in Section 3.4) vs. temperature. The quasi-equilibrium heating is shown as the lower curve. The upper curve shows, for comparison, our earlier results for the continuous heating of Chapter 5 (see Fig. 5.3b). Note that the continuous heating curve is a plot of the instantaneous radius of gyration vs. the *instantaneous* temperatures all the way through the whole curve. However, the values plotted for the quasi-equilibrium curve are grouped into bins representing 12 fixed temperatures. The temperatures of two adjacent bins have a difference of 100 K. Within each bin the temperature is held constant to the leftmost (smallest) value, and the plotted curve shows the radius of gyration as it

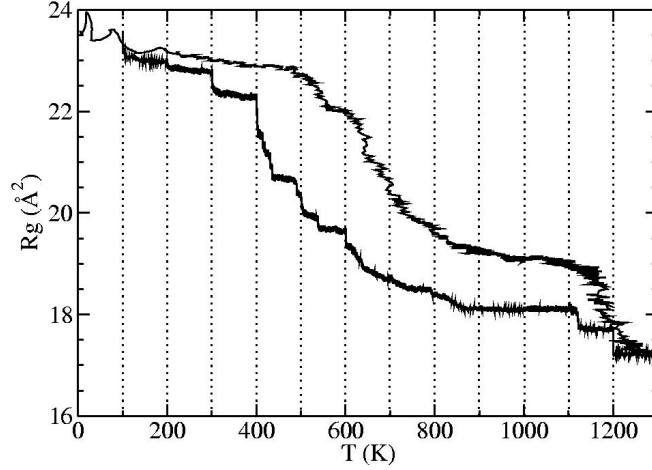


Fig. 6.1: Radius of gyration for the quasi-equilibrium heating (lower curve). Dotted vertical lines represent constant temperature bins. The values in each bin are the time evolution of radius of gyration through a constant temperature MD at a fixed temperature given by the leftmost (smallest) temperature of the bin. For comparison, the upper curve is the radius of gyration for the continuous heating of the same rod (the same curve in Fig. 5.3b).

evolves in time at the *fixed* temperature. We plot it in this way to illustrate that the cluster continues to relax its shape over the time scale of our simulation, even when the temperature is held constant. The two curves in Fig. 6.1 have roughly equal values both at very low temperature (~ 100 K) and at high temperature in the liquid (~ 1200 K). In between, the radius of gyration for the quasi-equilibrium heating is systematically lower than that for the continuous heating, indicating that the former procedure facilitates the relaxation of the rod to a shorter and wider shape at each temperature. The onset shape transformation temperature for the quasi-equilibrium heating is $T_s \simeq 400$ K, substantially lower than that for the continuous heating (~ 500 K). In both cases the shape change stops at about 900 K, and the melting transition happens between 1100 K and 1200 K.

In Fig. 6.2 we show the bond order parameters, averaged over all the internal atoms, during the quasi-equilibrium heating. Here the internal atoms are defined as

those atoms not on the surface of the rod, where the surface atoms are determined by the cone algorithm described in Section 3.5.1. Again the values are grouped into constant temperature bins as was done for the radius of gyration in Fig. 6.1. By considering \hat{W}_4 in particular, and comparing to the values given in Table 3.1, we see that the internal structure remains almost pure fcc up to almost $T_s \simeq 400$ K, then jumps quickly to an hcp-dominated structure, and remains so until roughly 600 K. From 600 K to 700 K, the bond parameters take values between those of the fcc and hcp structures. At 800 K, the interior of the rod changes back to fcc-dominated, and stays so up until the bulk melting T_m . At 1200 K, above T_m , all four parameters oscillate around 0, indicating a liquid state. Comparing with the plots of Chapter 5 for different continuous heating rates, Figs. 5.4, 5.5b, and 5.6b, it is clear that the internal structure for the quasi-equilibrium heating evolves in a way more like that for our slowest continuous heating rate of Fig. 5.6b; the internal structure changes back to fcc-dominated, rather than staying hcp-dominated, before melting.

In Fig. 6.3 we show the caloric curve (average potential energy per atom vs. temperature) of the quasi-equilibrium heating of the rod with $N = 2624$ atoms (solid circles) as compared to that of continuous heating (dotted line) and the equilibrium heating of the Ih cluster (open circles). We see that from 100 K to 300 K the plot grows almost linearly, showing that thermal expansion is the dominating phenomenon. The potential energy remains unchanged at 400 and 500 K, corresponding to the shape transformation regions indicated by the radius of gyration (see Fig. 6.1) and the internal bond order parameters (see Fig. 6.2). Then it increases linearly from 600 K to 800 K, corresponding to the slower transformation regions seen in the radius of gyration and the internal bond order parameters. Just below T_m the linear increase is with a faster rate, corresponding to the thermal expansion of the intermediate state, as indicated by the plateaus in the plots of the radius of gyration and the internal bond order parameters. The rod melts at $T_m \simeq 1120$ K, after equilibration for about 20 ns.

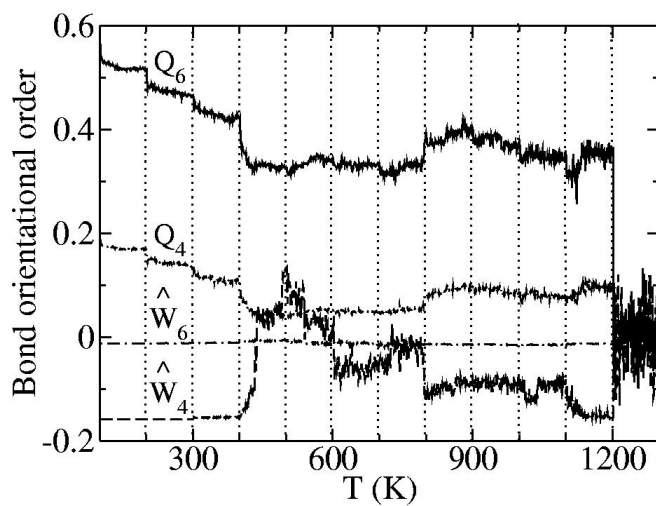


Fig. 6.2: Bond orientational order parameters for the internal atoms. Dotted vertical lines represent constant temperature bins. The values in each bin are the time evolution of radius of gyration through a constant temperature MD at a fixed temperature given by the leftmost (smallest) temperature of the bin.

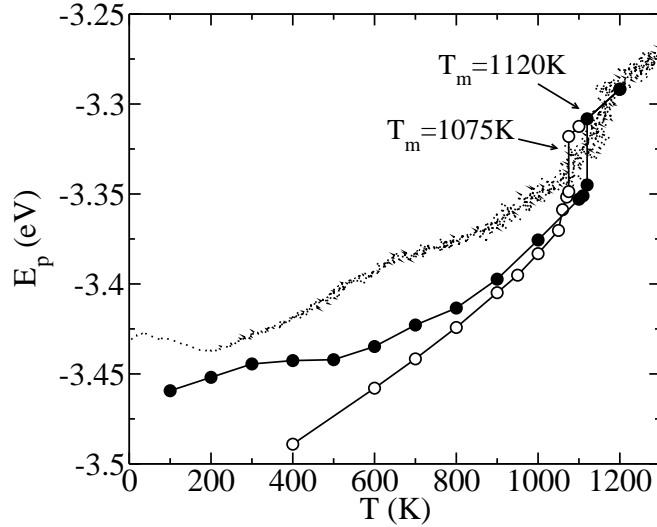


Fig. 6.3: Caloric curves for quasi-equilibrium heating (closed circles) and continuous heating (dotted line) of the gold nanorod with $N = 2624$ atoms, and for the equilibrium simulations of the Ih gold cluster with $N = 2624$ atoms (open circles).

Because the rod is better relaxed by the quasi-equilibrium heating than by the continuous heating, the potential energy of the former is systematically lower than the latter. The melting temperature during continuous heating (~ 1140 K) is close to that during quasi-equilibrium heating (~ 1120 K), but the melting during continuous heating is smeared out to form a melting “zone” ending at about 1180 K. On the other hand, the potential energy of the Ih cluster is systematically lower than the rod, due mainly to the larger surface area of the rod. Above 800 K, the potential energy for the quasi-equilibrium heating of the rod is very close to that for the Ih cluster, and the two curves are roughly parallel to each other. Note that although the potential energy of the rod is still slightly higher than for the Ih cluster, the rod melts at a somewhat higher temperature (~ 1120 K) than the cluster (~ 1075 K). This indicates that, in our limited simulation time, the intermediate state of the gold nanorod is more stable than the Ih gold cluster, despite the fact that the former has a higher potential energy than the latter. This might be due to a larger superheating

hysteresis associated with the melting of the intermediate rod. However, because the average potential energy of the rod is higher than the Ih cluster, we expect, in the limit of *true* equilibrium, that the rod will melt at a lower temperature than the Ih cluster, or that the rod will go through a solid-to-solid transition to become an Ih cluster below the melting T_m . We will make this point clearer after our investigation of the intermediate state of the rod in the following sections.

From these three plots we see that the quasi-equilibrium heating procedure is qualitatively equivalent to the continuous heating with a very slow heating rate. Our quasi-equilibrium heating procedure takes a simulated time of 387 ns to heat the rod from 300 K to 1200 K $> T_m$, about a thousand times longer than for the continuous heating procedure of Chapter 5 (around 280 ps). We now find that the onset temperature of the shape transformation is $T_s \simeq 400$ K, and that the intermediate state remains essentially unchanged between 900 and 1000 K. The rod becomes a little shorter and wider at 1100 K below $T_m \simeq 1120$ K. Thus, for the length of our simulation time, the intermediate state appears to be stable and relatively well equilibrated.

6.2 Intermediate State and Random Stacking

Before we investigate how the gold nanorod restructures itself from its initial configuration to the higher temperature stable intermediate state, we illustrate just how different the intermediate state is from the initial one. In Fig. 6.4a we show the surface atoms of the rod with $N = 2624$ atoms, as it is initially constructed before any thermal relaxation, according to the model shown in Fig. 2.13b. We define a coordinate system fixed on the rod, with the long axis of the rod along the \hat{z} axis, as shown in the figure. We show two views of the surface: looking sideways at the rod along the \hat{x} axis (left picture), and looking down the length of the rod along the \hat{z} axis (right picture). To identify the local structure of the atoms on the surface, we have computed the 2D bond order parameters for each surface atom, and set criteria

for determining different local surface structures. According to the closeness to the values given in Table 3.1, we chose the criteria: gold $\{111\}$ if $0.7 < Q_6 < 0.9$ and $-0.08 < \hat{W}_6 < -0.02$; gold $\{100\}$ if $Q_6 < 0.7$ and $\hat{W}_6 > -0.02$; and gold $\{110\}$ if $Q_6 > 0.9$ and $\hat{W}_6 < -0.08$. The surface atoms are then colored accordingly: gold $\{111\}$ is yellow, gold $\{100\}$ is green, gold $\{110\}$ is red, and “other” is gray. Note that here the bond parameter values correspond to the structure of the atoms at the center of perfect gold surface planes as shown in Fig. 2.2. Thus the edge atoms connecting planes of different orientations are easily identified as having “other” local surface structure. From these pictures we see that the initial constructed rod has four elongated $\{100\}$ facets and four elongated $\{110\}$ facets on the long sides, and four small $\{111\}$ facets, four small $\{110\}$ facets, and one small $\{100\}$ facet on each end cap. Comparing the colored surface with the theoretical model shown in Fig. 2.13b, we see that our criteria and coloring method work well with the rod.

We now consider similar pictures for the intermediate state at higher temperature. We pick a configuration sampled in the middle of the run at $T = 900$ K, and quench the local thermal fluctuations by the conjugate gradient method [94]. As we will show in Section 6.4 all the layers have a similar shell structure, but the surface and first sub layers exhibit some distortion due to surface reconstruction. In Fig. 6.4b we therefore show the second sub layer of the configuration to represent the surface (shell) structure of the intermediate state (we used a similar approach in Fig. 4.1 for the Ih cluster). Again the atoms are colored according to their 2D local structure. We see that now there are only four elongated gold $\{111\}$ facets on the long sides (left picture). Each end cap (right picture) has two small $\{111\}$ and two small $\{100\}$ facets. We thus can make one of our main conclusions: the transformation to the intermediate state is driven by the preference of the rod to replace its less stable $\{100\}$ and $\{110\}$ surfaces by much more highly stable $\{111\}$ surfaces.

Next we consider the 3D structure of the interior of the intermediate state. In Fig. 6.5a we show the cross section in the y - z plane of the constructed rod as shown

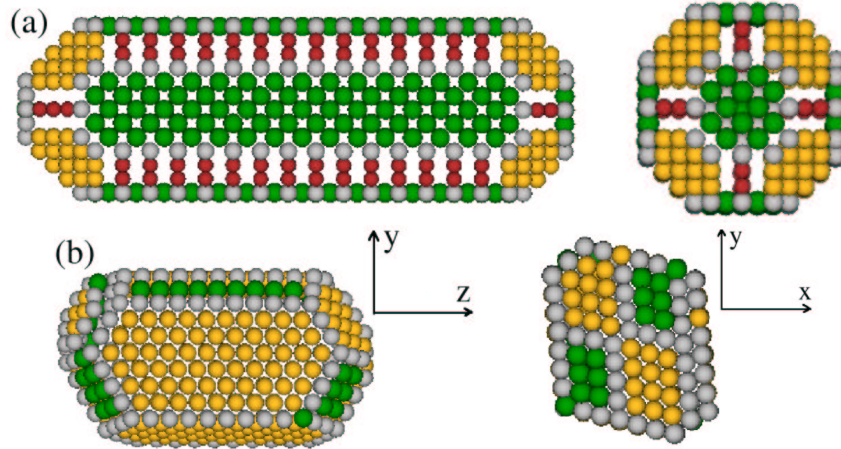


Fig. 6.4: (a) The surface of the constructed gold nanorod. (b) The second sub layer of a configuration in the intermediate state at $T = 900$ K. The atoms are colored by their 2D local surface structure: $\{111\}$ is yellow, $\{100\}$ is green, $\{110\}$ is red, and “other” is gray.

in Fig. 6.4a. In Fig. 6.5b we show the cross section of the same configuration of the intermediate state as shown in Fig. 6.4b. Local 3D bond order parameters have been calculated for each internal atom. The atoms are then colored according to their 3D local structure, as we have done for the Ih cluster in Section 4.1 and for the continuous heating in Section 5.4: fcc is yellow, hcp is green, and “other” is gray. Note that the coloring here is meaningless for the surface atoms, since these atoms lack the 3D environment of the internal atoms.

From Fig. 6.5 we see that both the initial constructed rod and the intermediate state rod have an almost pure fcc body, however the orientation of this fcc body with respect to the long axis of the rod is different for the two cases! In order to see this, we first give a brief introduction about the fcc (face-centered-cubic), hcp (hexagonal-close-packed), and random stacking structures. We will then show how the gold $\{111\}$ planes are oriented in our gold nanorods.

A bulk fcc crystal can be built up either through the periodic duplication of the cubic unit cell of fcc shown in Fig. 2.1, or through the periodic pile-up of $\{111\}$

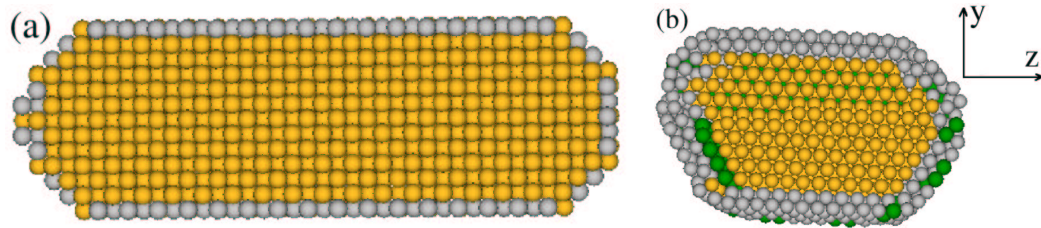


Fig. 6.5: Cross sections of (a) the initial constructed rod and (b) the intermediate state at $T = 900$ K. The atoms are colored by their 3D local structure: fcc is yellow, hcp is green, and “other” is gray.

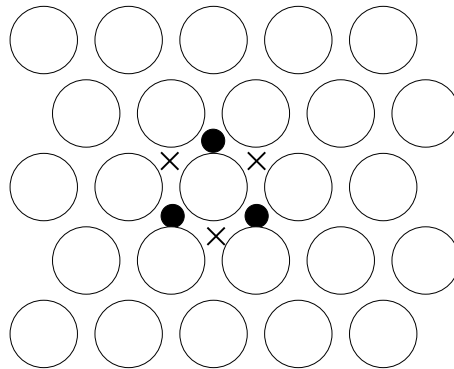


Fig. 6.6: Two possible piling positions of a hexagonal plane represented by solid circles and crosses, respectively.

surfaces, such as shown in Fig. 2.2c. A $\{111\}$ surface is actually a 2D hexagonal planar lattice, in which the particles are close-packed. To form the closest three dimensional packing, another hexagonal plane can be placed on top of the first in two possible ways. We illustrate these two possibilities by the solid circles and the crosses shown in Fig. 6.6. If the hexagonal planes are piled up periodically alternating between all three positions, i.e. $ABCABC\cdots$, the resulting structure forms an fcc bulk crystal [95]. If they are piled up periodically using only two out of three positions, i.e. $ABABAB\cdots$, the resulting structure forms an hcp bulk crystal [95]. If the planes are piled up randomly, e.g. $ABCBAB\cdots$, they form a “random stacking” bulk.

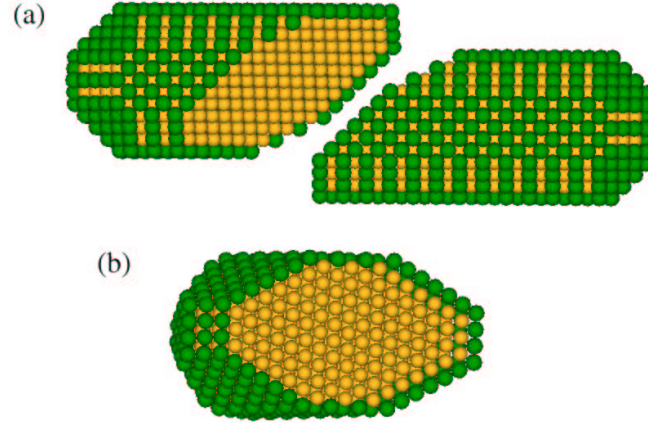


Fig. 6.7: (a) The constructed rod cut along the $[1\bar{1}\bar{1}]$ direction. (b) The cross section of the cut surface. Green atoms lie on the surface of the rod, and yellow atoms lie in the interior.

Now let us see how the hexagonal planes are oriented in our gold nanorods with a pure fcc body. Referring to Figs. 6.4 and 6.5, we have defined coordinates in which the long axis of the rod is the \hat{z} axis, and the \hat{x} and \hat{y} axes are as shown. This laboratory coordinate system is fixed in our simulations, and we define the crystal orientations with respect to this system. For the constructed rod of Figs. 6.4a and 6.5a, the unit cubic cell of the fcc bulk is by construction aligned with this xyz coordinate system. The \hat{z} axis is in the $[100]$ direction of the fcc crystal, and the cross section shown in Fig. 6.5a is just the square gold $\{100\}$ surface as shown in Fig. 2.2b. The hexagonal planes of this fcc bulk thus lie with their normal vectors in the $\hat{x} + \hat{y} + \hat{z}$ direction of the laboratory coordinate system. Coloring surface atoms green, and interior atoms yellow, we show in Fig. 6.7a a cut through the constructed rod of Fig. 6.5a with normal in the $\hat{x} + \hat{y} + \hat{z}$ direction, illustrating the hexagonal planar structure of the resulting cross section in Fig. 6.7b.

In contrast to the constructed rod that we start with at low temperature, the intermediate state at 900 K, shown in Figs. 6.4b and 6.5b, has the hexagonal planes of its fcc bulk oriented with their normal in the \hat{x} direction. The cross section in

the y - z plane shown in Fig. 6.5b clearly shows these hexagonal planes. Thus for the intermediate state, the $[111]$ direction of the fcc unit cell is aligned with the \hat{x} axis of the laboratory coordinate system, and the long \hat{z} axis of the rod is now aligned with the $[10\bar{1}]$ direction of the fcc unit cell.

Thus we see that the shape transformation to the intermediate state involves not only a reconstruction of the rod surface, so as to expose the more stable $\{111\}$ planes, but also a reconstruction of the entire bulk of the rod so as to reorient the crystal axes of the fcc interior to be consistent with the new surface structure.

6.3 Average Cross-Sectional Shape and Surface Curvature

Having identified the nature of the intermediate state, we next look to see how this shape and structural transformation evolves with temperature. Since we believe the surface plays an important role in the shape transformation, we first consider the change of the surface at different temperatures. Similar to our analysis for the gold Ih cluster, we now ask how the average shape of the rod changes as the temperature is increased. Because of the large aspect ratio of the rod, the 4π solid angle division that we used when considering the Ih cluster would give a very nonuniform mesh for computing the average surface position of the rod. Thus we turn to a simpler method which only computes the cross-sectioned average shape of the rod when viewed looking down the long axis of the rod (the \hat{z} axis). At each temperature, 1000 configurations sampled uniformly throughout the simulated time of 43 ns are used. We discard all the atoms forming the end caps of the rod, and then project the remaining surface atoms from all configurations into the x - y plane. The average cross-sectional shape is then obtained by dividing the x - y plane into 100 even polar angles centered at the center of mass of all surface atoms, and averaging the x and y positions for the atoms in each angular division. The computed average shapes at

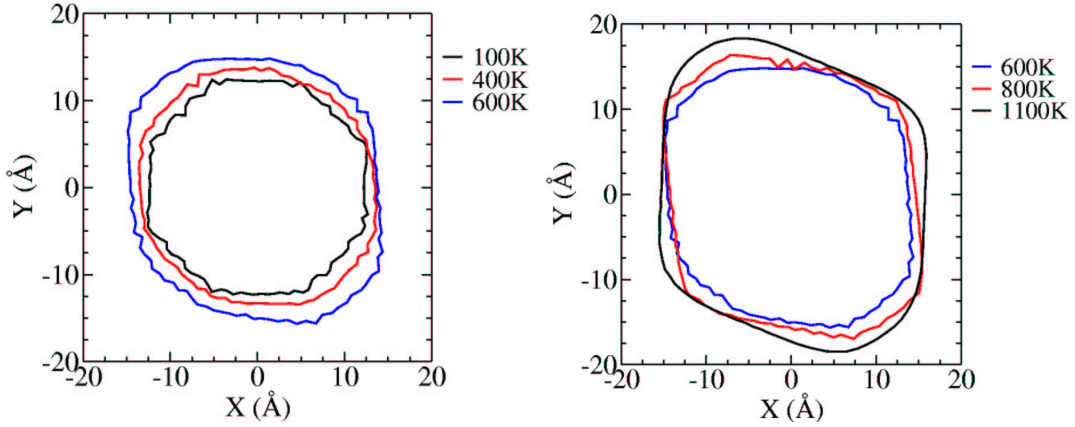


Fig. 6.8: Average cross-sectional shape of the gold nanorod at different temperatures. At each temperature the averaging is over the side atoms of the 1000 configurations sampled in the simulated time of 43 ns.

each temperature are shown in Fig. 6.8. At 100 K, the average cross-sectioned shape has four lines parallel to the x and y axes, corresponding to the four elongated $\{100\}$ facets, and four diagonal lines, corresponding to the four elongated $\{110\}$ facets. At $T_s \simeq 400$ K, where the shape transformation begins, the sides are rounded and bending, showing no facets and a breaking of the initial 4-fold rotational symmetry. At 600 K, The sides nearly parallel to the y axis are flat, showing that facets are forming. At 800 K, the average shape has almost the geometry we have shown in Fig. 6.4b. At 1100 K, the four flat $\{111\}$ facets meet at rounded corners. In the instantaneous configurations, the flat $\{111\}$ facets always meet at sharp edges. However, the positions of the sharp edges fluctuate, so that their average shape is rounded. The perimeter of the average cross-sectional shape keeps growing with increasing temperature, showing that the rod is becoming shorter and wider.

In addition to the average cross-sectional shape, we also use the bond curvature, defined in Section 3.5.2, to further study the flatness of the gold nanorod surface. At each temperature, we calculate the surface bond curvatures, defined by Eq. 3.14, for each instantaneous configuration, as we have done for the gold Ih cluster in Sec-

tion 4.3. In Fig. 6.9 we show the resulting histograms. Unlike the gold Ih cluster (see Fig. 4.11), for which the peaks get broader continuously with increasing temperature, we see that, as the temperature increases, the broad distribution at 400 K sharpens up, with strong low curvature peak and high curvature plateau forming as one makes the shape transformation to the intermediate state. The histograms thus illustrate what is obviously apparent in Fig. 6.8 — as the shape transformation occurs, the surface becomes more ordered with larger flat facets forming.

From the preceding evidence, we can describe the surface evolution upon heating as follows. At 100 K, because the $\{110\}$ and $\{100\}$ facets are less stable, the surface is reorganized from the initial constructed form to be a little rougher. At $T_s \simeq 400$ K, although still with finite surface structure, the surface is now almost as rough as the surface of a liquid drop. Noting that the roughening transition of a macroscopically slab-like gold $\{110\}$ surface takes place at about 680 K [37], we speculate that at 400 K the surface of the rod is really going through this roughening transition, which is shifted to lower temperature as a finite size effect due to the fairly small width of these facets. Once the original $\{110\}$ surfaces roughen, the facets in these directions disappear and the rod reconstructs itself to grow new $\{111\}$ facets on the surface which becomes more and more flat with increasing temperature. The surface is flattest after the rod reaches the intermediate state and is equilibrated at 900, 1000, and 1100 K, as we can see from the average cross-sectional shape at 1100 K. Nevertheless, because the bond curvature distribution also includes the effect from thermal fluctuation, which increases with temperature, the distribution at 1100 K is lower and broader than that at 800 K, similar to the case for the gold Ih cluster (see Fig. 4.11).

6.4 Structural Change of Different Layers

As we have seen that the roughening transition at $T_s \simeq 400$ K of the unstable gold $\{110\}$ facets drive the surface to change to the more stable gold $\{111\}$ facets, we

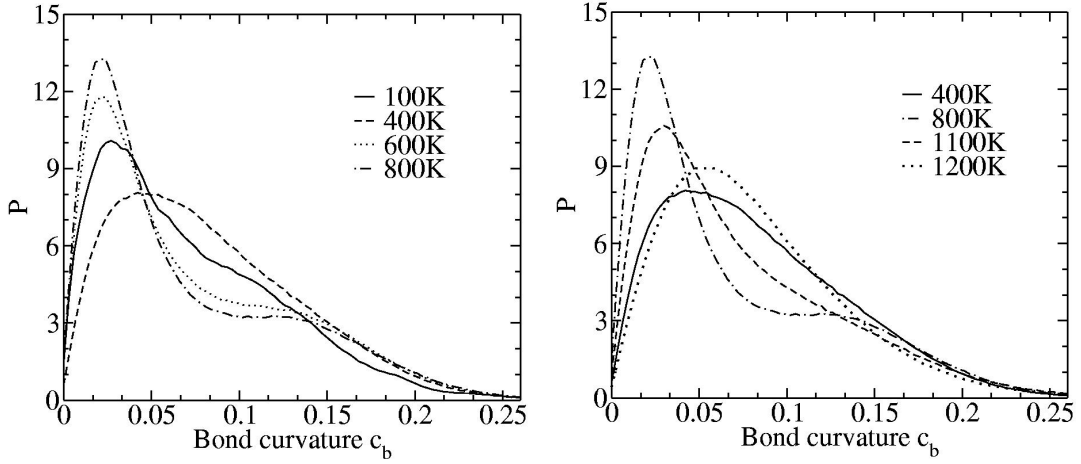


Fig. 6.9: Histograms of bond curvature c_b for the instantaneous configurations of the rod at different temperatures.

want to know how the layers beneath the surface layer behave in response to the surface change. We divide the rod into surface, four sub surface layers, and interior by using the cone algorithm described in Section 3.5.1. We then compute the four bond orientational order parameters Q_4 , Q_6 , \hat{W}_4 , and \hat{W}_6 , defined in Section 3.3, separately for each layer and for the bulk, as we have done for the Ih cluster in Section 4.2. In Fig. 6.10 we show the results for the $N = 2624$ gold nanorod. Unlike \hat{W}_4 for the Ih cluster (see Fig. 4.4), here all four bond parameters have very small fluctuations at each temperature.

In Fig. 6.10f we see that the interior of the rod changes from almost pure fcc to hcp-dominated at $T_s \simeq 400$ K. It changes back to fcc-dominated at 800 K and remains almost unchanged up to the melting $T_m \simeq 1120$ K. Similar structure as in the interior is observed for all sub layers except the surface.

In order to look into the details of the shell structures and how they change with temperature, in Fig. 6.11, we show pictures of the surface and the second sub layer. The second sub layer is almost free of surface distortion, and so allows us to see clearly the structure. As we know from Fig. 6.10, the other layers have similar structures. At each temperature, Fig. 6.11 shows the 500th configuration taken out

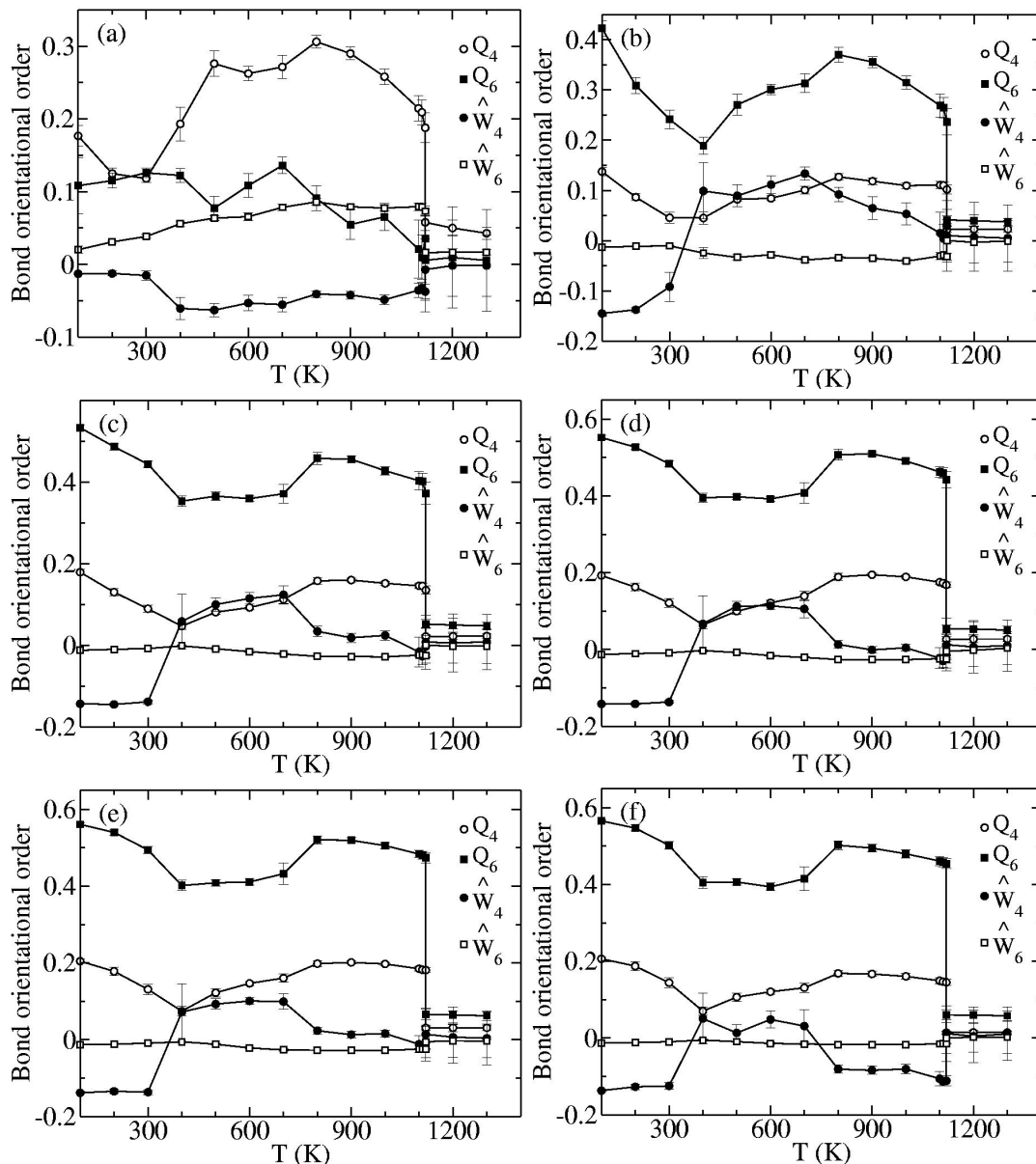


Fig. 6.10: Bond orientational order parameters of the (a) surface, (b) first sub layer, (c) second sub layer, (d) third sub layer, (e) fourth sub layer, and (f) interior of the rod vs. temperature.

from the 1000 configurations sampled during the simulated time of 43 ns. The atoms are then colored by their 2D local structures, as we have done previously for the rods shown in Fig. 6.4.

From Fig. 6.11 we see that, despite the differences in the average bond order parameters shown in Fig. 6.10, the surface has a similar 2D structure as the inner layers. By 100 K, the rod has already lost its side $\{110\}$ facets. Although in the second sub layer one sees a remainder of the $\{100\}$ facets, these are no longer clearly in evidence on the surface. Then at $T_s \simeq 400$ K, the order of the $\{100\}$ facets on the inner sub layer is destroyed. Above 400 K, once the side surfaces have roughened, nucleation of $\{111\}$ facets takes place at different spots. The spots grow into larger $\{111\}$ facets by including more and more atoms near the facets as a way to release the surface tension of the kinks and steps between those facets. By 800 K, the facets are almost free of kinks and steps, and the rod has reached its intermediate state. The surface of the intermediate state remains qualitatively unchanged until melting at $T_m \simeq 1120$ K.

6.5 Evolution of the Interior

Since the different layers and the bulk change simultaneously, we now want to find out how the change of the internal structure is synchronized with the surface change. We investigate the evolution of the internal structure by carrying out an analysis of the local crystal structure, as we have done for the rod with continuous heating in Section 5.4.

The local structure is determined by performing a local bond order parameter calculation as we have already done in Fig. 6.5, but now we show for more temperature values. The atoms are colored according to their local structure: fcc is yellow, hcp is green, and “other” is gray. In Fig. 6.12 we show the cross sections of these configurations. At each temperature, the pictures are from the same configuration as shown in Fig. 6.11. Each row of the two columns shows one of the two orthogonal

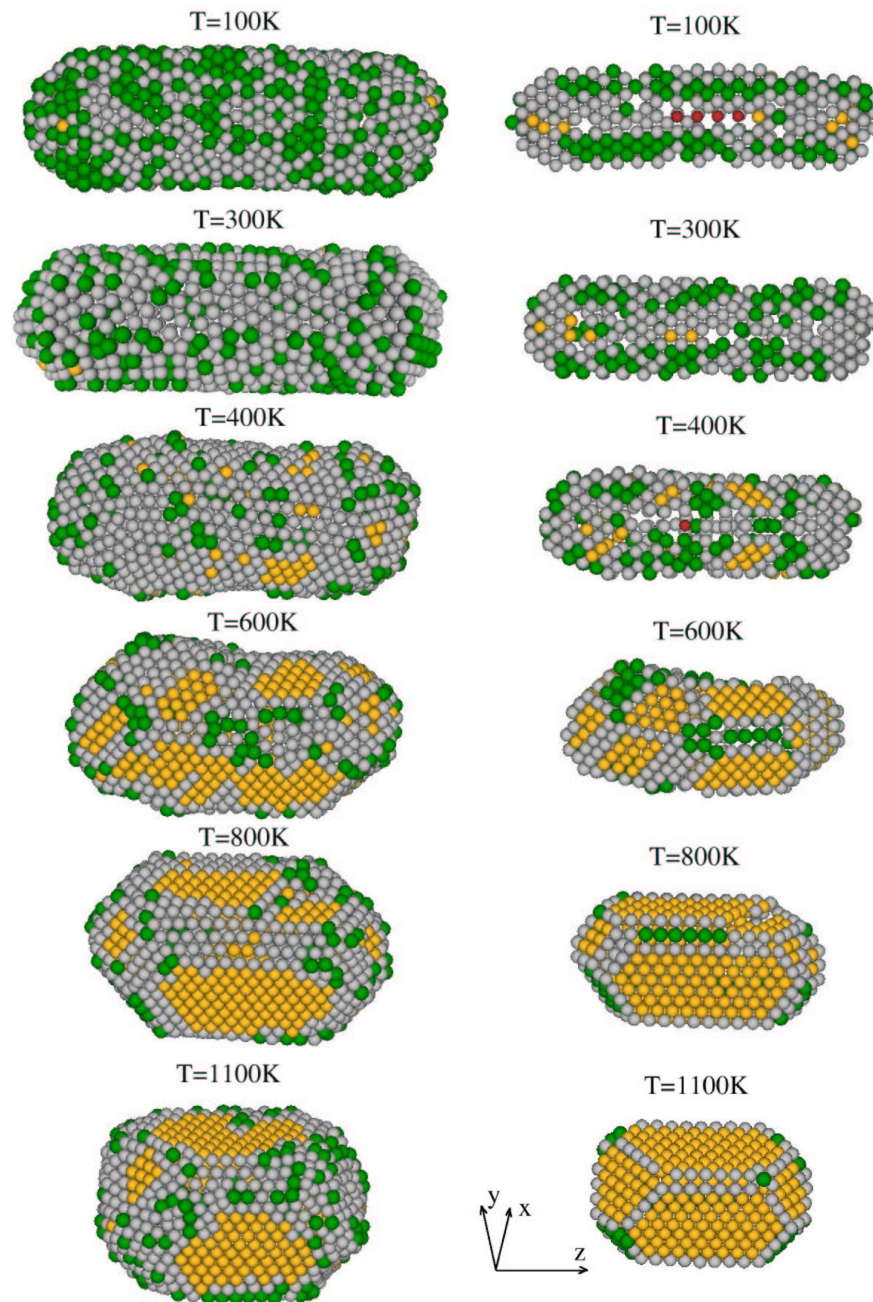


Fig. 6.11: Snapshots of the surface (left column) and the second sub layer (right column) of the rod at different temperatures. The atoms are colored according to their local 2D surface structure: $\{111\}$ is yellow, $\{100\}$ is green, $\{110\}$ is red, and "other" is gray.

cross sections of the same configuration, the cross section in the y - z plane (left) and the cross section in the x - z plane (right). At 100 K, the rod has an almost pure fcc crystal structure by construction, with the long axis of the rod (z -axis) along the $[100]$ direction of the crystal. Thus the planes of the cross sections are square $\{100\}$ surfaces, as shown in Fig. 2.2. At 300 K, two $\{111\}$ planes slide to form local hcp structures. At $T_s \simeq 400$ K, as the surface roughens, less strain on the surface allows many $\{111\}$ planes to slide forming a random stacking structure. This random stacking process has destroyed the order of the initial crystal structure, and reduces the energy required to reform $\{111\}$ planes in the interior with their normal along the \hat{x} axis. At 600 K, as the surface is forming $\{111\}$ facets with their normal along the \hat{x} direction, the internal atoms are forced to reorganize themselves to coincide with the surface, as we can see from the random stacking along the \hat{x} axis. After the surface and internal atoms finish the adjustment, the rod reaches its intermediate state, now with the long axis of the rod (the \hat{z} axis) along the $[10\bar{1}]$ crystal orientation. This structural transformation is accompanied by a shape transformation, in which the end cap atoms move closer to the center of mass by joining the random stacking process. These atomic movements have the same pattern illustrated by the velocity field plot for the continuous heating shown in Fig. 5.13.

6.6 Diffusion of Atoms

Finally we consider whether the structural transformation described in the preceding sections is accompanied by large scale atomic diffusion, as would be the case if the structural transformation was nucleated by a partial melting of the rod. In Fig. 6.13 we show our measurement of the inter-layer diffusion by using the interlayer mixing parameter $\langle n \rangle$ described in Section 4.4. Compared with the plot for the gold Ih cluster in Fig. 4.15, we see that the rod behaves similarly to the cluster. No excessive inter-layer diffusion at the temperatures characteristic of the onset and completion of the structural transformation, $T_s \simeq 400$ K and 800 K, is observed.

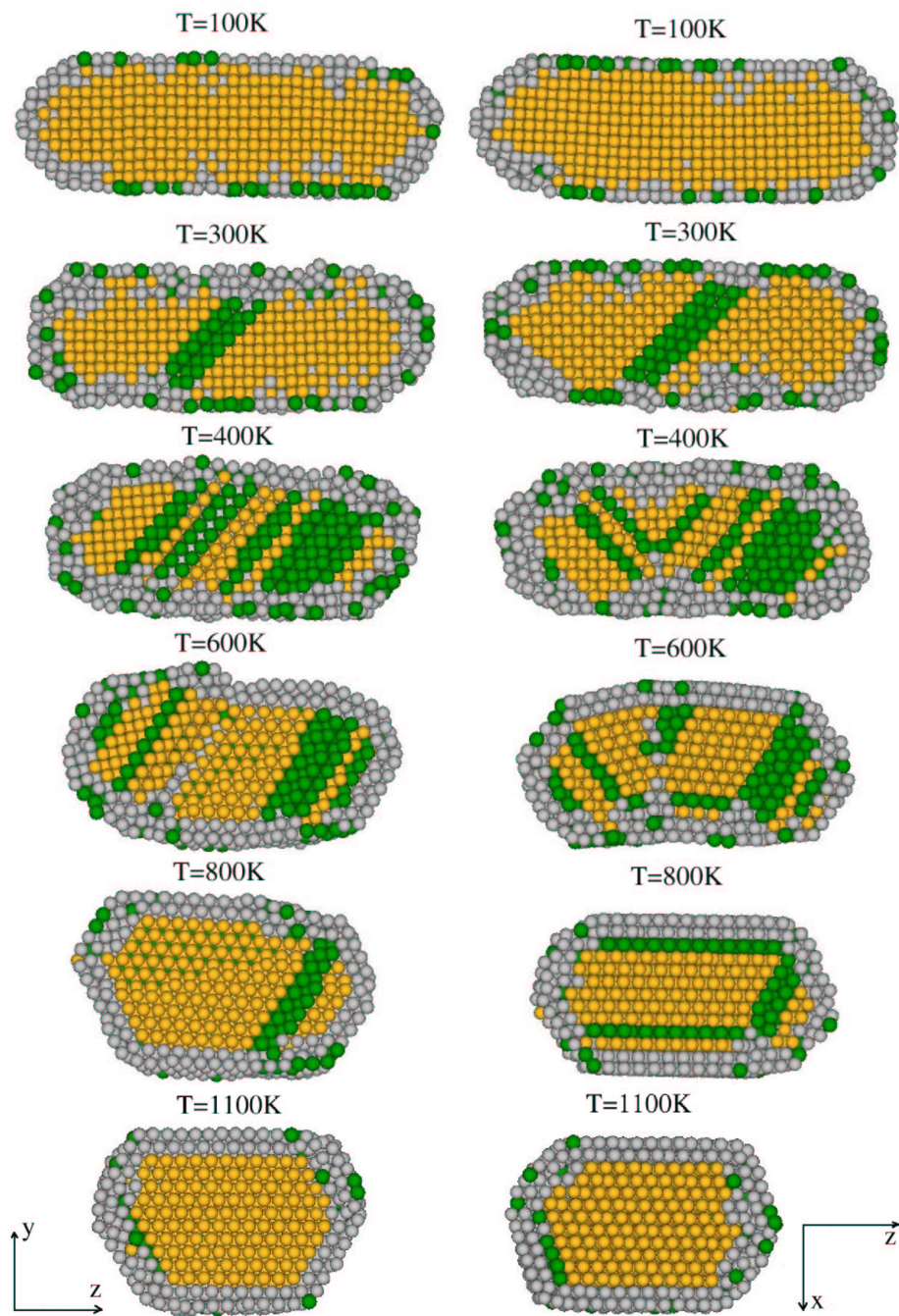


Fig. 6.12: Cross sections of a gold nanorod with $N = 2624$ atoms at different temperatures along the $x = 0$ plane (left) and along the $y = 0$ plane (right). The atoms are colored according to their local structure: fcc is yellow, hcp is green, and “other” is gray.

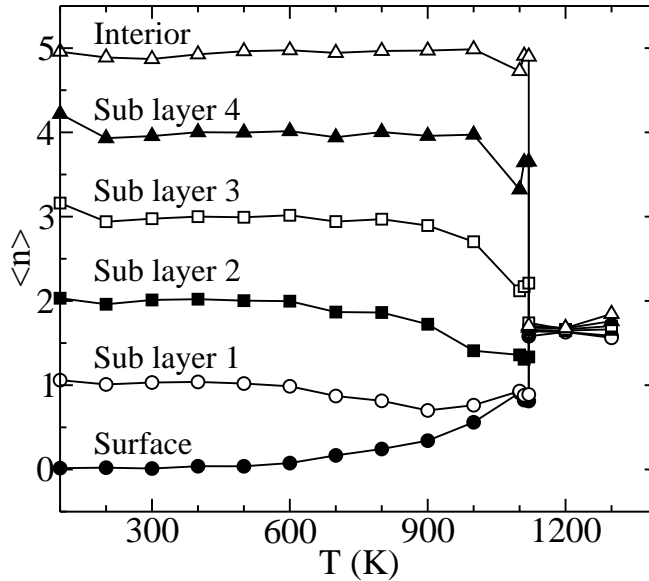


Fig. 6.13: Inter-layer mixing parameter $\langle n \rangle$ vs. T , for atoms initially in the different layers and the interior of the gold nanorod with $N = 2624$ atoms.

We then measure the mobility of atoms by computing the diffusion coefficients D determined from the atomic mean squared displacements, as defined in Section 3.6. The values for different layers of the rod at different temperatures are shown in Fig. 6.14. Comparing it with the plot for the Ih cluster in Fig. 4.17, we see that the two sets of data are quite similar with only a small diffusive tail below T_m . This further verifies that the transformation does not require atomic diffusion.

6.7 Discussion and Conclusions

From all of the above results, we conclude that the shape transformation of the gold nanorod with 2624 atoms is induced by the surface energy minimization, and is accompanied by a complete reconstruction of the internal structure. The transformation leads the rod from an initial aspect ratio of 3.0 and a pure fcc structure to a shorter and wider rod with an aspect ratio of 1.8 and another pure fcc structure, but with the fcc bulk reorienting. Initially the long axis of the rod is along [100]

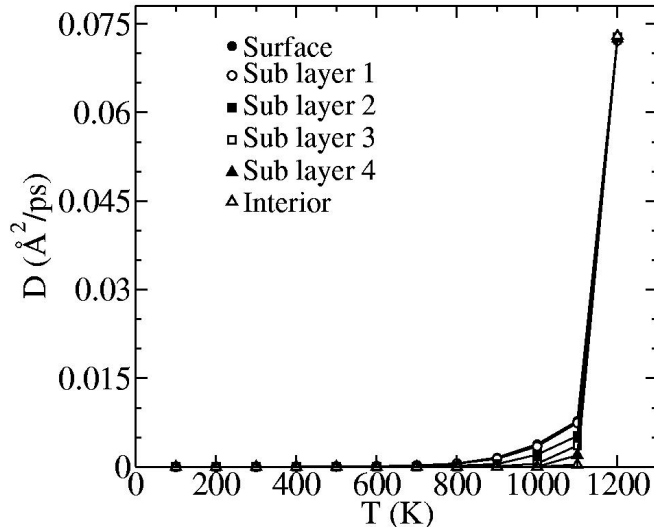


Fig. 6.14: Diffusion coefficients D vs. T for different layers and the interior of the $N = 2624$ atom rod.

crystal direction. After the fcc bulk is reoriented, the long axis is along the $[10\bar{1}]$ crystal direction. The transformation is initiated by the roughening of the initial $\{110\}$ facets taking place at $T_s \simeq 400$ K. The roughened surface allows the internal $\{111\}$ planes to slide, forming a random stacking structure to destroy the order of the initial crystal. After the roughening takes place, regions of $\{111\}$ facets form and grow by absorbing more adjacent atoms as a way to release the surface tension of the kinks and steps. The forming of $\{111\}$ facets on the surface requires the forming of the $\{111\}$ planes in the interior with their normal along the \hat{x} direction, so that the crystal orientation changes in the way that the long axis of the rod is now along the $[10\bar{1}]$ direction of the fcc crystal structure. The rod finally reaches the intermediate state, which is stable for a wide temperature range, with an almost pure fcc body with its surface mostly covered by gold $\{111\}$ facets. During the structural change the rod becomes shorter and wider by moving some atoms on the end caps to the sides of the rod through the random stacking process. No atomic diffusion participates in the shape and structural transformation.

Comparing with the results for the continuous heating of the gold nanorod with 2624 atoms, we see that the results for the quasi-equilibrium heating is closer to that for the slower heating rate. The hcp-dominated state represents the random stacking process in the middle of the transformation. The “stable” hcp-dominated intermediate state just results from the kinetic process of the continuous heating method. It will change towards the pure fcc intermediate state if the rod is fully relaxed for an adequate time. One evidence supporting this is the small but noticeable increase of the number of fcc atoms just below the melting temperature during the continuous heating (see Fig. 5.11). Similarly, with a slower heating rate, the temperature range of the hcp-dominated state for the larger size rods should shrink. The intermediate states of the rods with different aspect ratios should have a similar structure which is a pure fcc body mostly covered by gold {111} facets, although the aspect ratios of the intermediate states may be different, which may depend on the heating procedure.

Comparing with the gold Ih cluster, we see that the intermediate state appears more stable in our simulated time range of 43 ns at each temperature. The intermediate rod melts at a higher temperature of ~ 1120 K than ~ 1075 K for the gold Ih cluster with the same size. This may be due to the facts that the intermediate rod has a pure fcc body without the extra energy caused by the twin grain boundary inside the body, and that it has less vertices and edges on the surface, which “melt” at a much lower temperature than the T_m . However, partly supported by the observation that the potential energy of the intermediate rod is still a little higher than the gold Ih cluster (see Fig. 6.3), which results from the larger surface area of the rod, we expect that, for a very long run that approaches the *true* equilibrium, the intermediate rod will melt at a lower temperature than the gold Ih cluster, or go through a solid-to-solid transition from the rod to the Ih cluster.

7. SUMMARY

We have carried out Molecular Dynamics (MD) simulations to study the thermal stability and melting behavior of gold nanoclusters and gold nanorods. Because of their small sizes, the surface plays a very important role in the behavior of nanomaterials. In equilibrium, the potential energy of surface atoms are higher than those in the interior. Thus at low temperatures, the global minimum shape of nanomaterials is in general achieved by minimizing their surface energy. This can be done either by minimizing the surface area, or by covering the surface as much as possible by the low energy, close-packed hexagonal facets. However, these two requirements are sometimes contradictory. In addition, minimizing the surface energy may distort the internal structure and invoke strain energy. The balance of these three energetic requirements decides the equilibrium shape of nanomaterials. It is this single physical reason that leads gold nanoclusters with hundreds to thousands of atoms to favor the Mackay icosahedron crystalline structure, and drives gold nanorods to go through a morphological and structural transformation to obtain a more preferable surface geometry.

The Mackay icosahedron (Ih) is a crystalline structure covered only by 20 hexagonal planes. It has the highest symmetry of all discrete point groups. These two facts lead the Ih structure to reach the lowest possible surface potential energy. Although the internal twin grain and strain energy make it unfavorable for bulk materials, the lower surface energy can compensate for these effects and make the Ih structure the preferred one for small clusters. In chapter 4, we find that upon cooling, gold nanoclusters with hundreds to thousands of atoms solidify into an Ih crystalline structure with a missing central atom. We believe that this is the thermodynamically preferred

crystalline structure in this size range of gold nanoclusters. Upon heating these Ih clusters from low temperatures to above the bulk melting temperature T_m of the clusters, we confirm that the melting temperature of the gold clusters decreases when the gold cluster becomes smaller [50]. However, unlike previous results on smaller cuboctahedral clusters, which include non $\{111\}$ facets that premelt below T_m [50], we find no surface premelting or roughening of the $\{111\}$ facets of our Ih clusters. Nevertheless, we find that there is a considerable softening of the cluster surface roughly ~ 200 K below T_m due to the motion of atoms along the vertices and edges of the cluster. In this temperature range we find both intra-layer and inter-layer diffusion of atoms, which increases as T_m is approached. The average shape evolves from fully faceted, to faceted with rounded edges, to nearly spherical just below T_m . Throughout this region, the interior atoms of the cluster remain essentially perfectly ordered, until T_m is reached.

Theoretical work [96] gives a similar picture of the rounding of edges and shrinking of facets for the equilibrium shape of macroscopically large crystals, where the continuum Wulff construction [16] can be applied. In this theory, the shrinkage of facets is associated with approaching a roughening transition of the faceted surface, and the facet length shrinks proportionally to the inverse of the roughening correlation length. We do not believe that this theory explains the results for our clusters. Firstly, it is generally believed that the gold $\{111\}$ surface that forms the facets of our Ih cluster does not have a roughening transition below the bulk melting transition [23, 24]. This is consistent with our observation that the surface softening of our clusters seems to track the cluster melting temperature which is *size dependent*. If there was a true thermodynamic roughening transition, we would expect the surface softening to approach a *size independent* onset temperature. Moreover, in that theory, no diffusion of atoms need be involved in the vanishing of facets. The roughening transition can occur within the context of the crystalline state. In our case, it is clear that diffusion of atoms along the vertices and edges plays an important role.

We therefore believe that the phenomena we observe in our simulated nanoclusters are due to the finite, relatively small, size of our clusters. The continuum approaches are not valid for these small clusters and one must consider the atomistic nature of the system. The rounding of edges and shrinkage of facets that we observe are better attributed to a “melting” of the cluster edges, which then spreads out into the ordered facets as the temperature increases towards melting.

With the observation that, at high temperatures just below T_m , the $\{111\}$ surface facets of the gold Ih clusters remain ordered while still all surface atoms diffuse, one may conceive of another possible surface melting mechanism, in contrast to the above “edge melting” one. One might suppose that the surface is really in a liquid state in the sense of losing its translational order, and that the orientational order is maintained by an effective substrate periodic potential formed by the ordered sub layer beneath the surface. This mechanism however is doubtful due to the fact that, at these temperatures, small facets are still present in the average cluster shapes. It is more likely that the sizes of the facets shrink but do not vanish below T_m . Nevertheless, at high temperatures near T_m , because the facets become so small, the atoms on the facets easily exchange with the atoms in the “liquid” edges around the facets, so that even atoms on the facets will, over time, diffuse.

As for possible future work on gold Ih clusters, it would be interesting to check the hysteresis and the freezing mechanism. Simulations with bigger sizes may determine the critical size up to which the Ih structure is preferred for gold nanoclusters. If possible, a quantitative definition of the roughening transition for small nanoclusters would be helpful to show the non-roughening nature of gold Ih clusters. As always, longer simulation time will be helpful to verify our conclusions. It will be directly useful to experiments to study the aggregation of gold nanoclusters and their binding mechanism to organic molecules.

In Chapter 5 we have reported on our continuous heating MD study of gold nanorods, which mimics the experimental laser heating of gold nanorods. The ini-

tial gold nanorods have a pure fcc body and the elongated gold $\{100\}$ and $\{110\}$ facets on the sides (see Fig. 2.13). A shape transformation has been found to precede the melting transition. The shape change is accompanied by a structural change, through which the pure fcc body becomes hcp-dominated by sliding planes along $\langle 111 \rangle$ directions, and sometimes changes back to be fcc-dominated at higher temperatures. The exact aspect ratio and the structure of the intermediate state after the shape transformation depends on rod size, heating rate and initial aspect ratio. The shorter and wider intermediate state corresponds to what is seen experimentally, and the planar internal defects in experiments might be the sliding planes changing from the fcc to the hcp local structure, according to our simulations.

Although the results can be compared directly with experiments, in the continuous heating simulations, we can only obtain instantaneous physical properties, which is insufficient to understand the physical reasons behind the phenomenological observations. Thus in Chapter 6, we have reinvestigated the same gold nanorod with $N = 2624$ atoms by a quasi-equilibrium heating method. We find that the shape transformation of the rod drives the rod from the initial one with thermally less stable $\{100\}$ and $\{110\}$ facets to an intermediate rod with its surface mostly covered by more stable $\{111\}$ (hexagonal) facets. This transformation is triggered by the roughening transition on the surface $\{110\}$ facets. To be consistent with the surface geometry, the internal crystalline structure changes from a pure fcc with the long axis of the rod along the $[100]$ crystal orientation, to another pure fcc with long axis of the rod along the $[10\bar{1}]$ crystal orientation. This internal structural change is accomplished through a random stacking process in the interior, which is the consequence of surface roughening and reordering. No atomic diffusion takes place during this transformation.

Some phenomena observed upon the continuous heating can be explained by the results for the quasi-equilibrium heating. The hcp-dominated state is encountered as an intermediate configuration along the way of changing from the initial fcc structure

to the intermediate fcc structure. Due to the kinetic effect of continuous heating, it sometimes appears stable in some temperature range. The surface roughening and reorganization to stable $\{111\}$ facets leads to the surface disordering and reordering observed in the continuous heating.

According to the mechanism conceived from our simulations, we do not believe that the mechanism suggested by Link *et al.* [30], which has been described in Section 2.4, is what really happens in experiments. They suggested that the defects created by local melting and the surface diffusion lead to the twinned crystal. However, as we have shown, the shape transformation does not require atomic diffusion, and our intermediate state model with a pure fcc body should be more stable than the twinned crystal they have suggested in Fig. 2.15d. The experimental observed twinned and bent crystals might be the rods that are midway in the process of the shape transformation.

Some points remain for the future study of gold nanorods. We have never observed the ϕ -shaped intermediate state found in experiments, and our simulated rods do not exhibit point defects inside the rods. We believe this is because the gold nanorods studied by experiments are several magnitudes larger than our simulated rods, so that the shape and structural changes can happen inhomogeneously, and the anisotropy can be frozen in the intermediate states. Simulations of much bigger clusters might be able to observe these phenomena, when the shape transformation happens inhomogeneously and the anisotropic states can be stable for a long time. It will be necessary to develop numerical methods for computing the average shapes for the gold nanorods and tracking how structural changes happen on different facets separately. An equilibrium study on the intermediate rod similar to the one done for the gold Ih cluster will help to understand more about their equilibrium properties. More simulations and analysis on the rods with different sizes and aspect ratios will generalize our conclusions. It will also be interesting to check the (meta)stability of the hcp-dominated intermediate state for the continuous heating and study the mechanism by which it goes to the intermediate state with a pure fcc body.

Our simulations on rods have been carried out only for one particular model of the initial rod configuration, that of Fig. 2.13. Several other possible models for experimental gold nanorods have been suggested, such as the elongated cyclic penta-tetrahedral twin model shown in Fig. 2.11, and the model for long rods shown in Fig. 2.12. A more common mechanism about the shape transformations of gold nanorods can only be drawn after the simulations have also been done for these other kinds of models,

It is worth noting that our simulations for gold nanorods are all made for gold nanomaterials with ideal environmental conditions, such as in vacuum and without support materials. In the experiments the rods we have studied are capped by micelles. The experimental heating process is more complicated than linearly increasing the total energy of each atom. Further simulations and evaluations will clarify the differences between the theoretical and experimental studies.

Finally we discuss the equilibrium and kinetic effects in our simulations. The *true* equilibrium of a thermodynamic system can be reached in principle by waiting for an infinite long time. In a finite time range there is always a possibility that kinetic effects are important. However, in real life we are generally interested in the physical properties of a thermodynamic system with a time duration ranging from seconds to years ($\sim 1 \text{ s} - 10^8 \text{ s}$) rather than the *true* equilibrium properties. Thus when we talk about the equilibrium properties of a system, we always assume the equilibrium with more or less kinetic effects. With the basic MD methods we have used and the capability of modern computers, we can only propagate the system for about tens of nanoseconds ($\sim 10^{-8} \text{ s}$). To make our simulation studies valuable for experiments, we have to theoretically interpret our results for a very limited simulated time extending to a time several magnitudes longer. A very common situation is that the system reaches its thermodynamically most stable state in the simulated short time, and because the energy barriers to jump to other states are so high, the system is not expected to transfer to such other states even in a much longer but finite time. In this

case kinetic effects brought in by very short simulated times will not qualitatively change the behavior from that of more realistic experimental time scales. We believe our simulations for the gold Ih clusters fall into this category. At temperatures far from the melting temperature, the clusters do not have any noticeable change after the equilibration time of 4.3 ns. The exact melting temperature should be lower than that given by the simulation with finite simulated time. However, because the vertex and edge softening starts at a temperature much lower than the experimental melting temperature, the superheating should not be significant.

In the simulations of gold nanorods, we are interested in the equilibrium properties of the intermediate state. Although in the limit of true equilibrium, the intermediate rod obtained in the quasi-equilibrium simulation should finally change to a more spherical shape (e.g. the Ih cluster), the large $\{111\}$ facets should be able to stabilize the rod for a very long time. Especially with a much bigger size, the rod may be stable in the experimental time range. On the other hand, when we investigate the mechanism of the rod transforming from the initial to the intermediate state, we are not interested in the exact equilibrium properties at each temperature. Instead we are more concerned with the kinetic procedure. In this case, a transformation that happened at a certain temperature may happen at a lower temperature if the simulated time is much longer. However, it is the procedure, not the temperature at which the procedure happens that we are really interested in. Transformations are easier to happen at high temperatures, thus we can use a shorter simulated time, as long as the kinetic effects are not too severe to change the dynamics.

In summary, in this thesis we have studied the thermal stability and melting behavior of gold nanoclusters and gold nanorods by molecular dynamics simulations. We find that the surface plays a very important role in both nanomaterials. The results are coincident with experiments, and we believe our studies will benefit the future applications of gold nanomaterials, as well as the studies of other nanomaterials.

BIBLIOGRAPHY

- [1] T. A. Taton, C. A. Mirkin, and R. L. Letsinger, *Science* **289**, 1757 (2000).
- [2] J.-M. Nam, C. S. Thaxton, and C. A. Mirkin, *Science* **301**, 1884 (2003).
- [3] S. O. Obare, R. E. Hollowell, and C. J. Murphy, *Langmuir* **18**, 10407 (2002).
- [4] M. G. Warner and J. E. Hutchison, *Nature Materials* **2**, 272 (2003).
- [5] J. Zheng, Z. Chen, and Z. Liu, *Langmuir* **16**, 9673 (2000).
- [6] A. T. Bell, *Science* **299**, 1688 (2003).
- [7] K. K. Caswell, J. N. Wilson, U. H. F. Bunz, and Catherine J. Murphy, *J. Am. Chem. Soc.* **125**, 13 914 (2003).
- [8] J. A. Ascencio, C. Gutiérrez-Wing, M. E. Espinosa, M. Martín, S. Tehuacanero, C. Zorrilla, and M. José-Yacamán, *Surf. Sci.* **396**, 349 (1998).
- [9] B. Pauwels, G. Van Tendeloo, W. Bouwen, L. T. Kuhn, P. Lievens, H. Lei, and M. Hou, *Phys. Rev. B* **62**, 10 383 (2000).
- [10] S. Tehuacanero, R. Herrera, M. Avalos, and M. José-Yacamán, *Acta Metall. Mater.* **40**, 1663 (1992).
- [11] Y. G. Chushak and L. S. Bartell, *J. Phys. Chem. B* **105**, 11 605 (2001).
- [12] H.-S. Nam, Nong M. Hwang, B. D. Yu, and J.-K. Yoon, *Phys. Rev. Lett.* **89**, 275 502 (2002).

- [13] L. D. Marks, *Rep. Prog. Phys.* **57**, 603 (1994).
- [14] A. L. Mackay, *Acta Cryst.* **15**, 916 (1962).
- [15] T. P. Martin, *Phys. Rep.* **273**, 199 (1996).
- [16] G. Wulff, *Z. f. Kristallog.* **34**, 449 (1901); C. Herring, *Phys. Rev.* **82**, 87 (1931).
- [17] S. Ino, *J. Phys. Soc. Japan* **27**, 941 (1969).
- [18] L. D. Marks, *Phil. Mag.* **49**, 81 (1984).
- [19] C. L. Cleveland, U. Landman, M. N. Shafigullin, P. W. Stephens, and R. L. Whetten, *Z. Phys. D* **40**, 503 (1997).
- [20] C. L. Cleveland, U. Landman, T. G. Schaaff, M. N. Shafigullin, P. W. Stephens, and R. L. Whetten, *Phys. Rev. Lett.* **79**, 1873 (1997).
- [21] K. Michaelian, N. Rendón, and I. L. Garzón, *Phys. Rev. B* **60**, 2000 (1999).
- [22] C. L. Cleveland, W. D. Luedtke, and U. Landman, *Phys. Rev. Lett.* **81**, 2036 (1998); C. L. Cleveland, W. D. Luedtke, and U. Landman, *Phys. Rev. B* **60**, 5065 (1999).
- [23] P. Carnevali, F. Ercolessi, and E. Tosatti, *Phys. Rev. B* **36**, 6701 (1987).
- [24] K. D. Stock and B. Grosser, *J. Cryst. Growth* **50**, 485 (1980).
- [25] F. D. Di Tolla, E. Tosatti, and F. Ercolessi, *Interplay of melting, wetting, overheating and faceting on metal surfaces: theory and simulation, in Monte Carlo and molecular dynamics of condensed matter systems*, K. Binder and G. Ciccotti (Eds.), Società Italiana di Fisica, Bologna, 1996, p. 345-398.
- [26] A. P. Alivisatos, *J. Phys. Chem.* **100**, 13 226 (1996).
- [27] V. Albe, C. Jouanin, and D. Bertho, *J. Cryst. Growth* **184/185**, 388 (1998).

- [28] S. Chang, C. Shih, C. Chen, W. Lai, and C. R. C. Wang, *Langmuir* **103**, 1165 (1999).
- [29] S. Link, C. Burda, B. Nikoobakht, and M. A. El-Sayed, *J. Phys. Chem. B* **104**, 6152 (2000).
- [30] S. Link, Z. L. Wang, and M. A. El-Sayed, *J. Phys. Chem. B* **104**, 7867 (2000).
- [31] B. M. Ocko, D. Gibbs, K. G. Huang, D. M. Zehner, and S. G. J. Mochrie, *Phys. Rev. B* **44**, 6429 (1991).
- [32] I. N. Stranski, *Z. Phys.* **119**, 22 (1942).
- [33] J. Frenkel, *Kinetic Theory of Liquids*, Clarendon Press: Oxford, 1946.
- [34] J. W. M. Frenken and J. F. van der Veen, *Phys. Rev. Lett.* **54**, 134 (1985).
- [35] A. W. Denier van der Gon, R. J. Smith, J. M. Gay, D. J. O'Connor, and J. F. van der Veen, *Surf. Sci.* **227**, 143 (1990).
- [36] B. Pluis, A. W. Denier van der Gon, J. W. M. Frenken, and J. F. van der Veen, *Phys. Rev. Lett.* **59**, 2678 (1987).
- [37] A. Hoss, M. Nold, P. von Blanckenhagen, and O. Meyer, *Phys. Rev. B* **45**, 8714 (1992).
- [38] F. Ercolessi, M. Parrinello, and E. Tosatti, *Philos. Mag. A* **58**, 213 (1988).
- [39] F. Ercolessi, S. Iarlori, O. Tomagnini, E. Tosatti, and X. J. Chen, *Surf. Sci.* **251/252**, 645 (1991).
- [40] K. G. Huang, D. Gibbs, D. M. Zehner, A. R. Sandy, and S. G. J. Mochrie, *Phys. Rev. Lett.* **65**, 3313 (1990).
- [41] G. M. Watson, D. Gibbs, S. Song, A. R. Sandy, S. G. J. Mochrie, and D. M. Zehner, *Phys. Rev. B* **52**, 12 329 (1995).

- [42] S. G. J. Mochrie, D. M. Zehner, B. M. Ocko, and D. Gibbs, *Phys. Rev. Lett.* **64**, 2925 (1990).
- [43] G. Gilalbegović and E. Tosatti, *Phys. Rev. B* **48**, 11 240 (1993).
- [44] J. C. Heyraud and J. J. Metois, *J. Crystal Growth* **50**, 571 (1980).
- [45] Z. Wang and P. Wynblatt, *Surf. Sci.* **398** 259 (1998).
- [46] N. T. Wilson and R. L. Johnston, *Eur. Phys. J. D* **12**, 161 (2000).
- [47] Y. Chushak and L. S. Bartell, *Eur. Phys. J. D* **16**, 43 (2001).
- [48] S. M. Foiles, M. I. Baskes, and M. S. Daw, *Phys. Rev. B* **33**, 7984 (1986).
- [49] J.-H. Shim, B.-J. Lee, and Y. W. Cho, *Surf. Sci.* **512**, 262 (2002).
- [50] F. Ercolessi, W. Andreoni, and E. Tosatti, *Phys. Rev. Lett.* **66**, 911 (1991).
- [51] S. Iijima and T. Ichihashi, *Phys. Rev. Lett.* **56**, 616 (1986).
- [52] P. M. Ajayan and L. D. Marks, *Phys. Rev. Lett.* **60**, 585 (1988).
- [53] M. Takagi, *J. Phys. Soc. Jpn.* **9**, 359 (1954).
- [54] Ph. Buffat and J.-P. Borel, *Phys. Rev. A* **13**, 2287 (1976).
- [55] L. J. Lewis, P. Jensen, and J.-L. Barrat, *Phys. Rev. B* **56**, 2248 (1997).
- [56] H. B. Liu, J. A. Ascencio, M. Perez-Alvarez, and M. J. Yacaman, *Surf. Sci.* **491**, 88 (2001).
- [57] Z. L. Wang, M. B. Mohamed, S. Link, and M. A. El-Sayed, *Surf. Sci.* **440**, L809 (1999).
- [58] M. J. Yacamán, J. A. Ascencio, and G. Canizal, *Suf. Sci.* **486**, L449 (2001).
- [59] Y.-J. Zhu and X.-L. Hu, *Chem. Lett.* **32**, 1140 (2003).

- [60] N. R. Jana, L. Gearheart, and C. J. Murphy, *J. Phys. Chem. B* **105**, 4065 (2001).
- [61] N. R. Jana, L. Gearheart, S. O. Obare, and C. J. Murphy, *Langmuir* **18**, 922 (2002).
- [62] P. L. Gai and M. A. Harmer, *Nano Lett.* **2**, 771 (2002).
- [63] C. J. Johnson, E. Dujardin, S. A. Davis, C. J. Murphy, and S. Mann, *J. Mater. Chem.* **12**, 1765 (2002).
- [64] B. Nikoobakht and M. A. El-Sayed, *Chem. Mater.* **15**, 1957 (2003).
- [65] J. Gao, C. M. Bender, and C. J. Murphy, *Langmuir* **19**, 9065 (2003).
- [66] N. Taub, O. Krichevski, and G. Markovich, *J. Phys. Chem. B* **107**, 11 579 (2003).
- [67] B. D. Busbee, S. O. Obare, and C. J. Murphy, *Adv. Mater.* **15**, 414 (2003).
- [68] S. Link, C. Burda, B. Nikoobakht, and M. A. El-Sayed, *Chem. Phys. Lett.* **315**, 12 (1999).
- [69] S. Link, C. Burda, M. B. Mohamed, B. Nikoobakht, and M. A. El-Sayed, *J. Phys. Chem. A* **103**, 1166 (1999).
- [70] S. Link and M. A. El-Sayed, *J. Chem. Phys.* **114**, 2362 (2001).
- [71] Z. L. Wang, R. P. Gao, B. Nikoobakht, and M. A. El-Sayed, *J. Phys. Chem. B* **104**, 5417 (2000).
- [72] M. HU, X. Wang, G. V. Hartland, P. Mulvaney, J. P. Juste, and J. E. Sader, *J. Am. Chem. Soc.* **125**, 14 925 (2003).
- [73] N. R. Jana, L. A. Gearheart, S. O. Obare, C. J. Johnson, K. J. Edler, S. Mann, and C. J. Murphy, *J. Mater. Chem.* **12**, 2909 (2002).

- [74] B. Nikoobakht, Z. L. Wang, and M. A. El-Sayed, *J. Phys. Chem. B* **104**, 8635 (2000).
- [75] X. Yu and P. M. Duxbury, *Phys. Rev. B* **52**, 2102 (1995).
- [76] N. Combe, P. Jensen, and A. Pimpinelli, *Phys. Rev. Lett.* **85**, 110 (2000).
- [77] D. Marx and J. Hutter, *Ab initio molecular dynamics: Theory and implementation; Modern Methods and Algorithms of Quantum Chemistry*, J. Grotendorst (Ed.), Forschungszentrum Juelich, NIC Series, Vol. 1, 2000.
- [78] D. J. Wales and J. P. K. Doye, *J. Phys. Chem. A* **101**, 5111 (1997).
- [79] J. N. Murrell and R. E. Mottram, *Mol. Phys.* **69**, 571 (1990).
- [80] H. Cox, R. L. Johnston, and J. N. Murrell, *J. Sol. State Chem.* **145**, 517 (1999).
- [81] H. Cox, X. H. Liu, and J. N. Murrell, *Mol. Phys.* **93**, 921 (1998).
- [82] R. P. Gupta, *Phys. Rev. B* **23**, 6265 (1981).
- [83] P. Hohenberg and W. Kohn, *Phys. Rev. B* **136**, 864 (1964).
- [84] M. S. Daw and M. I. Baskis, *Phys. Rev. Lett.* **50**, 1285 (1983).
- [85] D. Frenkel and B. Smit, *Understanding Molecular Simulation: From Algorithms to Applications*, Academic Press: San Diego, 2002.
- [86] M. P. Allen and D. J. Tildesley, *Computer Simulation of Liquids*, Clarendon Press: Oxford, 1987.
- [87] P. J. Steinhardt, D. R. Nelson, and M. Ronchetti, *Phys. Rev. B* **28**, 784 (1983).
- [88] J. D. Landau and F. M. Lifshitz, *Quantum Mechanics*, Pergamon: New York, 1965.

-
- [89] R. H. Hardin, N. J. A. Sloane and W. D. Smith, *Tables of spherical codes with icosahedral symmetry*, published electronically at <http://www.research.att.com/~njas/icosahedral.codes/>.
- [90] L. L. Boyer and J. Q. Broughton, *Phys. Rev. B* **42**, 11 461 (1990).
- [91] C. Mottet, G. Treglia, and B. Legrand, *Surf. Sci.* **383**, L719 (1997).
- [92] G. Boisvert and L. J. Lewis, *Phys. Rev. B* **52**, 9078 (1995).
- [93] P. J. Feibelman, J. S. Nelson, and G. L. Kellogg, *Phys. Rev. B* **49**, 10 548 (1994).
- [94] W. H. Press, S. A. Teukolsky, W. T. Vetterling, and B. P. Flannery, *Numerical Recipes in C: The Art of Scientific Computing*, Cambridge University Press: Cambridge, 1992.
- [95] G. Burns, *Solid State Physics*, Academic Press: Orlando, 1985.
- [96] C. Jayaprakash, W. F. Saam, and S. Teitel, *Phys. Rev. Lett.* **50**, 2017 (1983).